AWARD NUMBER: W81XWH-14-1-0408

TITLE: Macrophage Efferocytosis and Prostate Cancer Bone Metastasis

PRINCIPAL INVESTIGATOR: Benjamin Philip Sinder, PhD

CONTRACTING ORGANIZATION: University of Michigan
Ann Arbor, MI 48109

REPORT DATE: March 2018

TYPE OF REPORT: Final

PREPARED FOR: U.S. Army Medical Research and Materiel Command
Fort Detrick, Maryland 21702-5012

REPORT DOCUMENTATION PAGE

Form Approved
OMB No. 0704-0188

1. REPORT DATE	2. REPORT TYPE	3. DATES COVERED
March 2018	Final	15 Sept 2014 – 14 Dec 2017

4. TITLE AND SUBTITLE
Macrophage Efferocytosis and Prostate Cancer Bone Metastasis

5a. CONTRACT NUMBER

5b. GRANT NUMBER
W81XWH-14-1-0408

5c. PROGRAM ELEMENT NUMBER

6. AUTHOR(S)
Benjamin Sinder

E-Mail: bpsinder@umich.edu

5d. PROJECT NUMBER

5e. TASK NUMBER

5f. WORK UNIT NUMBER

7. PERFORMING ORGANIZATION NAME(S) AND ADDRESS(ES)
University of Michigan
Ann Arbor, MI 48109

8. PERFORMING ORGANIZATION REPORT NUMBER

9. SPONSORING / MONITORING AGENCY NAME(S) AND ADDRESS(ES)

U.S. Army Medical Research and Materiel Command
Fort Detrick, Maryland 21702-5012

10. SPONSOR/MONITOR'S ACRONYM(S)

11. SPONSOR/MONITOR'S REPORT NUMBER(S)

12. DISTRIBUTION / AVAILABILITY STATEMENT

Approved for Public Release; Distribution Unlimited

13. SUPPLEMENTARY NOTES
Date Covered (Box 3) is actually two periods. 15 Sept 2014 – 31 Dec 2014 (Prior PI JD Jones) and 1 May 2016 – 14 Dec 2017 (Current PI BP Sinder)

14. ABSTRACT

Findings identify macrophages and efferocytosis as a key mediator of prostate cancer skeletal metastasis and the bone microenvironment. Specifically, phagocytic macrophages and efferocytosis were found to be upregulated in the blood of patients with metastatic prostate cancer. Moreover, inhibiting phagocytic macrophages with the chemotherapeutic trabectedin reduced efferocytosis and prostate cancer tumor size in murine models. In addition, trabectedin inhibition of macrophages significantly altered macrophages and efferocytosis in the bone microenvironment – a common site of prostate cancer metastasis. Trabectedin was further found to reduce bone mass and bone healing.

15. SUBJECT TERMS
Macrophages, Efferocytosis, Prostate Cancer, Bone

16. SECURITY CLASSIFICATION OF:			17. LIMITATION OF ABSTRACT	18. NUMBER OF PAGES	19a. NAME OF RESPONSIBLE PERSON
a. REPORT	b. ABSTRACT	c. THIS PAGE			USAMRMC
Unclassified	Unclassified	Unclassified	Unclassified	44	19b. TELEPHONE NUMBER *(include area code)*

Table of Contents

1. **INTRODUCTION:**

Prostate cancers preferentially metastasize to bone which results in increased pain, fracture and morbidity. Numerous and diverse cell types are present in the bone marrow, and these cells make direct contributions to the deleterious outcomes associated with prostate cancer metastasis and growth in the skeleton. Macrophages are a class of phagocytic white blood cells that comprise a large portion of the marrow and their contribution to skeletal metastasis and growth of cancer is an area of emerging interest. Work on this project seeks to define role of macrophages in the bone and tumor microenvironment, including their phagocytic/efferocytic capacity, and related impact of the chemotherapeutic trabectedin.

2. **KEYWORDS:**

Macrophages, efferocytosis, cancer therapeutic, trabectedin, osteoimmunology.

3. **ACCOMPLISHMENTS:**

What were the major goals of the project?

The major goal of the project is to define the role of macrophages and efferocytosis (phagocytosis of apoptotic cells) on the tumor and bone environment.

What was accomplished under these goals?

Outcomes and papers supported by this work are described below. There are four outcomes in total. Specifically, two papers have already been accepted and published: one to the Journal of Clinical Investigation and another to the Journal of Bone and Mineral Research. Two additional manuscripts were also supported by this work, one of which is being actively revised for submission and another being written and submitted in early 2018.

1. Previous work by the prior PI Jacqueline Jones contributed to an accepted publication in the Journal of Clinical Investigation (second author JD Jones) titled, "Apoptosis-induced CXCL5 accelerates inflammation and growth of prostate tumor metastases in bone". Funding support from this grant is acknowledged in the manuscript. Full results can be found in the copy of this paper provided in the appendix. The abstract of the paper below summarizes the results:

"During tumor progression, immune system phagocytes continually clear apoptotic cancer cells in a process known as efferocytosis. However, the impact of efferocytosis in metastatic tumor growth is unknown. In this study, we observed that macrophage-driven efferocytosis of prostate cancer cells in vitro induced the expression of proinflammatory cytokines such as CXCL5 by activating Stat3 and NF-κB(p65) signaling. Administration of a dimerizer ligand (AP20187) triggered apoptosis in 2 in vivo syngeneic models of bone tumor growth in which apoptosis-inducible prostate cancer cells were either coimplanted with vertebral bodies, or inoculated in the tibiae of immunocompetent mice. Induction of 2 pulses of apoptosis correlated with increased infiltration of inflammatory cells and accelerated tumor growth in the bone. Apoptosis-induced tumors displayed elevated expression of the proinflammatory cytokine CXCL5. Likewise, CXCL5-deficient mice had reduced tumor progression. Peripheral blood monocytes isolated from patients with bone metastasis of prostate cancer were more efferocytic compared with

normal controls, and CXCL5 serum levels were higher in metastatic prostate cancer patients relative to patients with localized prostate cancer or controls. Altogether, these findings suggest that the myeloid phagocytic clearance of apoptotic cancer cells accelerates CXCL5-mediated inflammation and tumor growth in bone, pointing to CXCL5 as a potential target for cancer therapeutics."

2. A second manuscript from this work has been written, and is actively being revised for submission. This manuscript also focuses on the role of macrophages and efferocytosis in prostate cancer skeletal metastasis. The original PI (Jacqueline Jones) and current PI (Benjamin Sinder) are co-first authors on the study. This study first identifies the macrophage sub-types present in the metastatic prostate cancer bone and tumor microenvironment, and goes on to examine a candidate treatment. Both M1-like and M2-like macrophages were identified in the skeletal metastatic prostate cancer tumor microenvironment of mice. M2-like macrophages were further found to have a greater efferocytic capacity *in vitro*. Phagocytic CD68+ cells were identified in human prostate cancer tissue array samples. Moreover, increased phagocytic CD68+ cells were observed in patients with a higher Gleason score (Figure 1). Two murine prostate cancer models were utilized to assess the impact of ablating macrophages with the clinically relevant chemotherapeutic trabectedin. Results showed that trabectedin reduced M2-like (CD206+) macrophages in the bone and tumor microenvironment and also reduced prostate cancer skeletal metastatic tumor growth and progression (Figure 2). Collectively this data supports a role for macrophages and efferocytosis in prostate cancer, and the manuscript has been revised and actively being re-submitted for publication.

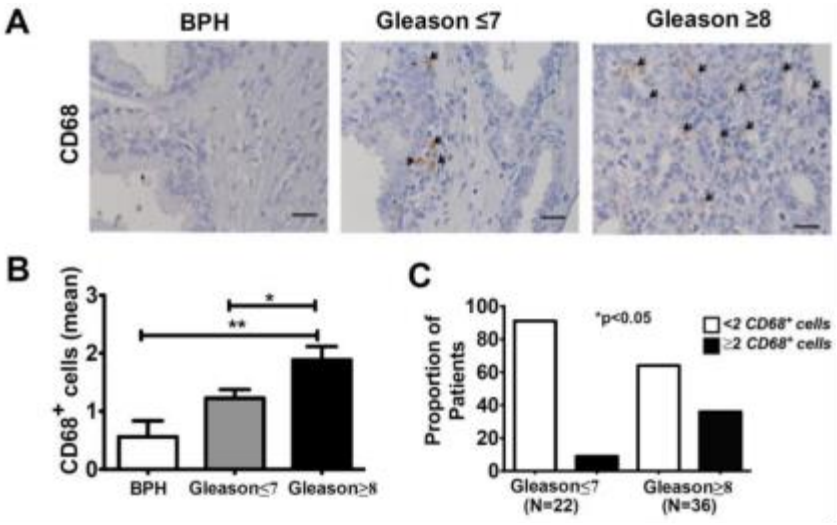

Figure 1: **Phagocytic CD68+ cells are positively associated with high Gleason scores** A) Representative images of CD68 immunohistochemistry in prostate cancer tissue microarray specimens including BPH (n=16), Gleason ≤7 (n=22) and Gleason ≥8 (n=36). Arrowheads (black) indicate cells positive for CD68. Images are taken at 400-fold magnification. B) Quantitative analysis of tissue specimens for the sum of CD68 + cells in four different fields of view. Measured images were taken at 20X for analysis. Data are mean ± S.E., *p<0.05, **p<0.01. C) The association of two or more CD68 + cells in tissue by patient's Gleason score was tested using Fishers exact test. Significance was set at *p<0.05.

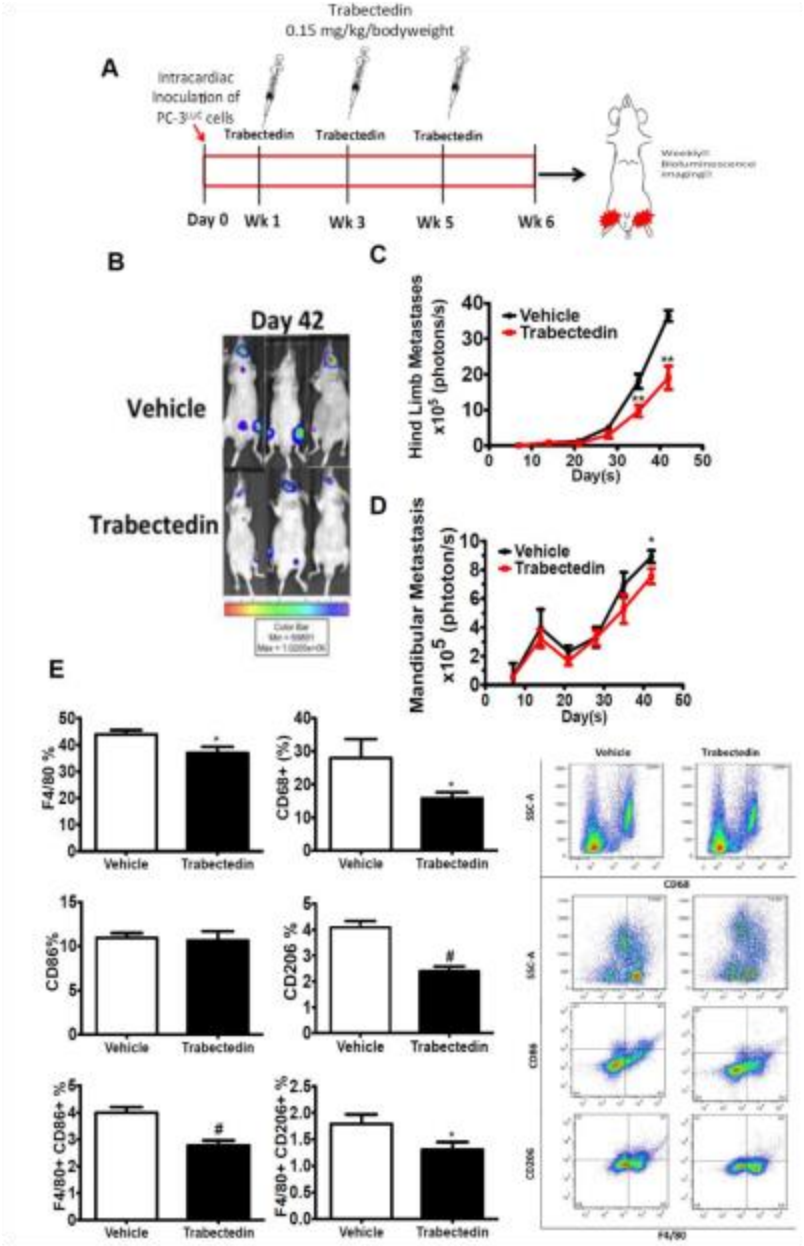

Figure 2**: M2-like monocytes and macrophages in experimental prostate cancer skeletal metastasis model** A) Schematic of the experimental design (therapeutic treatment regimen). Male athymic mice were divided into two groups and were injected with PC-3 Luc in the left ventricle of the heart. Trabectedin was subsequently administered (0.15 kg/mg/bodyweight) in three doses: 7 days after tumor inoculation, at week 3, and at week 5.B) Representative images of in vivo bioluminescence on day 42. C) Hind limb metastatic tumor growth was measured by weekly in vivo bioluminescence imaging. Data are mean ± S.E., **p<0.01 vs. vehicle.D) Mandibular metastatic tumor size was measured by weekly in vivo bioluminescence imaging. Data are mean ± S.E., *p<0.05 vs. vehicle. E) Bone marrow cells were isolated and analyzed for markers F4/80, CD68, CD86, and CD206 using flow cytometric analysis (representative flow cytometric analyses at right). Data are mean ± S.E., *p<0.05, #p <0.0001 vs. vehicle.

3. Prostate cancer preferentially metastasizes to the skeleton and the interaction between the bone and tumor microenvironment is critical to better understanding patient outcomes. Thus, changes in the bone microenvironment may be important variables that drive skeletal metastasis. Using the same chemotherapeutic trabectedin as in the prior study, the impact was directly studied on the bone microenvironment and examined effects on osteal macrophages, osteoblasts, osteoclasts, and bone mass. The data show that in addition to compromising macrophages, trabectedin also inhibits osteoblasts and significantly reduces bone mass. In addition to providing further information about changes in the bone microenvironment with trabectedin treatment, the results also suggest that patients receiving trabectedin may have reduced bone mass. This work has been published in the Journal of Bone and Mineral Research (BP Sinder first author) and the title is, "Bone Mass Is Compromised by the Chemotherapeutic Trabectedin in Association With Effects on Osteoblasts and Macrophage Efferocytosis". The full paper and results can be found in the appendix, and the abstract is included below to summarize:

"Macrophages have established roles supporting bone formation. Despite their professional phagocytic nature, the role of macrophage phagocytosis in bone homeostasis is not well understood. Interestingly, apoptosis is a pivotal feature of cellular regulation and the primary fate of osteoblasts is apoptosis. Efferocytosis (phagocytosis of apoptotic cells) is a key physiologic process for the homeostasis of many tissues, and is associated with expression of osteoinductive factors. To test effects of macrophage depletion and compromised phagocytosis on bone, 16-week-old male C57BL/6J mice were treated with trabectedin—a chemotherapeutic with established anti-macrophage effects. Trabectedin treatment reduced F4/80+ and CD68+ macrophages in the bone marrow as assessed by flow cytometry, osteal macrophages near the bone surface, and macrophage viability in vitro. Trabectedin treatment significantly reduced marrow gene expression of key phagocytic factors (Mfge8, Mrc1), and macrophages from treated mice had a reduced ability to phagocytose apoptotic mimicry beads. Macrophages cultured in vitro and treated with trabectedin displayed reduced efferocytosis of apoptotic osteoblasts. Moreover, efferocytosis increased macrophage osteoinductive TGF-β production and this increase was inhibited by trabectedin. Long-term (6-week) treatment of 16-week-old C57BL/6J mice with trabectedin significantly reduced trabecular BV/TV and cortical BMD. Although trabectedin reduced osteoclast numbers in vitro, osteoclast surface in vivo was not altered. Trabectedin treatment reduced serum P1NP as well as MS/BS and BFR/BS, and inhibited mineralization and Runx2 gene expression of osteoblast cultures. Finally, intermittent PTH 1-34 (iPTH) treatment was administered in combination with trabectedin, and iPTH increased trabecular bone volume fraction (BV/TV) in trabectedin-treated mice. Collectively, the data support a model whereby trabectedin significantly reduces bone mass due to compromised macrophages and efferocytosis, but also due to direct effects on osteoblasts. This data has immediate clinical relevance in light of increasing use of trabectedin in oncology."

4. Finally, as our above results suggest that cancer patients taking trabectedin may have reduced bone mass and be at risk of fracture, the impact of trabectedin on bone repair and fracture healing repair was also examined. Using a murine model of stress fracture healing, we examined the impact of trabectedin treatment on the fracture callus during bone healing. Results show that trabectedin reduces the callus size and amount of bone after 1 week of healing and suggest that trabectedin may compromise bone healing (Figure 3). This work is complimented by macrophage flow cytometry analysis, IHC staining for macrophages, and additional histologic analysis of bone healing effects. A manuscript describing this work is being written.

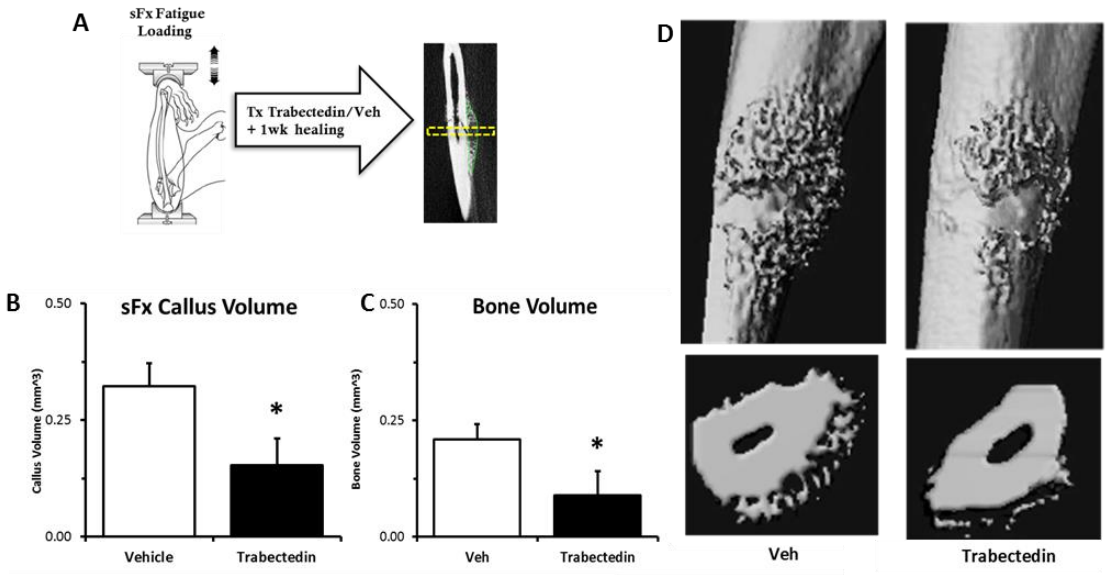

Figure 3: **Trabectedin Reduces Callus Size and Bone Volume During Bone Healing** A) Stress fracture (sFx) was induced in 16wk old C57BL/6J mice, immediately treated with trabectedin or vehicle (0.15mg/kg, iv), and callus outcomes assessed after 1wk of healing. B,C) Trabectedin treatment significantly reduced total callus volume, as well as total bone volume within the callus. D) Representative (median) images show impact of trabectedin on callus healing from both external and cross-sectional views with reduced bone and callus healing present in the trabectedin treated group. n=8/gp. *p<0.05.

What opportunities for training and professional development has the project provided?

The project has provided ample opportunity for training and professional development including one-on-one meetings with mentor Dr. Laurie McCauley as well as learning novel laboratory skills. Professional development has been afforded by attending on campus seminar series focused on skeletal research as well as skeletal cancers, attending and presenting at seminars on responsible conduct of research, and presenting data during group and departmental meetings. In addition, both the current (BP Sinder) and prior (JD Jones) PI's presented at Prostate Cancer project group meetings. Moreover, both the current (BP Sinder) and prior (JD Jones) PI's participated in guest lectures with Dr. Laurie McCauley on osteoclasts. The opportunity to present findings at national meetings as also supported by this grant.

How were the results disseminated to communities of interest?
Results published in Journal of Clinical Investigation and the Journal of Bone and Mineral Research. Additional articles are being submitted for publication and further disseminated once peer reviewed.

What do you plan to do during the next reporting period to accomplish the goals?
Nothing to report.

4. IMPACT:

What was the impact on the development of the principal discipline(s) of the project?
Recent work of this project has two major impacts. First, it highlighted the role of macrophages and efferocytosis on the bone and tumor microenvironment. In addition, this work also showed the negative impact of trabectedin treatment on bone and bone healing. **What was the impact on other disciplines?**
The main impact of this work on other disciplines is added knowledge on the role of macrophages and efferocytosis which may be translatable to the biology of other cancers and tissues.

What was the impact on technology transfer?
Nothing to report.

What was the impact on society beyond science and technology?
Nothing to report.

5. CHANGES/PROBLEMS:

Changes in approach and reasons for change
Nothing to report.

Actual or anticipated problems or delays and actions or plans to resolve them
Nothing to report.

Changes that had a significant impact on expenditures
Nothing to report.

Significant changes in use or care of human subjects, vertebrate animals, biohazards, and/or select agents
No significant changes
Significant changes in use or care of human subjects
No significant changes
Significant changes in use or care of vertebrate animals.
No significant changes
Significant changes in use of biohazards and/or select agents
No significant changes

6. **PRODUCTS:**

Journal publications.
Publications are previously referenced in the "accomplishments" section 3. A bibliography is provided below. PI's Sinder BP and Jones JD are highlighted in bold font.

Accepted Publications

Roca H, **Jones JD**, Purica MC, Weidner S, Koh AJ, Kuo R, Wilkinson, J, Wang Y, Diagnault-Newton S, Pienta K, Morgan T, Keller E, Nor J, Shea L, McCauley L. Apoptosis-induced CXCL5 accelerates inflammation and growth of prostate tumor metastases in bone. J Clin Invest. 2017. Accepted.

Sinder BP, Zweifler L, Koh AJ, Michalski MN, Hofbauer LC, Roca HR, McCauley LK. Bone Mass is Compromised by the ChemotherapeuticTrabectedin via Effects on Osteoblasts and Macrophage Efferocytosis. Journal of Bone and Mineral Research. 32 (10). 2017.

Manuscripts Actively Being Submitted or In Preperation

JD Jones, BP Sinder, FN Soki, AJ Koh, S Thiele, LC Hofbauer, S Daignault, H Roca, LK McCauley. Trabectedin Reduces Skeletal Prostate Cancer Tumor Size in Association with Effects on M2 Macrophages and Efferocytosis. *Actively being submitted.*

Sinder BP, Do J, Koh AJ, Roca HR, McCauley LK. The Chemotherapeutic Trabectedin Impacts Macrophages and Bone Healing. *In Preparation.*

Books or other non-periodical, one-time publications.
Nothing to report.

Other publications, conference papers, and presentations.
JD Jones
1. American Society for Investigative Pathology (ASIP) (San Diego, CA) - "Alternatively Activated Monocytes/Macrophages Support Prostate Cancer Skeletal Metastasis"
2. American Society for Bone and Mineral Research (Houston, TX) – "Alternatively Activated Monocyte and Macrophage Efferocytosis Support Prostate Cancer Skeletal Metastasis"
3. Case Western Reserve Research Symposium- "Macrophage Efferocytosis Supports Prostate Cancer Skeletal Metastasis"
4. American Society for Bone and Mineral Research (Denver CO). 2017. "Efferocytosis of Apoptotic Prostate Cancer Cells Induces Inflammation and Accelerates the Growth of Surviving Cancer Cells in Bone" Podium Presentation by Roca (JD Jones second author).
BP Sinder
5. American Society for Bone and Mineral Research (Denver, CO). 2017. "The Chemotherapeutic Trabectedin Negatively Impacts Osteal Macrophages, Bone Formation and Bone Healing". Poster Presentation by Sinder BP.

Website(s) or other Internet site(s).
Nothing to report.

Technologies or techniques.
Nothing to report.

Inventions, patent applications, and/or licenses
Nothing to report.

Other Products
Nothing to report.

7. PARTICIPANTS & OTHER COLLABORATING ORGANIZATIONS

What individuals have worked on the project?

Name:	*Benjamin Sinder*
Project Role:	*PI and Postdoctoral Researcher*
Researcher Identifier (e.g. ORCID ID):	*0000-0002-5795-154X*
Nearest person month worked:	*19*
Contribution to Project:	*Mr Sinder performed work analyzing the effect of trabectedin on macrophages and efferocytosis.*

Name:	*Jacqueline Jones*
Project Role:	*Prior (initial) PI and Postdoctoral Researcher*
Researcher Identifier (e.g. ORCID ID):	
Nearest person month worked:	*3*
Contribution to Project:	*Mrs Jones performed work analyzing the effect of trabectedin on macrophages and efferocytosis.*

Name:	*Lorenz C Hofbauer*
Project Role:	*collaborator*
Researcher Identifier (e.g. ORCID ID):	
Nearest person month worked:	n/a
Contribution to Project:	*Dr. Hofbauer contributed prostate cancer tissue arrays and trabectedin (therapeutic drug used in the study).*

Has there been a change in the active other support of the PD/PI(s) or senior/key personnel since the last reporting period?
Nothing to report.

What other organizations were involved as partners?
Nothing to Report

8. **SPECIAL REPORTING REQUIREMENTS**

No special reporting requirements.

9. **APPENDICES:**

Copies of two published journal articles supported by this work are attached.

Apoptosis-induced CXCL5 accelerates inflammation and growth of prostate tumor metastases in bone

Hernan Roca,[1] Jacqueline D. Jones,[1] Marta C. Purica,[1] Savannah Weidner,[1] Amy J. Koh,[1] Robert Kuo,[2] John E. Wilkinson,[3] Yugang Wang,[4] Stephanie Daignault-Newton,[5] Kenneth J. Pienta,[6] Todd M. Morgan,[4] Evan T. Keller,[4,7] Jacques E. Nör,[8,9,10] Lonnie D. Shea,[10] and Laurie K. McCauley[1,3]

[1]Department of Periodontics and Oral Medicine, University of Michigan School of Dentistry, Ann Arbor, Michigan, USA. [2]Department of Chemical Engineering, University of Michigan College of Engineering, Ann Arbor, Michigan, USA. [3]Department of Pathology, University of Michigan Medical School, Ann Arbor, Michigan, USA. [4]Department of Urology, University of Michigan Medical School, Ann Arbor, Michigan, USA. [5]Department of Biostatistics, Center for Cancer Biostatistics, University of Michigan, Ann Arbor, Michigan, USA. [6]Department of Urology, Johns Hopkins University School of Medicine, Baltimore, Maryland, USA. [7]Biointerfaces Institute, University of Michigan, Ann Arbor, Michigan, USA. [8]Department of Cariology, Restorative Sciences and Endodontics, University of Michigan School of Dentistry, Ann Arbor, Michigan, USA. [9]Department of Otolaryngology, University of Michigan Medical School, Ann Arbor, Michigan, USA. [10]Department of Biomedical Engineering, University of Michigan College of Engineering, Ann Arbor, Michigan, USA.

During tumor progression, immune system phagocytes continually clear apoptotic cancer cells in a process known as efferocytosis. However, the impact of efferocytosis in metastatic tumor growth is unknown. In this study, we observed that macrophage-driven efferocytosis of prostate cancer cells in vitro induced the expression of proinflammatory cytokines such as CXCL5 by activating Stat3 and NF-κB(p65) signaling. Administration of a dimerizer ligand (AP20187) triggered apoptosis in 2 in vivo syngeneic models of bone tumor growth in which apoptosis-inducible prostate cancer cells were either coimplanted with vertebral bodies, or inoculated in the tibiae of immunocompetent mice. Induction of 2 pulses of apoptosis correlated with increased infiltration of inflammatory cells and accelerated tumor growth in the bone. Apoptosis-induced tumors displayed elevated expression of the proinflammatory cytokine CXCL5. Likewise, CXCL5-deficient mice had reduced tumor progression. Peripheral blood monocytes isolated from patients with bone metastasis of prostate cancer were more efferocytic compared with normal controls, and CXCL5 serum levels were higher in metastatic prostate cancer patients relative to patients with localized prostate cancer or controls. Altogether, these findings suggest that the myeloid phagocytic clearance of apoptotic cancer cells accelerates CXCL5-mediated inflammation and tumor growth in bone, pointing to CXCL5 as a potential target for cancer therapeutics.

Introduction

The most common site of prostate cancer metastasis is bone, with an incidence of 65%–80% in patients with advanced disease (1). Once cancer cells spread to bone, they significantly alter normal bone remodeling, resulting in bone fractures, nerve compression, pain, and hypercalcemia (2). In bone, cancer cells find a protective and supportive microenvironment that promotes metastatic outgrowth. Prevention of bone metastasis is a major goal of treatment, and elucidation of the crucial factors contributing to the development of skeletal metastasis is key. Some mechanisms have been proposed, and monocytic myeloid cell populations attracted to the tumor microenvironment have been identified as critical mediators of inflammation (3, 4). One study found that $CD11b^+$ myeloid cells expressing integrin $\alpha_4\beta_1$ were mobilized to the skeletal tumor microenvironment via interaction with VCAM-1 expressed in breast tumor cells (5). Similarly, another breast cancer study showed that macrophages expressing $\alpha_4\beta_1$ promote cancer cell survival and lung metastasis (6), suggesting that this interaction may be essential for both cancer colonization and osseous progression.

The bone microenvironment is rich in factors that promote the mobilization, proliferation, and differentiation of proinflammatory cells, which interact with disseminated tumor cells, promoting survival and colonization. This occurs through multiple inflammation-mediated molecular mechanisms that originate feed-forward amplification loops between tumor cells, inflammatory cells, osteoblasts, osteoclasts, and bone marrow stromal cells to perpetuate a chronic inflammatory state (7).

A successful antiinflammatory therapy that targets tumor metastasis has been associated with reduced infiltration of bone marrow–derived myeloid cells and prometastatic macrophages (8). Recently a crucial role of bone macrophages in the progression of prostate cancer skeletal metastasis was demonstrated in vivo using models of conditional macrophage depletion (9). Furthermore, special attention has been dedicated to macrophage-directed cancer immunotherapy based on the transformation of macrophages from M2 to M1 type to elicit antitumor responses (10). These approaches have the potential to inhibit tumor progression and metastasis.

Persistent inflammation also exacerbates cell stress and tissue damage, causing apoptotic/necrotic cell death. The clearance of dying cells occurs mainly through phagocytosis by macro-

Authorship note: H. Roca and J.D. Jones contributed equally to this work.
Conflict of interest: The authors have declared that no conflict of interest exists.
Submitted: December 22, 2016; **Accepted:** October 17, 2017.
Reference information: *J Clin Invest*. https://doi.org/10.1172/JCI92466.

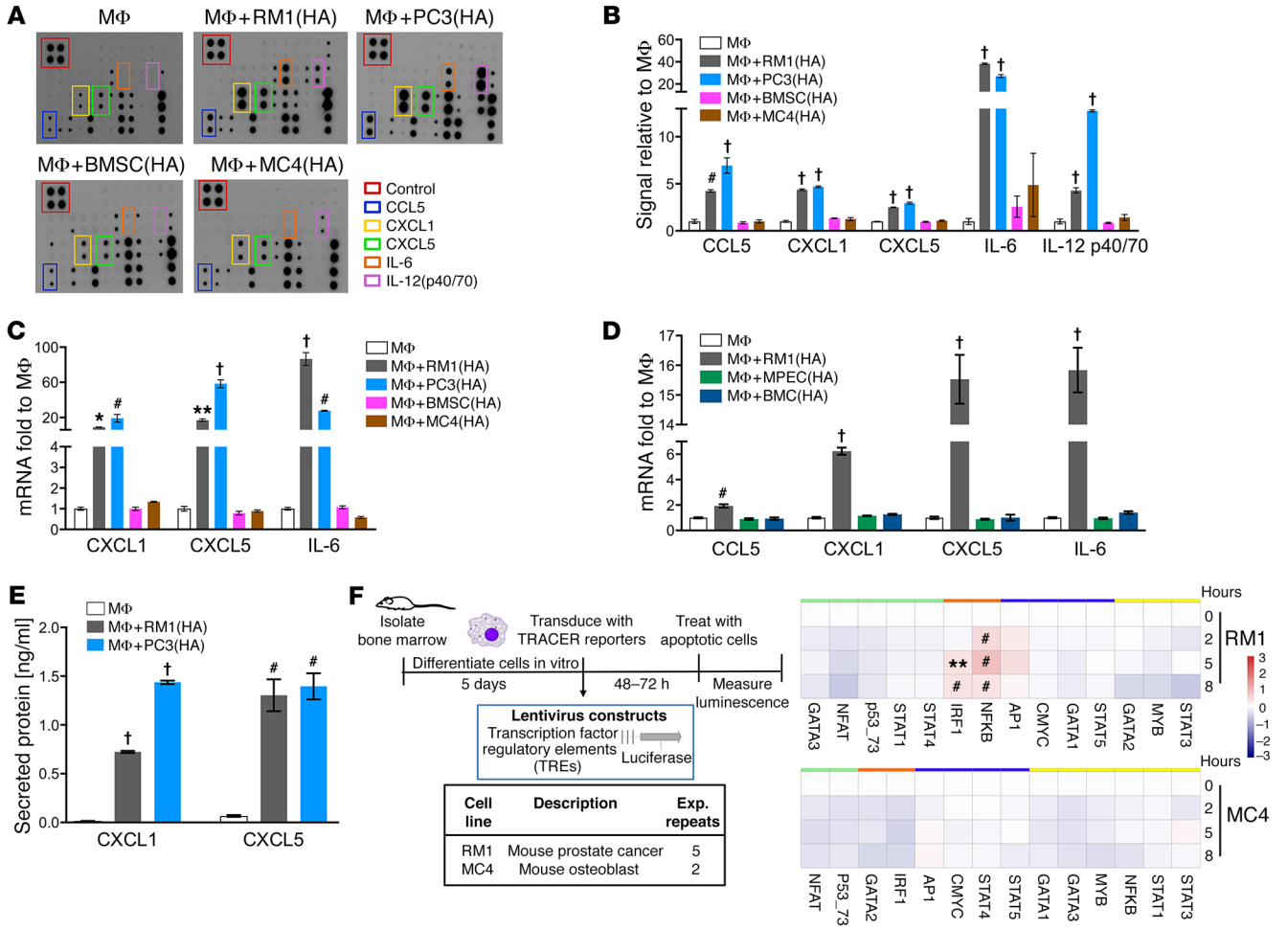

Figure 1. Inflammatory cytokine and transcription factor activation in cocultures of macrophages and highly apoptotic (HA) cells. (**A** and **B**) Supernatants were collected from macrophages (MΦs) alone or cocultured with RM1(HA), PC3(HA), BMSC(HA), or MC4(HA) cells for 18–20 hours and analyzed via inflammatory cytokine array. (**A**) Representative images. (**B**) Quantification of cytokines induced. (**C**) mRNAs isolated from cocultures described in **A** were analyzed by quantitative PCR (qPCR). (**D**) mRNAs isolated from MΦs alone or cocultured with RM1(HA), MPEC(HA), or BMC(HA) were analyzed by qPCR for indicated genes. (**E**) ELISA for total CXCL1 and CXCL5 levels in supernatants of MΦs alone or cocultured with RM1(HA) or PC3(HA). (**F**) Transcriptional activity cell arrays (TRACER). Analysis of bone marrow–derived MΦs transfected with transcription factor (TF) reporter constructs and cocultured with RM1(HA) or MC4(HA) cells. Data from experimental repeats (n = 5 and n = 2 independent experiments for RM1 for MC4, respectively) were combined. Measurements were $\log_2$-transformed and normalized to average intensity of control reporter and then to background. Finally, data were normalized to the initial reporter measurement for each treatment condition at 0 hours. Heatmaps show TF grouping according to cluster analysis for each cell line and the statistical significance, $^{**}P < 0.01$, $^{\#}P < 0.001$, determined using limma package. Data in **B**–**E** are mean ± SEM, n = 3 per group; $^{*}P < 0.05$, $^{**}P < 0.01$, $^{\#}P < 0.001$, $^{\dagger}P < 0.0001$ (1-way ANOVA).

phages and other cells (11). Phagocytosis of apoptotic cancer cells (termed efferocytosis) is a process often underestimated during tumor progression due to rapid clearance by phagocytes (11). Tumor cell death, significantly amplified by chemotherapies or other targeted therapies, triggers extensive efferocytosis, which has been suggested to accelerate further tumor growth at least in part by inducing M2-like macrophage polarization and resultant protumoral functions (12, 13).

Using in vivo models of skeletal tumor growth and apoptosis-inducible prostate cancer cells, the role of apoptotic cancer cell clearance in skeletal tumor progression was investigated. A critical role of efferocytosis-induced inflammation mediated by macrophage-derived CXCL5 was discovered as a novel mechanism underlying skeletal metastasis and a viable target for cancer therapeutics.

Results

Proinflammatory cytokines are induced in macrophages upon apoptotic cancer cell efferocytosis. Immunofluorescence and flow cytometric studies show that bone marrow–derived macrophages (MΦs) effectively efferocytose apoptotic cells (12, 14). We hypothesized that macrophages discriminate between different types of apoptotic cells and orchestrate a distinctive response accordingly. To investigate the production of proinflammatory cytokines, cocultures of macrophages and different highly apoptotic (HA) cells were analyzed (Supplemental Figure 1A; supplemental material available online with this article; https://doi.org/10.1172/JCI92466DS1). Two prostate cancer cell types (murine RM1 and human PC3) and 2 noncancer cell types (murine osteoblastic MC4 and murine primary bone marrow stromal cells [BMSCs]) were used. RM1 cells, derived from C57BL/6J mice, represent a valuable

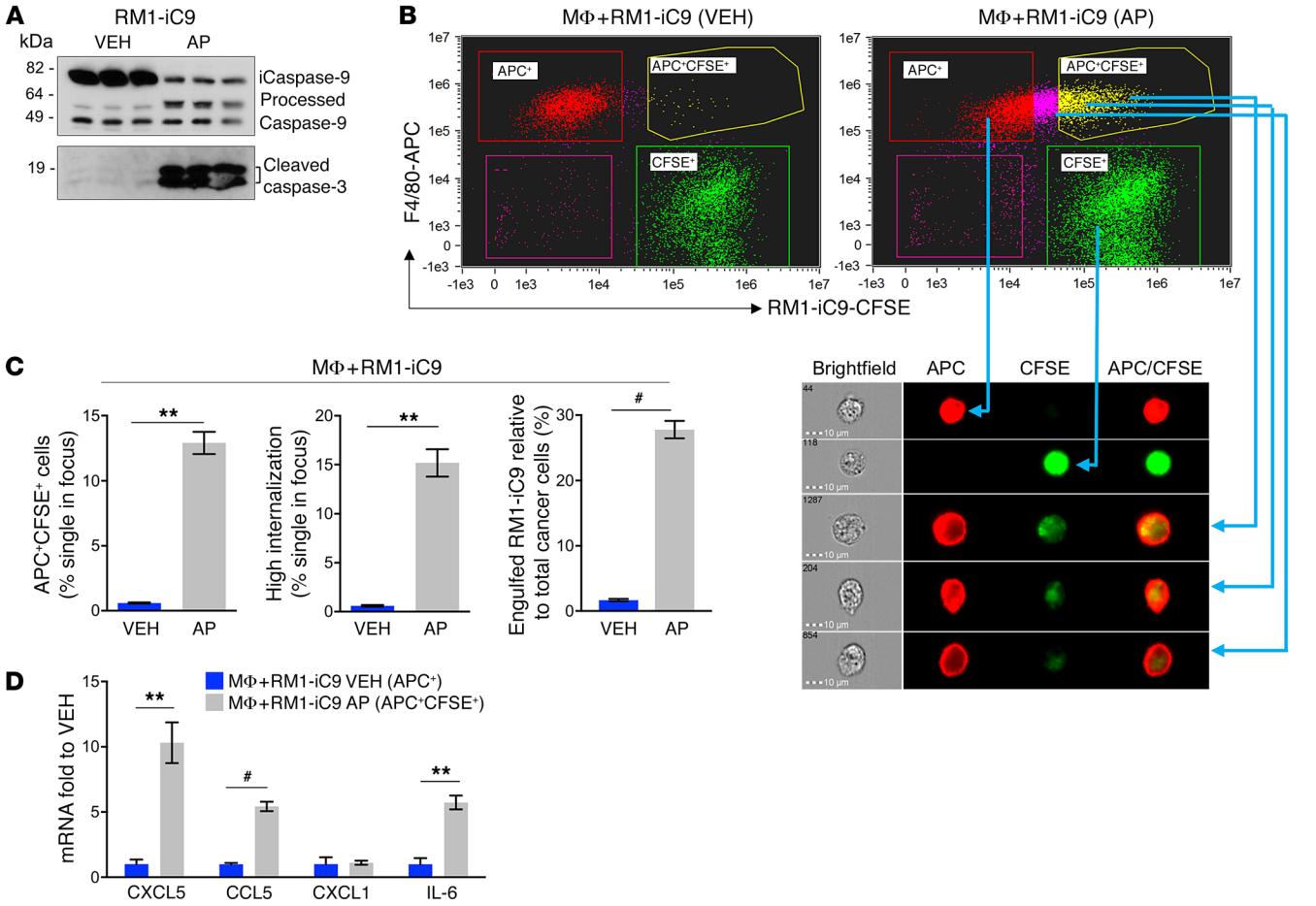

Figure 2. Efferocytosis of apoptosis-inducible prostate cancer RM1-iC9 cells. (**A**) Apoptosis-inducible RM1-iC9 cells were treated with VEH or AP and analyzed by Western blot for the activation of inducible caspase-9 (iC9) and apoptosis-associated caspase-3. AP treatment increased processed caspase-9 and cleaved caspase-3, reflecting apoptosis (see complete unedited blots in the supplemental material). (**B**) Bone marrow MΦs were cocultured with RM1-iC9 cells stained with Cell Trace–CFSE (Invitrogen), and treated with VEH or AP for 18 hours. The cocultures were stained with F4/80-APC antibody and analyzed by flow cytometry. Representative FACS images from ImageStream showing MΦs alone (APC$^+$, red gate), RM1-iC9 alone (CFSE$^+$, green gate), and 3 different examples of MΦs engulfing RM1-iC9 (APC$^+$CFSE$^+$, yellow gate). (**C**) Bar graphs indicating the percentage of efferocytic MΦs (APC$^+$CFSE$^+$ cells), MΦs with high internalization of RM1-iC9, and engulfed RM1-iC9 (APC$^+$CFSE$^+$) relative to total cancer cells (CFSE$^+$ plus APC$^+$CFSE$^+$) after treatment with VEH or AP. (**D**) mRNAs isolated from APC$^+$CFSE$^+$ gated cells (efferocytic MΦs) of MΦ+RM1-iC9(AP) and APC$^+$ gated cells (nonefferocytic MΦs) of MΦ+RM1-iC9 (VEH) samples were analyzed by qPCR for selected genes. Fold changes were expressed relative to the nonefferocytic MΦ values (VEH). Data in **C** and **D** are mean ± SEM, $n = 3$ per group; $^{**}P < 0.01$, $^{\#}P < 0.001$ (2-tailed Student's t test).

model for investigations of prostate cancer interactions with bone marrow stroma as they promote osteolytic lesions accompanied by periosteal bone deposition in immunocompetent C57BL/6J mice (9, 15). Human PC3 cancer cells, originally isolated from prostate cancer bone metastasis (16), have been used extensively for their ability to metastasize to the bone when injected in immunocompromised mice via intracardiac inoculation (17). Secreted proteins from cocultures of macrophages and apoptotic cells were analyzed using inflammation arrays (Figure 1A), and results were quantified and normalized relative to macrophage-alone controls (Figure 1B). The cytokines expressed upon efferocytosis of apoptotic cancer cells differed from noncancer cells, suggesting that different pathways were activated in macrophages. Cytokine activation of CCL5, CXCL1, CXCL5, IL-6, and IL-12(p40/p70) was observed in macrophages cocultured with apoptotic cancer cells, but not apoptotic noncancer cells. Upon noncancer apoptotic cell engulfment, CCL2 was the only cytokine significantly upregulated in macrophages interacting with apoptotic MC4 cells (Supplemental Figure 1B). Other cytokines, like CCL2 and MIP-1α, were increased in cocultures with PC3(HA) but not in cocultures with RM1(HA) cells, and a small increase in the proinflammatory cytokines sTNFRI and sTNFRII (soluble TNF receptors I and II) was observed for both RM1 and PC3 (Supplemental Figure 1B). Apoptotic cells alone showed reduced levels of cytokines compared with macrophages alone (Supplemental Figure 1C). Intriguingly, the proinflammatory factors CCL5, CXCL1, CXCL5, and IL-6 have been shown to have tumor-promoting functions in different contexts (18, 19). To determine the transcriptional regulation in macrophages, quantitative PCR mRNA expression analyses were performed for CXCL1, CXCL5, and IL-6 to compare macrophage responses to the different apoptotic cells. Figure 1C indicates that these cytokines were transcriptionally upregulated in macrophages interacting with apoptotic cancer cells in contrast with noncancer cells, which correlates with the cytokine array results. Since pros-

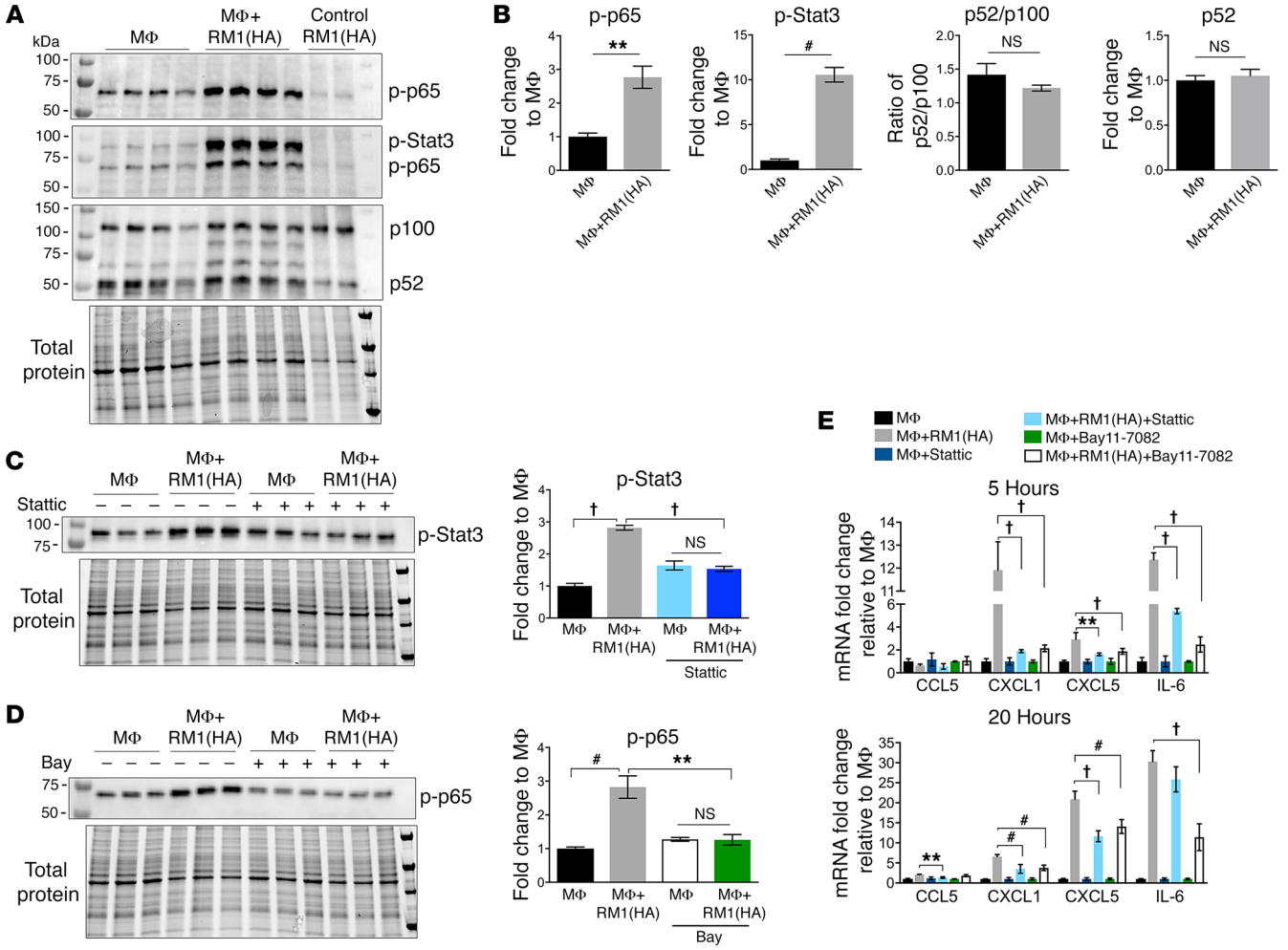

Figure 3. Efferocytosis-induced activation of Stat3 and NF-κB signaling mediates inflammatory response in macrophages. (**A**) MΦs were cocultured 20 hours alone or with apoptotic RM1(HA) cells. Protein from cocultures was analyzed by Western blot for activation of NF-κB and Stat3 signaling using consecutively the following antibodies (panels from top): phospho–NF-κB(p65) [p–NF-κB(p65)], p-Stat3, and p100/p52. Bottom panel shows total protein for each sample. (**B**) Protein bands in the blots were quantified and normalized to total protein for each sample. Graphs depict the fold changes for p-p65, p-Stat3, p52/p100 ratio, and p52 relative to MΦ signal, respectively. (**C**) Stattic, a selective inhibitor of Stat3 activation, was incubated with MΦs (12.5 μM) for 1 hour, then removed before coculture with RM1(HA) for 5 hours. Protein was analyzed by Western blot using the p-Stat3 antibody. (**D**) Bay11-7082, an inhibitor of NF-κB signaling, was preincubated with MΦs (20 μM) for 1 hour before coculture with RM1(HA) for 5 hours. Protein was analyzed by Western blot using the p-p65 antibody. Graphs in **C** and **D** depict the quantification of p-Stat3 and p-p65 signals normalized to total protein (lower panel) relative to the average MΦ control (VEH), respectively. See complete unedited blots in the supplemental material. (**E**) mRNAs were isolated from cocultures at 5 and 20 hours of incubation as described in the experiments in **C** and **D** and analyzed by qPCR for indicated genes. Graphs show the fold change relative to MΦ control for each group. Data in **B** are mean ± SEM, $n = 4$ per group (2-tailed Student's t test), or $n = 3$ per group in **C**–**E** (1-way ANOVA); $^{**}P < 0.01$, $^{\#}P < 0.001$, $^{\dagger}P < 0.0001$.

tate cancer cells are of epithelial origin, we investigated whether the inflammatory responses induced in macrophages were a result of their interaction with apoptotic epithelial cells. Similarly to the experiments above (Supplemental Figure 1A), we used apoptotic mouse primary prostate epithelial cells (MPECs), apoptotic total bone marrow cells (BMCs) (isolated from mouse tibiae), or apoptotic RM1 cells (all originated from C57BL/6J mice) in cocultures with bone macrophages to analyze changes in gene expression of the different inflammatory cytokines (CCL5, CXCL1, CXCL5, and IL-6). Only apoptotic RM1 cancer cells were capable of inducing an inflammatory response in bone marrow macrophages (Figure 1D). ELISA evaluation for CXCL1 and CXCL5 proteins in the coculture media for apoptotic cancer cells (Figure 1E) confirmed the cytokine array results and aligned with the mRNA analyses. Altogether, these results suggest that the clearance of apoptotic cells by macrophages induced a selective response dependent on the cell type engulfed and a common inflammatory expression pattern in macrophages efferocytosing apoptotic cancer cells.

To investigate the transcription factor activity in macrophages in response to the apoptotic cells, we used TRACER (transcriptional activity cell array) technology (Figure 1F and ref. 20). The activity of 13 transcription factors was investigated in cocultures with apoptotic RM1 or MC4, 2 cell lines that induced a differential response in macrophages. Macrophages were transduced with a reporter luciferase construct containing the DNA binding site for each transcription factor or a control vector and the lucif-

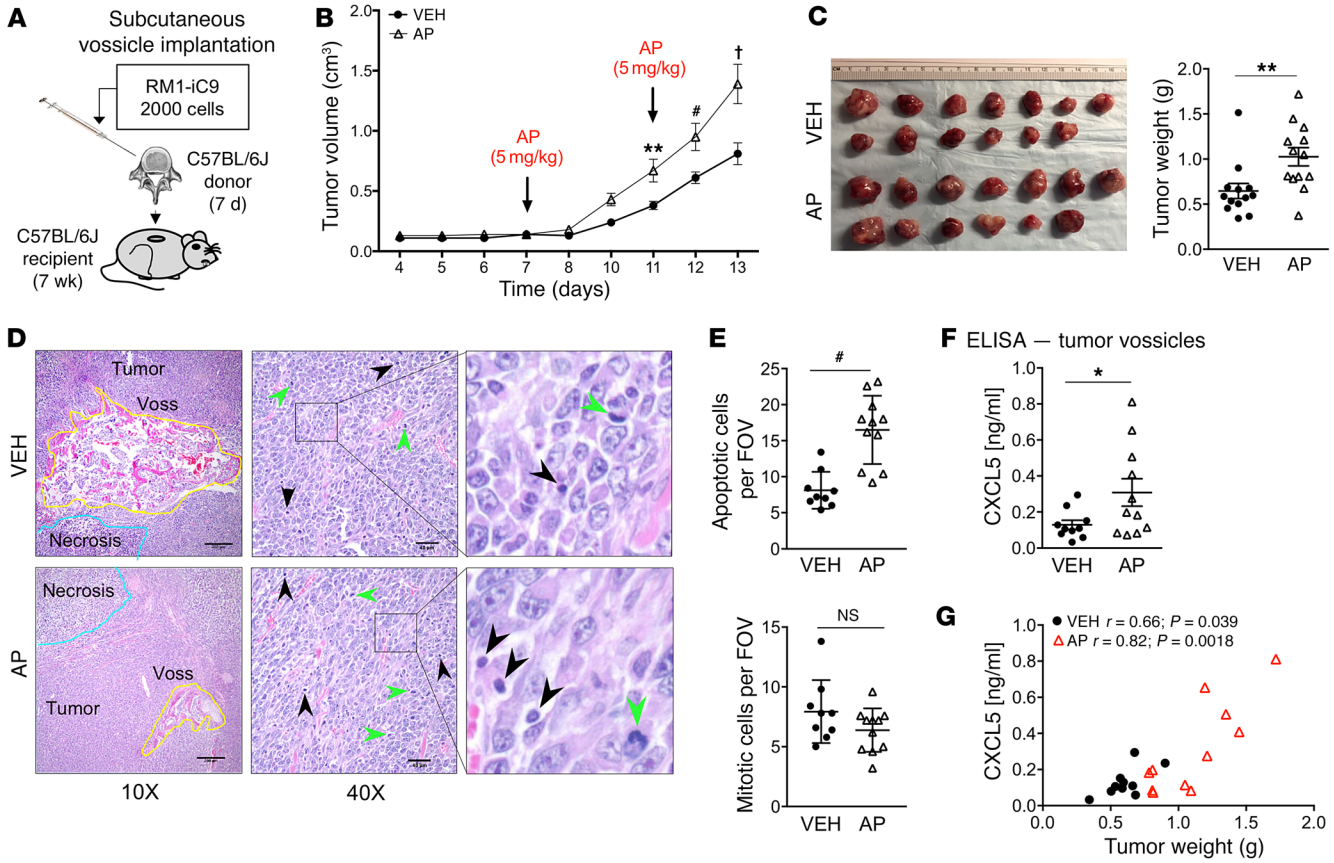

Figure 4. In vivo syngeneic osseous implant tumor model. Vertebral bodies (vossicles) from C57BL/6J donor mice (7-day-old males) were inoculated with RM1-iC9 cells, and subcutaneously implanted in C57BL/6J recipient mice (7-week-old males). Mice were randomly divided in 2 groups and treated with VEH or AP to induce apoptosis in RM1-iC9 cells. (**A**) Experimental design for tumor vossicle model. (**B**) Tumor volumes were measured by caliper every 1–2 days starting at day 4. RM1-iC9 tumor vossicle volumes were compared between VEH and AP; $n = 13$ per group. Data are mean ± SEM; $^{**}P < 0.01$, $^{\#}P < 0.001$, $^{\dagger}P < 0.0001$ vs. VEH (2-way ANOVA). (**C**) Images of RM1-iC9 VEH- and AP-treated tumor vossicles. Tumor weight (g) was measured at sacrifice, 13 days after implantation; $n = 13$ per group. (**D**) Representative H&E images of tumor vossicles showing vossicle fragments surrounded by tumor cells at ×10 (scale bars: 200 μm) and ×40 (scale bars: 40 μm) original magnifications. Areas of necrosis are highlighted by blue lines in the ×10 images. Apoptotic (black arrowheads) and mitotic cells (green arrowheads) are indicated at ×40 original magnification. (**E**) Apoptotic and mitotic cells were quantified (by a trained pathologist) inside non-necrotic tumor areas (5 fields at ×20 per tumor vossicle sample); VEH ($n = 9$) and AP ($n = 11$). (**F**) CXCL5 ELISA analysis of total protein lysates from VEH- ($n = 10$) and AP-treated ($n = 11$) tumor vossicles. (**G**) Graphs depicting the correlation between CXCL5 protein (determined by ELISA) and tumor weight. The Pearson correlation coefficient (r) and P values are indicated. Data in **C**, **E**, and **F** are mean ± SEM; $^{*}P < 0.05$, $^{**}P < 0.01$, $^{\#}P < 0.001$ (2-tailed Student's t test).

erase activity monitored over time in MΦ, MΦ+RM1(HA), and MΦ+MC4(HA). The results were normalized to macrophages alone and to the 0 hour (initial time) (Figure 1F). NF-κB and IRF1 were activated in MΦ+RM1(HA) but not in MΦ+MC4(HA) cocultures. Both transcription factors activate inflammatory responses and in some contexts cooperate with the activation of proinflammatory cytokines (21, 22). These findings correlate with the differential inflammatory response of macrophages in the cocultures with the apoptotic prostate cancer RM1 and the noncancer MC4 cells (Figure 1, A–C). Although Stat3 activation was not detected in the TRACER assays, other studies have suggested activation of this pathway by efferocytosis (12). It is possible that the specific Stat3 regulatory elements in the construct may require additional enhancer sequences to achieve activation upon efferocytosis.

Efferocytosis induces an inflammatory response via activation of Stat3 and NF-κB signaling. To better understand the role of efferocytosis, we generated apoptosis-inducible prostate cancer cells, RM1-iC9, from murine RM1 cells using the viral construct for inducible caspase-9 (iC9) (23). The induction of apoptosis and resultant caspase-3 activation were validated by treatment with the dimerizer drug AP20187 (AP) or control vehicle (VEH) followed by Western blot analysis of cell extracts (Figure 2A). Formation of processed caspase-9 and corresponding cleaved caspase-3 confirmed apoptosis activation in AP-treated cells. To verify that the inducible apoptotic RM1-iC9 cells were able to be efferocytosed, cells were prelabeled with CFSE dye, cocultured with macrophages, and treated with VEH or AP. After 16–18 hours the cells were collected, labeled with F4/80-APC antibody, and analyzed using the ImageStream flow cytometer (Abcam), which provides microscopic event images. Double-positive $APC^{+}CFSE^{+}$ cells indicate efferocytic macrophages (macrophages engulfing apoptotic RM1-iC9 cells) as depicted in Figure 2B (yellow gate). The $APC^{+}CFSE^{+}$ gate exhibited images with green apoptotic cancer cells engulfed by red $F4/80^{+}$ macrophages (Figure 2B) with

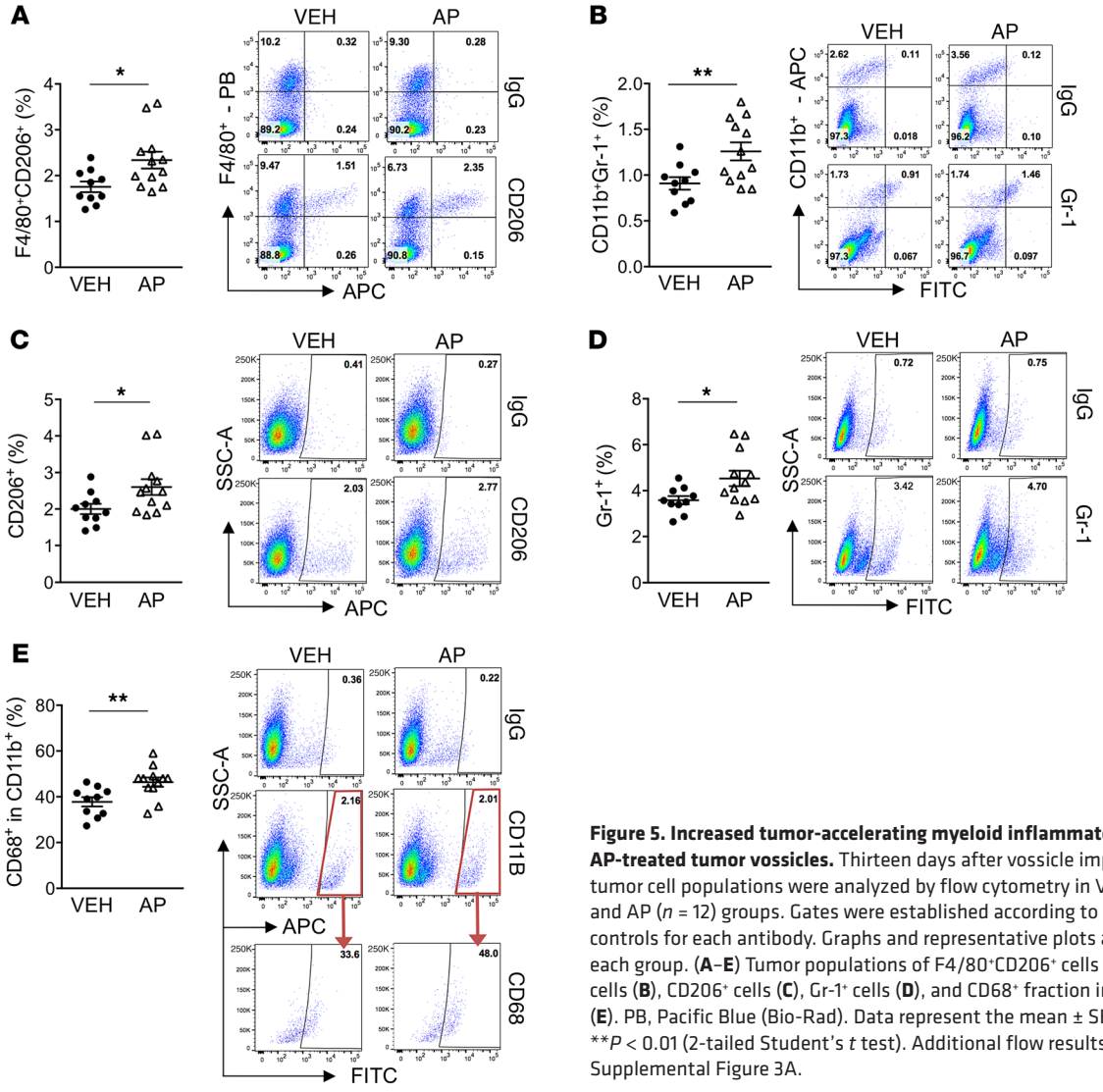

Figure 5. Increased tumor-accelerating myeloid inflammatory cells in AP-treated tumor vossicles. Thirteen days after vossicle implantation, tumor cell populations were analyzed by flow cytometry in VEH (n = 10) and AP (n = 12) groups. Gates were established according to IgG isotype controls for each antibody. Graphs and representative plots are shown for each group. (**A**–**E**) Tumor populations of F4/80$^+$CD206$^+$ cells (**A**), CD11b$^+$Gr-1$^+$ cells (**B**), CD206$^+$ cells (**C**), Gr-1$^+$ cells (**D**), and CD68$^+$ fraction in CD11b$^+$ cells (**E**). PB, Pacific Blue (Bio-Rad). Data represent the mean ± SEM; *P < 0.05, **P < 0.01 (2-tailed Student's t test). Additional flow results are shown in Supplemental Figure 3A.

high internalization, indicating efferocytosis. In the APC$^+$CFSE$^+$ gate, efferocytosis was observed at different stages of digestion correlating to the position of the cell in the plot. The brightest cells in the CFSE axis showed less digested cancer cells inside macrophages (Figure 2B). As expected, the percentage of cells (gated from single cells in focus) with high internalization was strikingly higher in the samples treated with AP relative to VEH (Figure 2C). Furthermore, the percentages of highly internalized cells were similar to the percentages of cells gated as APC$^+$CFSE$^+$, validating that this gate demonstrates that efferocytosis increased with the induction of apoptosis in cancer cells. When apoptosis was induced with AP, the proportion of engulfed RM1-iC9 cells relative to total cancer cells was approximately 30%, compared with less than 5% when the cells were treated with VEH (Figure 2C). Macrophages from the APC$^+$CFSE$^+$ gate, which had been cocultured with apoptosis-induced RM1-iC9 (AP-treated) cells, were sorted by flow cytometry and compared with APC$^+$-gated macrophages sorted from VEH samples. Quantitative PCR analyses revealed higher (5- to 10-fold) mRNA expression of the proinflammatory cytokines CXCL5, CCL5, and IL-6 in efferocytic macrophages (APC$^+$CFSE$^+$-sorted) as compared with nonefferocytic (APC$^+$-sorted) macrophages (Figure 2D).

Simultaneous activation of Stat3 and NF-κB signaling in the tumor microenvironment has been identified as a critical element of inflammation-associated tumor progression (24, 25), and here, NF-κB was identified as a critical transcription factor induced in efferocytic macrophages (Figure 1F). Thus the increase in phosphorylation/activation of NF-κB(p65) and Stat3 occurring in macrophages via efferocytosis of apoptotic RM1 cells was further investigated. Protein lysates isolated from cocultures of macrophages and RM1(HA) cells were analyzed by Western blot and quantified. Figure 3A depicts consecutive blotting of the membrane with antibodies for phosphorylated (p) p65, p-Stat3, and NF-κB2(p100/p52), respectively. Quantification of Western bands normalized to total protein in each lane (bottom panel in Figure 3A) showed activation (phosphorylation) of both canonical NF-κB(p65) (p-p65) and Stat3 (p-Stat3) signaling in efferocytic macrophages (Figure 3B). No significant changes in the processing of NF-κB2(p100) precursor to produce p52 (noncanonical NF-κB signaling) were induced by efferocytosis (Figure 3B), which suggests the predom-

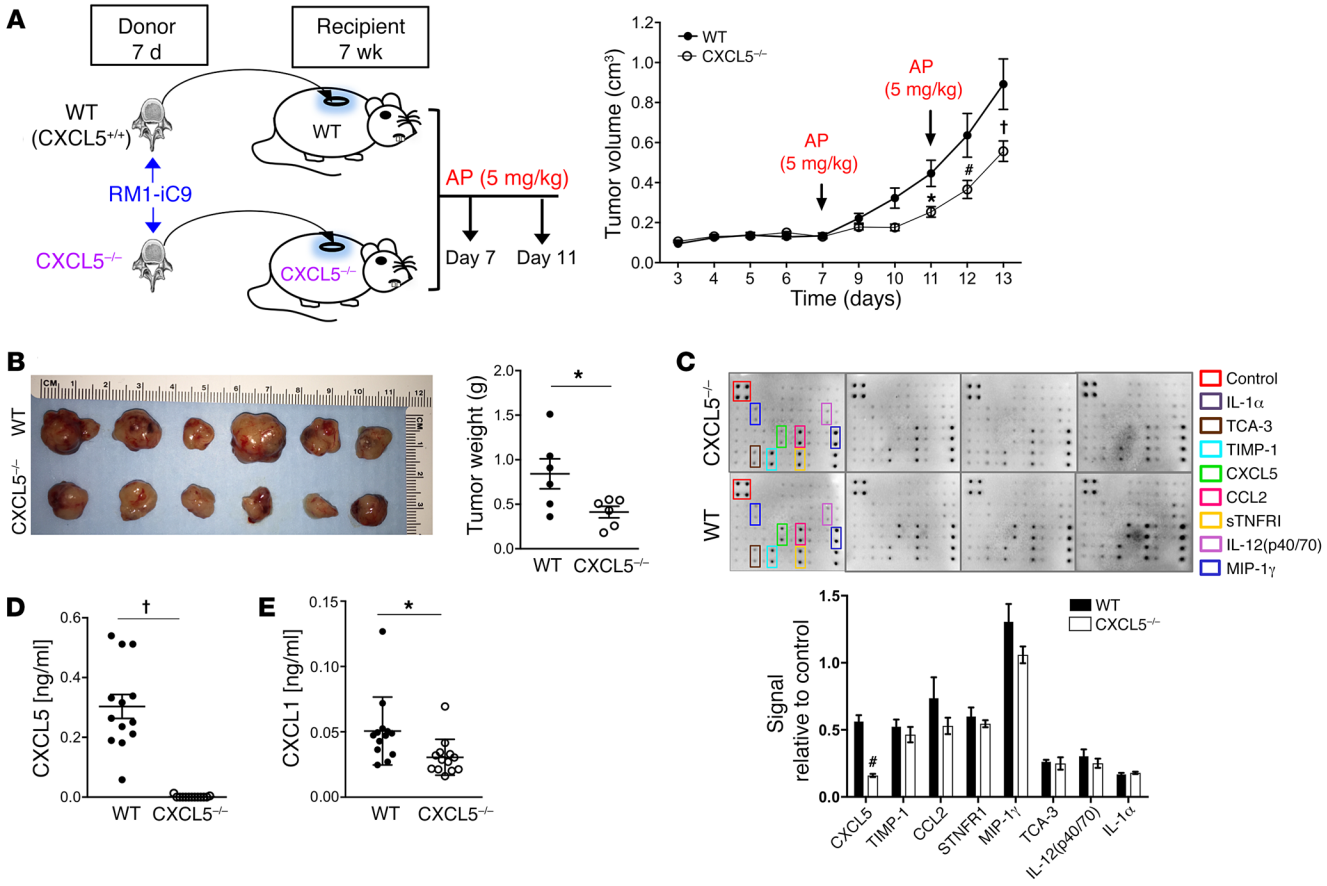

Figure 6. Prostate cancer growth in bone vossicles is hindered in CXCL5$^{-/-}$ mice. (**A**) WT (CXCL5$^{+/+}$) and CXCL5$^{-/-}$ recipient mice (7wk males) were implanted subcutaneously with RM1-iC9 inoculated vossicles isolated from WT or CXCL5$^{-/-}$ donor mice (7d males), respectively. Recipient mice from both groups were treated with AP at days 7 and 11 to induce apoptosis. Tumor volumes were quantified. An independent experiment with similar results is shown in Supplemental Figure 4A. Data are mean ± SEM; $^{*}P < 0.05$, $^{\#}P < 0.001$, $^{\dagger}P < 0.0001$ vs. WT controls (2-way ANOVA). (**B**) Gross image of tumors and graph of quantified tumor weights; $n = 6$ per group. (**C**) Total protein lysates of tumor vossicles from WT and CXCL5$^{-/-}$ mice were analyzed via inflammatory cytokine array. Quantification of cytokines expressed is represented as signal relative to the positive controls in the array; $n = 4$ independent arrays per group. (**D** and **E**) Protein lysates were analyzed by ELISA for the expression of CXCL5 (**D**) and CXCL1 (**E**) in the tumor vossicles of WT and CXCL5$^{-/-}$ mice; $n = 13$ per group. Data in **B**–**E** are mean ± SEM; $^{*}P < 0.05$, $^{\#}P < 0.001$, $^{\dagger}P < 0.0001$ (2-tailed Student's t test).

inant role of canonical signaling in the efferocytic inflammatory response. The apoptotic RM1-only lysates demonstrated insignificant signals for p-Stat3 or p-p65, which is consistent with the apoptotic stage of these cells.

To evaluate the dependence of Stat3 and NF-κB in inflammatory cytokine production, cocultures of macrophages and apoptotic RM1 cells were treated with the small-molecule inhibitors Stattic (Stat3 phosphorylation inhibitor; ref. 26) and Bay11-7082 (IκBα phosphorylation inhibitor; refs. 27, 28). Figure 3, C and D, demonstrates the inhibition of p-Stat3 and p-p65 after 5 hours of coculture pretreated with Stattic or Bay11-7082, respectively. Neither Stattic nor Bay11-7082 inhibited efferocytosis (Supplemental Figure 2A); however, both inhibitors significantly mitigated proinflammatory cytokine expression in macrophages at 5 and 20 hours of coculture (Figure 3E).

Treatment with emetine, an IκBα phosphorylation inhibitor (29), reduced efferocytosis in cocultures of macrophages with apoptosis-induced RM1-iC9 (Supplemental Figure 2B). This correlates with Supplemental Figure 2, C and D, which shows that emetine blocked the AP-induced increase of both p–NF-κB(p65) and p-Stat3 in the F4/80^{+} macrophage population. Furthermore, Ly6B (Ly6-B.2 or antigen 7/4), a bone marrow–derived inflammatory macrophage antigen (30), was increased when efferocytosis was activated with the AP dimerizer (Supplemental Figure 2E), while inhibition of efferocytosis with emetine reduced Ly6B, which is consistent with the inflammatory response of macrophages upon efferocytosis of apoptotic cancer cells. However, emetine inhibited not only p–NF-κB(p65) but also p-Stat3 and efferocytosis, differing from the Bay11-7082 inhibitor results. Therefore, the combined effect of Stattic and Bay11-7082 on efferocytosis was determined. Pretreatment of macrophages (1 hour) with the combination of these inhibitors (same concentrations used in Supplemental Figure 2A) resulted in a complete abrogation of efferocytosis (Supplemental Figure 2F). These findings suggest that the effect of emetine on efferocytosis may be due do a simultaneous blocking of Stat3 and NF-κB activation.

Altogether these findings correlate efferocytosis with persistent inflammation within the tumor microenvironment via activation of Stat3 and NF-κB signaling in macrophages.

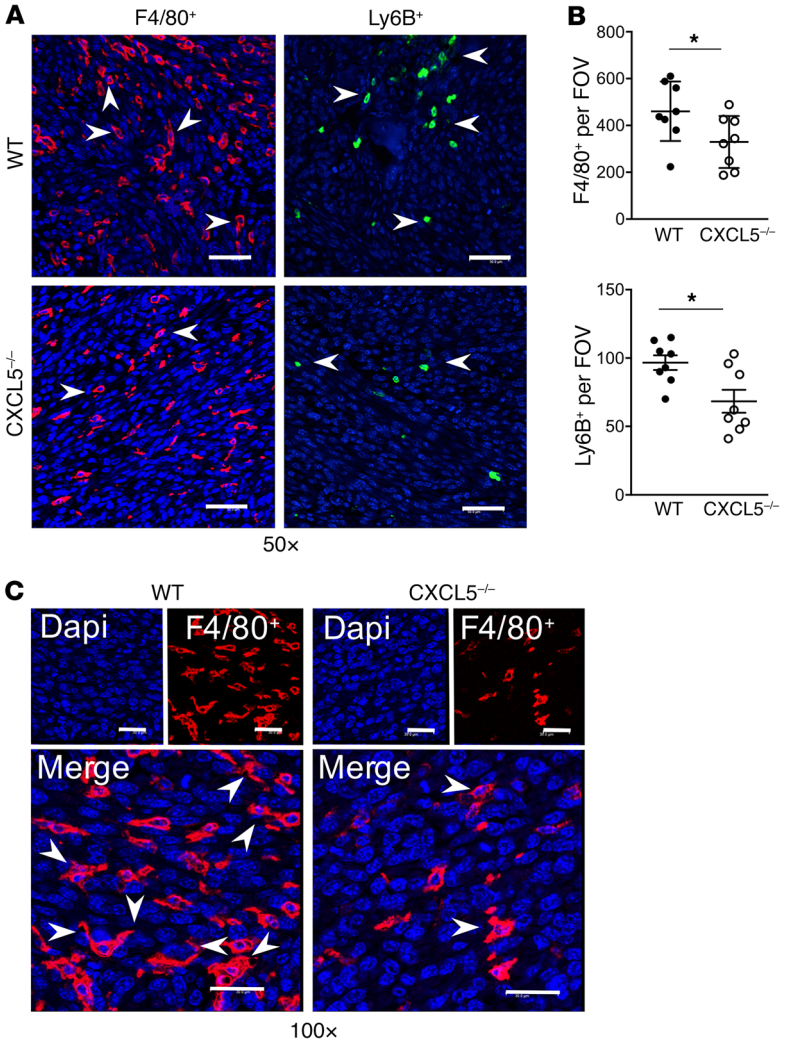

Figure 7. F4/80⁺ and Ly6B⁺ infiltration into tumor vossicles is hindered in CXCL5$^{-/-}$ mice. (**A**) Representative fluorescence images of F4/80⁺ (Opal 570) and Ly6B⁺ (Opal 520) cells in tumor vossicle sections from WT and CXCL5$^{-/-}$ mice at ×50 original magnification (scale bars: 50 μm). (**B**) Quantification of F4/80⁺ and Ly6B⁺ staining (4 fields at ×10 per tumor vossicle sample); n = 8 per group. (**C**) Macrophage morphology at ×100 original magnification (scale bars: 30 μm) showing some MΦs with extended arms (engulfing-like shape) surrounding large nuclei (blue, DAPI) typical of cancer cells. Image depicts the WT and CXCL5$^{-/-}$ MΦs (red) infiltrating the tumor. Data in **B** are mean ± SEM; *P < 0.05 (2-tailed Student's t test).

Cancer cell death accelerates tumor progression and increases tumor CXCL5 levels. To investigate how efferocytosis of cancer cells affects prostate cancer tumor progression in bone, an osseous implant vossicle model was used (9, 17, 31). Apoptosis-inducible RM1-iC9 cells were coimplanted with vertebral bodies (vossicles) of 7-day-old C57BL/6J mice into the subcutaneous compartment of 7-week-old C57BL/6J mice (Figure 4A). Tumors were repeatedly measured, and in the first 7 days no significant change in tumor volume was observed (Figure 4B). At day 7 after implantation, mice were randomized into 2 groups that were injected i.p. with VEH or the AP dimerizer to induce apoptosis in the RM1-iC9 cancer cells and subsequent efferocytosis. Tumor measurements revealed that induction of cancer cell apoptosis accelerated tumor growth, which was significant 4 days after AP treatment (day 11; Figure 4B). Apoptosis was induced again at day 11, and tumor growth continued to accelerate (days 12 and 13). At study end (day 13), tumor vossicles were collected, and tumor weight was significantly increased in the AP group compared with VEH (Figure 4C). Representative images of H&E tumor vossicle sections show bone structures surrounded by tumor cells as well as the presence of necrotic areas and apoptotic and mitotic cells in both VEH and AP tumors (Figure 4D). Analysis of tumor sections showed significantly higher apoptotic cell numbers in the AP-treated tumors relative to VEH, while no significant changes were observed in mitotic cell numbers between groups (Figure 4E). Considering that mice were sacrificed 2 days after the last AP treatment, it was expected that a major proportion of apoptotic cells would be cleared. Nevertheless, this result validates the effectiveness of AP treatment for the induction of cancer cell apoptosis in vivo.

As described above (Figure 1), in vitro results showed that CXCL5 was highly induced in macrophages upon efferocytosis of cancer cells. CXCL5 expression has been shown to correlate with prostate cancer progression and metastasis and is associated with stromal inflammation (32). To investigate whether expression of proinflammatory CXCL5 correlates with the induction of apoptosis in AP-treated mice, total protein from tumor vossicles was collected and analyzed by ELISA. As observed in Figure 4F, a significant increase in CXCL5 was detected in the AP-treated group, aligning with induction of apoptosis and consequent efferocytosis. A significant correlation between tumor weight and CXCL5 concentrations was found for both VEH- and AP-treated tumor vossicle groups (Figure 4G).

The immune cell composition of tumor vossicles was analyzed via flow cytometry. The AP-treated group (induced efferocytosis) showed significantly increased F4/80⁺CD206⁺ myeloid cells (Figure 5A), which characterizes M2-like macrophages (33). Other myeloid cells also showed increased infiltration in the AP-treated tumor vossicles, including: CD11b⁺Gr-1⁺ (monocytic/granulocytic cells associated with tumor progression and antitumor immunity) (34, 35) (Figure 5B), total CD206⁺ and Gr-1⁺ (characterizes inflammatory monocytes/granulocytes; ref. 36) (Figure 5, C and D), and CD68⁺ within the CD11b⁺ population (marker of phagocytic myeloid cells; aligns with higher efferocytosis induced by apoptosis) (Figure 5E). Other flow results are shown in Supplemental Figure 3A. Furthermore, whole blood count of VEH- and AP-treated mice revealed no significant differences (Supplemental Figure 3B), suggesting that the results observed in the tumor microenvironment are local and not related to general changes in the circulating monocytes/neutrophils.

CXCL5, a crucial inflammatory-microenvironment cytokine that accelerates tumor progression. As CXCL5 was found to increase with cancer cell death and efferocytosis in the tumor

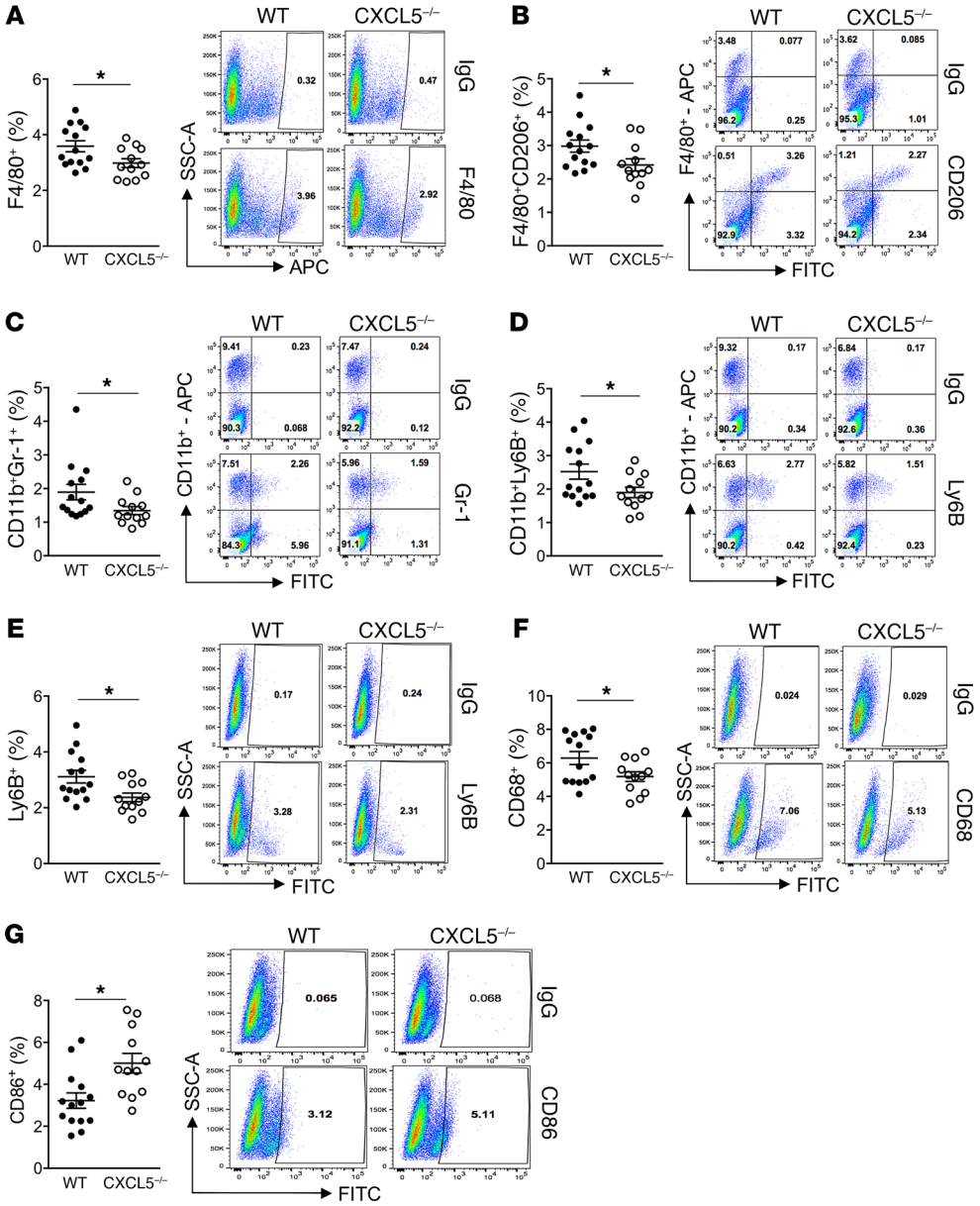

Figure 8. Flow cytometry analysis of WT and CXCL5$^{-/-}$ tumor vossicles. Changes in tumor vossicle cell populations of F4/80$^+$ cells (**A**), F4/80$^+$CD206$^+$ cells (**B**), CD11b$^+$Gr-1$^+$ cells (**C**), CD11b$^+$Ly6B$^+$ cells (**D**), Ly6B$^+$ cells (**E**), CD68$^+$ cells (**F**), and CD86$^+$ cells (**G**) in WT (n = 14) and CXCL5$^{-/-}$ (n = 12) mice are represented. Gates were established according to IgG isotype controls for each antibody. Representative plots for each group are shown. Additional flow results are shown in Supplemental Figure 4C. Data are mean ± SEM; *P < 0.05 (2-tailed Student's t test).

microenvironment, the specific role of CXCL5 was addressed using CXCL5$^{-/-}$ mice in the vossicle implant model. To avoid any possible compensation with CXCL5 produced by immune cells, vossicles from CXCL5$^{-/-}$ mice were inoculated with the RM1-iC9 cells and implanted in CXCL5$^{-/-}$ mice. Similarly, WT (CXCL5$^{+/+}$) vossicles were implanted in WT mice (Figure 6A). To induce apoptosis and efferocytosis and hence increase the expression of CXCL5 (in accordance with results in Figure 4), both groups were injected with AP at days 7 and 11 as described. Figure 6A and Supplemental Figure 4A demonstrate tumor growth deceleration in the CXCL5$^{-/-}$ mice compared with WT, and CXCL5$^{-/-}$ mouse tumors had significantly reduced weight at study end (Figure 6B).

Proinflammatory cytokine profiling in tumors from WT and CXCL5$^{-/-}$ mice revealed that CXCL5 was the only cytokine that was significantly different with distinctively lower levels in the CXCL5$^{-/-}$ mice (Figure 6C). These results were confirmed by ELISA (Figure 6D) and demonstrate that the major contribution of CXCL5 in the tumor microenvironment originated from the host and not from the tumor. However, since the cytokine array has limited detection, a more sensitive ELISA revealed a significant decrease in CXCL1 levels (Figure 6E). This may be explained by reduced inflammation in CXCL5$^{-/-}$ mice as a consequence of strikingly lower CXCL5 levels. These findings suggest a crucial role of host-derived CXCL5 in prostate cancer tumor progression in the bone microenvironment.

Apoptotic cells were counted inside the non-necrotic tumor sections, and no differences were found (Supplemental Figure 4B), which confirmed that AP treatment induced apoptosis in WT and CXCL5$^{-/-}$ vossicles similarly. There were no differences in mitotic cell numbers even though tumor growth was reduced. This could be due to a temporal effect, since the analysis of the tumors was performed at the experimental endpoint (2 days after AP treatment), which does not account for earlier differential effects in tumor growth.

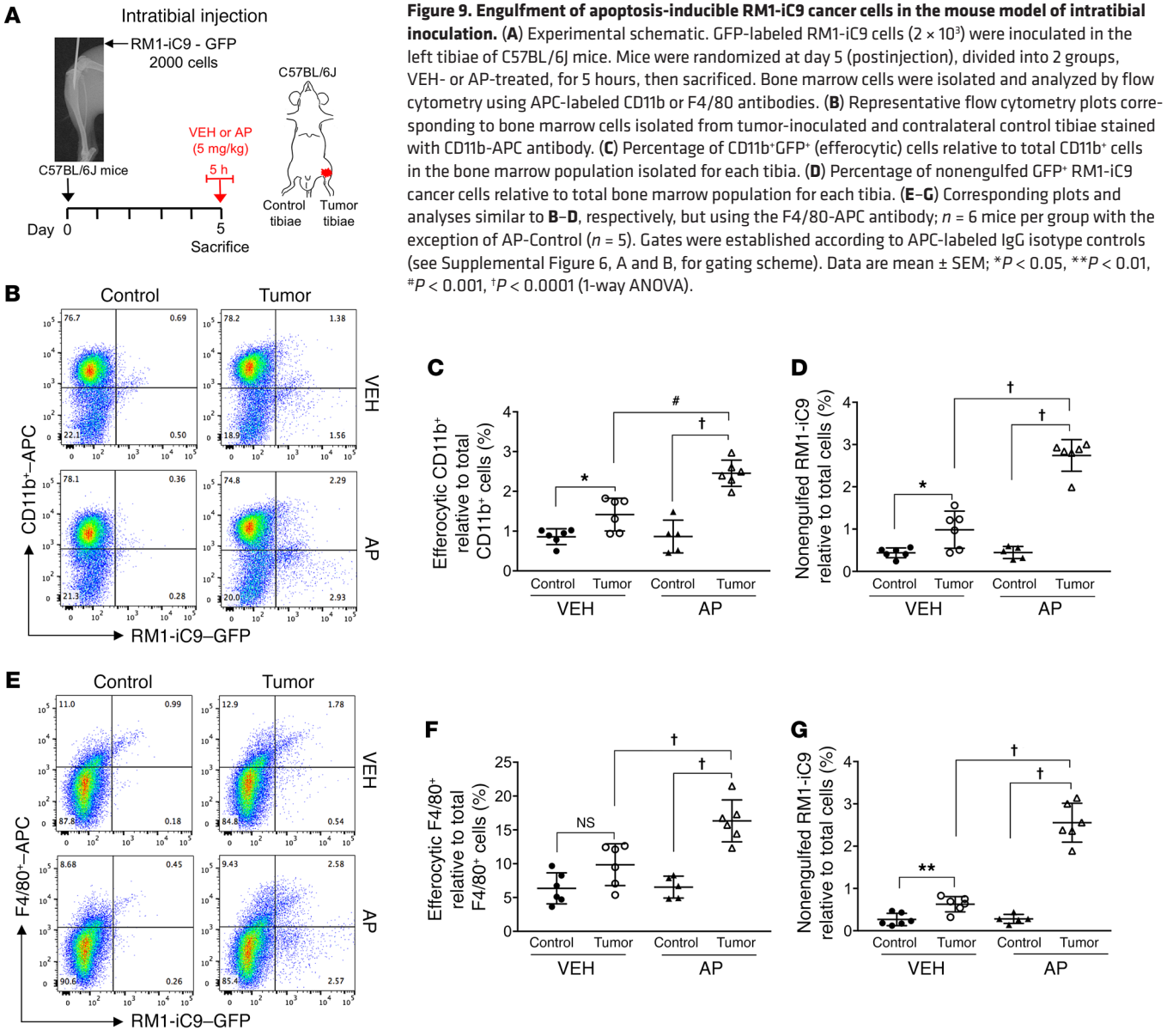

Figure 9. Engulfment of apoptosis-inducible RM1-iC9 cancer cells in the mouse model of intratibial inoculation. (**A**) Experimental schematic. GFP-labeled RM1-iC9 cells (2×10^3) were inoculated in the left tibiae of C57BL/6J mice. Mice were randomized at day 5 (postinjection), divided into 2 groups, VEH- or AP-treated, for 5 hours, then sacrificed. Bone marrow cells were isolated and analyzed by flow cytometry using APC-labeled CD11b or F4/80 antibodies. (**B**) Representative flow cytometry plots corresponding to bone marrow cells isolated from tumor-inoculated and contralateral control tibiae stained with CD11b-APC antibody. (**C**) Percentage of $CD11b^+GFP^+$ (efferocytic) cells relative to total $CD11b^+$ cells in the bone marrow population isolated for each tibia. (**D**) Percentage of nonengulfed GFP^+ RM1-iC9 cancer cells relative to total bone marrow population for each tibia. (**E**–**G**) Corresponding plots and analyses similar to **B**–**D**, respectively, but using the F4/80-APC antibody; $n = 6$ mice per group with the exception of AP-Control ($n = 5$). Gates were established according to APC-labeled IgG isotype controls (see Supplemental Figure 6, A and B, for gating scheme). Data are mean ± SEM; $^*P < 0.05$, $^{**}P < 0.01$, $^{\#}P < 0.001$, $^{\dagger}P < 0.0001$ (1-way ANOVA).

Fluorescence IHC of sections inside the tumor vossicles was performed. While areas inside the tumor vossicles were highly infiltrated by inflammatory $F4/80^+$ macrophages (red) and $Ly6B^+$ cells (green) (Figure 7A), quantitative analysis revealed that $CXCL5^{-/-}$ mice exhibited fewer $F4/80^+$ macrophages and $Ly6B^+$ inflammatory cells (Figure 7B). Figure 7C depicts the engulfing morphology observed in some macrophages when interacting with large nuclei, typical of tumor cells in comparison with the smaller nuclei of macrophages (37).

Cell analysis of tumor vossicles via flow cytometry revealed significantly reduced $F4/80^+$ macrophages, $F4/80^+CD206^+$ M2-like macrophages, and $CD11b^+Gr\text{-}1^+$ myeloid cells in $CXCL5^{-/-}$ mice (Figure 8, A–C), as well as reduced $CD11b^+Ly6B^+$ and total $Ly6B^+$ inflammatory cells (Figure 8, D and E). These results align with the IHC findings (Figure 7) and the in vitro data (Supplemental Figure 2E), in which Ly6B was increased via efferocytosis and in correlation with inflammation. Furthermore, a decrease in total $CD68^+$ phagocytic macrophages (the majority also $F4/80^+$) was observed (Figure 8F). In contrast, an increase in cells expressing the T lymphocyte–activating antigen $CD86^+$ was detected in the $CXCL5^{-/-}$ tumor vossicles (Figure 8G). Additional flow results are shown in Supplemental Figure 4C. Interestingly, the blood count of mice bearing tumor vossicles revealed significantly lower concentrations of leukocytes, lymphocytes, and monocytes in WT versus $CXCL5^{-/-}$ mice, where $CXCL5^{-/-}$ mice demonstrated values within the normal range (Supplemental Figure 4D). These findings suggest that increased recruitment of inflammatory cells into the tumors of WT mice may be responsible for a reduction of these cells in circulation, an effect that was not observed in WT mice or alleviated in $CXCL5^{-/-}$ mice.

For more in-depth analyses, flow cytometric results were compared between tumor vossicles and bone marrow myeloid cells from tumor-free WT and $CXCL5^{-/-}$ mice. In the bone marrow of the $CXCL5^{-/-}$ mice the percentages of Gr-1, Ly6B, Ly6C, Ly6G, and CD11b myeloid cells were higher than in WT mice

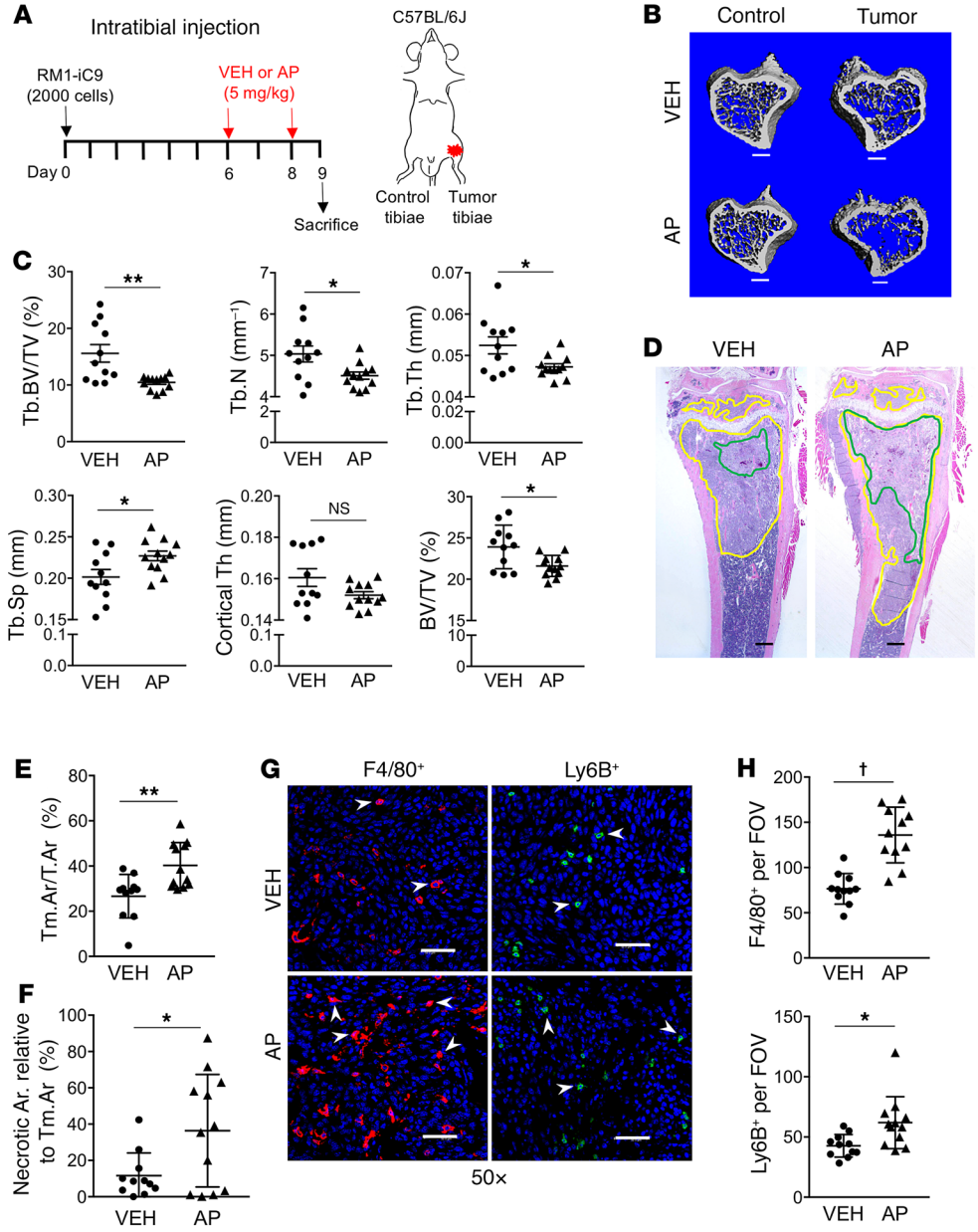

Figure 10. Cancer cell death induces accelerated tumor growth and bone osteolysis in the intratibial tumor model. (**A**) Experimental schematic. Mice injected with RM1-iC9 cells were randomized before VEH or AP treatment. (**B**) Representative μCT images showing trabecular bone in VEH and AP cancer-inoculated tibiae and the corresponding contralateral controls (nontumor) (scale bars: 400 μm). (**C**) Bone parameters quantified by μCT: trabecular bone volume relative to total volume (Tb.BV/TV), trabecular number (Tb.N), trabecular thickness (Tb.Th), trabecular spacing (Tb.Sp), cortical thickness (Cortical Th), and total bone volume relative to total volume (BV/TV); VEH (n = 11) and AP (n = 12). (**D**) Representative images of H&E sections of tumor-inoculated VEH and AP tibiae. Tumor areas are highlighted in yellow and necrosis in green (scale bars: 400 μm). (**E**) Quantification of tumor area relative to total bone area (Tm.Ar/T.Ar). (**F**) Necrotic area relative to tumor area inside the bone. (**G**) Images inside the tumor areas of sections stained using F4/80 and Ly6B antibodies for VEH and AP (×50) (scale bars: 200 μm). (**H**) Quantification of F4/80$^+$ (n = 11 per group) and Ly6B$^+$ VEH (n = 11) and AP (n = 12) staining (3 fields inside tumor area at ×20 per sample). Data are mean ± SEM; $^*P < 0.05$, $^{**}P < 0.01$, $^{\dagger}P < 0.0001$ (2-tailed Student's t test).

(Supplemental Figure 5A). These findings agree with the previously reported increase in Gr-1$^+$ cells in CXCL5$^{-/-}$ mice and the suggested role of this cytokine in bone marrow neutrophil homeostasis (38). Increased numbers of neutrophils were also found in the blood of CXCL5$^{-/-}$ mice relative to WT, but no changes in other leukocytes were observed (Supplemental Figure 5B). In contrast, the bone marrow analysis of tumor-free mice showed a significantly lower percentage of CD86$^+$ and no changes in total F4/80$^+$ cells (Supplemental Figure 5A). Since the intratumoral changes in myeloid cell populations are skewed in the opposite direction relative to tumor-free bone marrow, the differences observed in the tumor infiltration are not likely related to overall changes in the normal bone marrow of these mice; instead these changes highlight tumor environment specificity.

Altogether these findings demonstrate the critical role of the CXCL5 produced by the efferocytic macrophage as an inducer of inflammation-accelerating tumor growth in the bone microenvironment.

Cancer cell death induces accelerated tumor growth and bone destruction, while CXCL5 deficiency hinders tumor progression. Since the accelerated growth of cancer RM1-iC9 cells in the osseous vossicle model resulted in a large proportion of cells growing outside the bone, the effect of cancer cell death in tumor progression was further analyzed in an intratibial inoculation model. Engulfment of cancer cells after apoptosis induction mediated by AP treatment was evaluated. RM1-iC9 cells were GFP-labeled upon transfection with a lentiviral reporter construct prior to their inoculation into the left tibia of mice. Mice were randomized into groups treated with AP or VEH for 5 hours at day 5 after cancer inoculation (Figure 9A). Following this treatment, the bone marrow cells of the left tibia (tumor-inoculated) and the contralateral right tibia (control) were isolat-

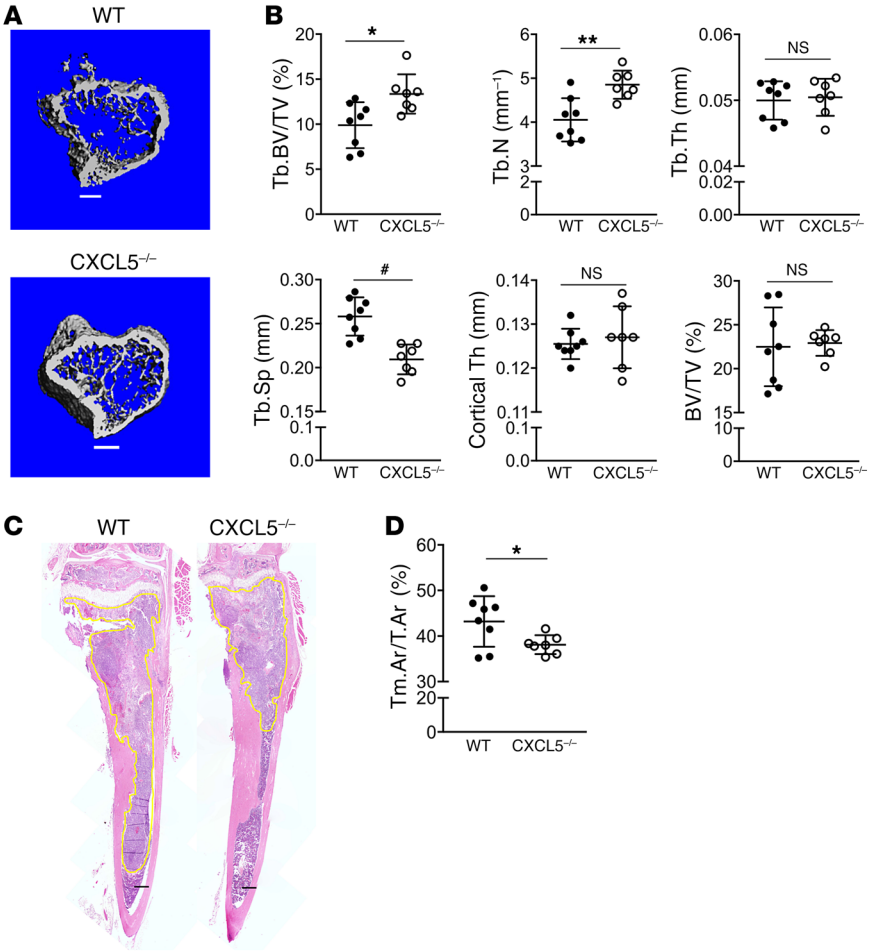

Figure 11. CXCL5 deficiency hinders tumor growth and bone osteolysis in the intratibial model. Both WT (n = 8) and CXCL5$^{-/-}$ (n = 7) mice were inoculated with RM1-iC9 cells via intratibial injection and treated with AP, similarly to Figure 10A. (**A**) Representative μCT images showing trabecular bone in the tumor tibiae for WT and CXCL5$^{-/-}$ mice (scale bars: 400 μm). (**B**) Bone parameters were quantified by μCT in tumor-injected tibiae for WT and CXCL5$^{-/-}$, similarly to Figure 10C. (**C**) Representative images of H&E sections for WT and CXCL5$^{-/-}$ tibiae. Tumors are highlighted in yellow (scale bars: 400 μm). (**D**) Quantification of tumor area relative to total bone area (Tm.Ar/T.Ar). Data are mean ± SEM; $^{*}P < 0.05$, $^{**}P < 0.01$, $^{\#}P < 0.001$ (2-tailed Student's t test).

ed and analyzed by flow cytometry using APC-labeled CD11b or F4/80 antibodies. The CD11b^{+}GFP^{+} or F4/80^{+}GFP^{+} populations in Figure 9, B and E, indicate the CD11b^{+} or F4/80^{+} efferocytic cells (engulfing cancer cells), respectively. Representative VEH and AP (tumor-inoculated) and corresponding contralateral (control) bone marrow cell plots are shown (Figure 9, B and E). APC-labeled IgG isotype control antibodies for both CD11b and F4/80 were used to determine the gates and representative plots (Supplemental Figure 6, A and B). The percentages of engulfing CD11b^{+} or F4/80^{+} cells were calculated for tumor-inoculated and control tibiae relative to total CD11b^{+} or F4/80^{+} cells, respectively. Engulfing CD11b^{+} and F4/80^{+} cells increased in the bone marrow of AP-treated tumor tibiae (AP-Tumor) relative to VEH-treated tumor (VEH-Tumor) or their controls (Figure 9, C and F). Furthermore, increased CD11b^{+} engulfing cells were observed in the VEH-Tumor relative to VEH-Control (Figure 9C), while no significant difference was found in the F4/80^{+} engulfing population (Figure 9F). No differences were found in any bone marrow population between VEH-Control and AP-Control (contralateral) tibiae (Figure 9, C and F).

The percentage of nonengulfed GFP^{+} RM1-iC9 cells was calculated relative to total cells. While higher numbers of GFP^{+} RM1-iC9 cells were observed in the bone marrow of all tumor tibiae relative to control, AP treatment significantly increased this population when compared with VEH, indicating rapid growth of cancer cells after AP treatment (Figure 9, D and G).

To further understand the effects of cancer cell apoptosis and subsequent efferocytosis on tumor progression and bone remodeling, the RM1-iC9 cells were inoculated via intratibial injection (day 0) and treated with VEH or AP at days 6 and 8 (Figure 10A). Tibiae (tumor-inoculated and control) were collected at day 9 and analyzed by micro–computed tomography (μCT). The analysis of AP-Tumor tibiae showed significant reduction in trabecular and total bone volume and reduced trabecular number and thickness with a corresponding increase in trabecular spacing relative to VEH-Tumor (Figure 10, B and C). No changes were observed in the cortical bone (Figure 10C). These results suggest that escalated bone osteolysis was induced by increased tumor growth via amplified efferocytosis and the predominant osteolytic nature of RM1 cells. However, to exclude the possibility that differences in bone volume could be due to an effect of AP in nontumor cells, μCT analysis revealed no differences in bone between VEH-Control and AP-Control contralateral tibiae (Supplemental Figure 7), confirming that the differences observed between AP and VEH in the tumor are a result of the tumor-induced osteolysis mediated by cancer cell apoptosis. Furthermore, osteoclast tartrate-resistant acid phosphatase–positive (TRAP^{+}) staining measured in bone inside the tumors (regions of interest [ROIs] depicted in Supplemental Figure 8A) demonstrated no differences in either osteoclast surface per bone surface or osteoclast number per bone surface (Supplemental Figure 8B), suggesting that the changes in trabecular and total bone volume are concomitant with osteolytic activity but not with increased osteoclast numbers.

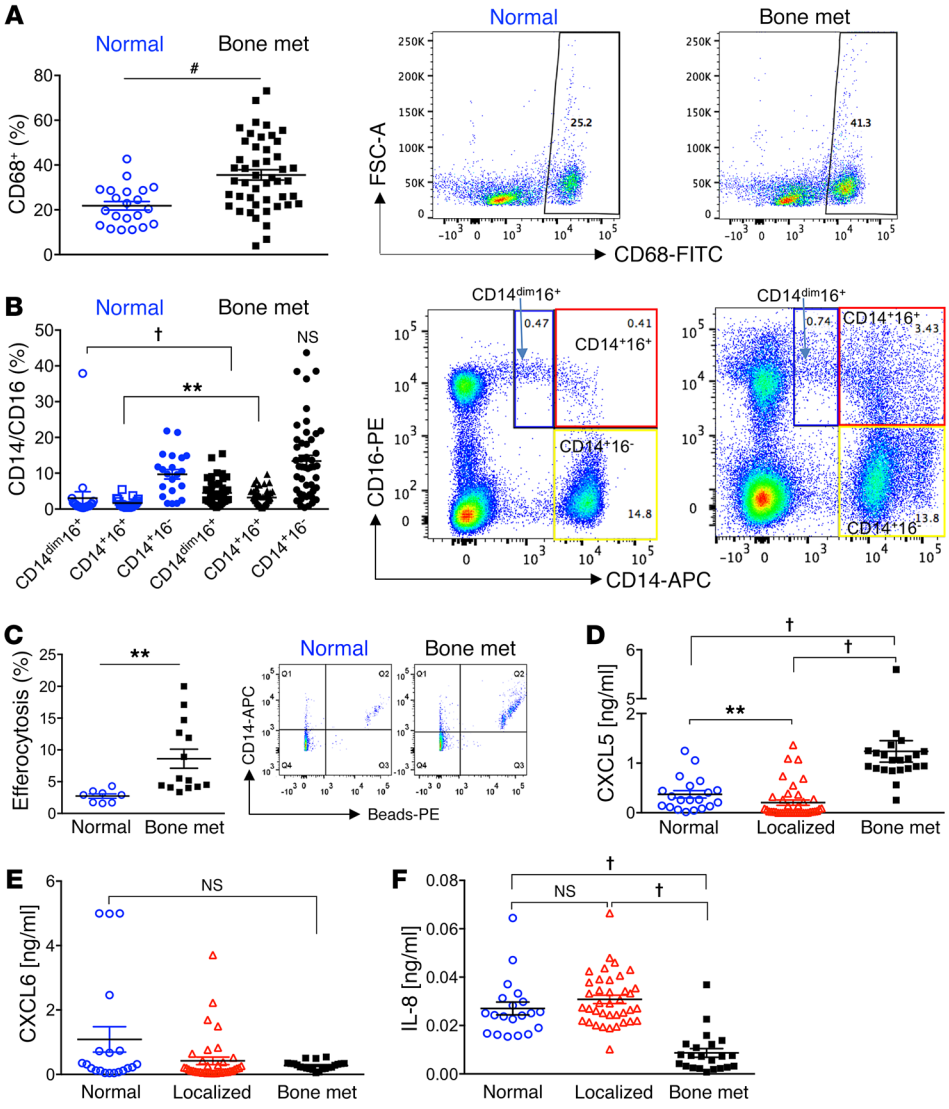

Figure 12. Nonclassical (CD16⁺) peripheral blood mononuclear cells and CXCL5 serum levels are associated with human prostate cancer skeletal metastasis. (**A**–**C**) Mononuclear cells were isolated from whole peripheral blood of noncancer (Normal, $n = 21$) and prostate cancer bone-metastatic patients (Bone met., $n = 47$). Monocyte populations were assessed via flow cytometry. (**A**) $CD68^+$ monocytes were assessed, and representative FACS images are displayed at right. (**B**) Subpopulations of $CD14^{dim}CD16^+$ (blue boxes), $CD14^+CD16^+$ (red boxes), and $CD14^+CD16^-$ (yellow boxes) were gated from total cell populations and quantified for Normal and Bone met. samples. Representative FACS plots are shown. (**C**) Freshly isolated monocytes ($CD14^+$) from normal ($n = 8$) and prostate cancer bone-metastatic ($n = 14$) patients were cultured with phosphatidylserine-coated fluorescently labeled apoptotic-mimicry beads (3:1) and efferocytosis assessed by flow cytometry for $CD14^+$ (APC^+) cells with ingested beads (representative FACS plots are shown). (**D**–**F**) Human serum isolated from normal ($n = 20$), localized (high-risk) prostate cancer (Localized, $n = 40$), and bone-metastatic prostate cancer (Bone met., $n = 22$) patients was analyzed by ELISA for CXCL5 (**D**), CXCL6 (**E**), and IL-8 (**F**). CXCL6 and IL-8 analysis included $n = 38$ for Localized. Data are mean ± SEM; $^{**}P < 0.01$, $^{\#}P < 0.001$, $^{\dagger}P < 0.0001$ (Wilcoxon 2-sample test and Kruskal-Wallis test with Bonferroni's correction).

Changes in the bones of AP-Tumor tibiae relative to the VEH-Tumor were correlated with the increased tumor progression seen in the AP-treated vossicle model. Tumor areas normalized to total bone area demonstrated that tumors were larger in AP-treated mice compared with VEH (Figure 10, D and E). The percentage of necrosis calculated as the ratio of necrotic areas divided by the total tumor area inside the bone demonstrated that increased tumor necrosis is induced by AP (Figure 10, D and F). These results suggest that the induction of apoptosis, resulting in larger tumors, also induces necrosis, perhaps enhanced by the limited capacity of macrophages to effectively clear the large proportion of apoptotic cells at an advanced stage of tumor growth. Consistent with the induction of apoptosis by AP, IHC inside the tumor revealed increased numbers of $F4/80^+$ and $Ly6B^+$ cells suggesting increased inflammation in tumors where cell death was stimulated (Figure 10, G and H).

Altogether these experiments demonstrated that induction of apoptosis with AP increased efferocytosis, rapidly stimulated cancer growth in the bone, and increased bone osteolysis.

Next, the role of CXCL5 in inducing tumor acceleration was investigated. An experiment comparing tumor growth in the bones of WT ($CXCL5^{+/+}$) and $CXCL5^{-/-}$ mice was performed. Using the same approach described above (Figure 10A), RM1-iC9 cells were inoculated via intratibial injection in 6-week-old mice. To maximize proinflammatory CXCL5 expression, WT and $CXCL5^{-/-}$ mice were treated with AP to induce cancer cell apoptosis. At endpoint, μCT analysis was performed on tumoral tibiae. CXCL5-deficient mice had significantly higher trabecular bone volumes relative to WT, increased trabecular numbers, and reduced trabecular spacing (Figure 11, A and B).

H&E-stained tumor sections showed reduced tumor areas in $CXCL5^{-/-}$ mice relative to WT (Figure 11, C and D), confirming the proinflammatory role of CXCL5 induced by efferocytosis of apoptotic cancer cells.

Nonclassical ($CD16^+$) phagocytic peripheral blood mononuclear cells and CXCL5 serum levels associated with human prostate cancer skeletal metastasis. Peripheral mononuclear cells serve as circulating immune cells in the blood recruited to replenish tissue-resident cells. A previous study reported that $CD16^+$ (nonclassical) monocytes presented a significant enrichment in genes involved in cytoskeletal arrangement and phagocytosis (39, 40). In response

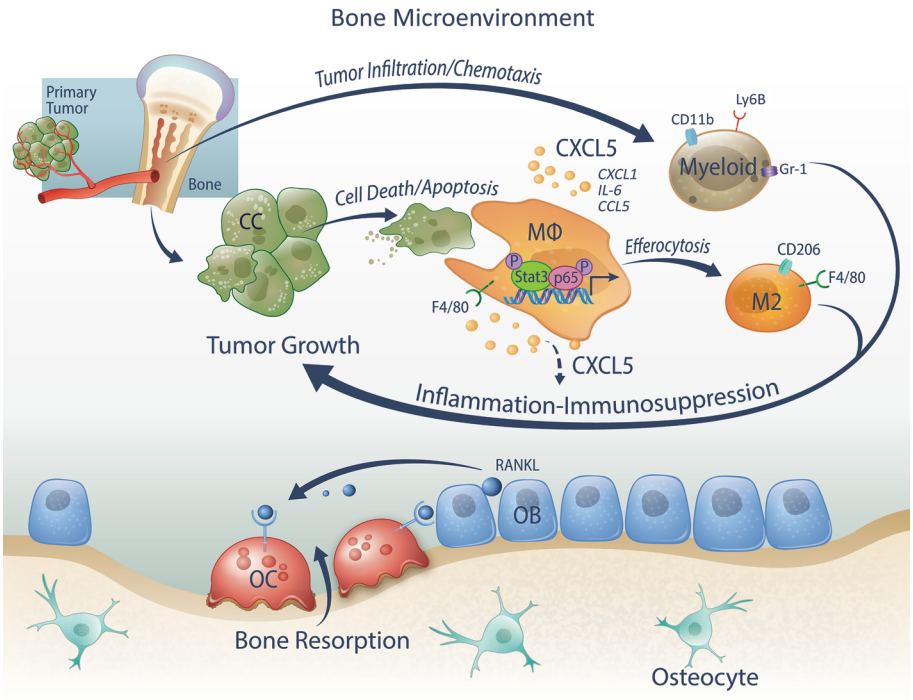

Figure 13. Model of efferocytosis-induced prostate cancer tumor growth in the bone microenvironment. Bone macrophages (MΦs) engage and efferocytose apoptotic cancer cells to induce the activation of Stat3 and NF-κB(p65), which stimulate the production of proinflammatory cytokines including CCL5, CXCL1, IL-6, and CXCL5. CXCL5 is a crucial chemoattractant of inflammatory myeloid cells, including CD11b$^+$Gr-1$^+$, Ly6B$^+$ cells, and increases M2 (F4/80$^+$CD206$^+$ cells) polarization, all resulting in perpetual inflammation and immunosuppression that stimulate tumor growth. OC, osteoclast; OB, osteoblast.

to the findings in the skeletal metastatic experimental model, we hypothesized that prostate cancer bone-metastatic patients would have increased circulating phagocytic monocytes compared with controls due to the presence of circulating tumor cells. Flow cytometric analysis of peripheral blood samples revealed that bone-metastatic patients (characteristics in Supplemental Table 1) harbored increased circulating CD68$^+$ (a phagocytic marker) cells compared with healthy controls (Figure 12A). These patients also had increased mononuclear CD14$^+$CD16$^+$ and CD14^{dim}CD16$^+$ cells (a patrolling monocyte subset) (ref. 41 and Figure 12B). Both of these populations express CD68 (Supplemental Figure 9A). However, no significant differences were identified in the classical CD14$^+$CD16$^-$ mononuclear population. The average age in male control (noncancer) patients was lower than in the bone-metastatic patients (Supplemental Figure 9B), but no significant correlation was found inside each group between the ages and the percentages of the different populations: CD68$^+$, CD14^{dim}CD16$^+$, CD14$^+$CD16$^+$, and CD14$^+$CD16$^-$ (Supplemental Figure 9C). Other studies have suggested that monocytes expressing both CD14 and CD16 are elevated in patients with cancer (42). To investigate the efferocytic capabilities of freshly isolated mononuclear cells from prostate cancer bone-metastatic patients compared with control, cells were cultured with phosphatidylserine-coated apoptotic-mimicry beads. Monocytes (CD14$^+$) isolated from patients with prostate cancer skeletal metastases had significantly greater efferocytosis (double-positive for beads and CD14) compared with cells from normal (noncancer) patients (Figure 12C).

Consistent with these results, we hypothesized that phagocytic monocytes/macrophages would increase serum levels of the inflammatory CXCL5 cytokine in bone metastasis patients because of tumor cell clearance both in circulation and in the bone marrow compartment. A cohort of serum samples from patients with progressive advanced castration-resistant prostate cancer metastatic to bone with multiple lesions (≥3 lesions), with no prior chemotherapy for metastatic disease and no signs of ongoing infection or another malignant disease, was analyzed (Supplemental Table 2). These samples were compared with cohorts of patients with either localized high-risk prostate cancer or noncancer patients. The age distribution from each group is shown in Supplemental Figure 10A. All samples were analyzed by ELISA to measure 3 closely related cytokines: CXCL5, CXCL6 (a human cytokine homologous to mouse CXCL5), and IL-8 (CXCL8). Human IL-8 is a proinflammatory cytokine with no direct murine homolog, suggested to be functionally homologous with murine CXCL1, CXCL5, and CXCL6 (43). Intriguingly, normal samples displayed significantly higher serum CXCL5 relative to localized cancer samples (Figure 12D). Importantly, considerably higher levels of CXCL5 were detected in the serum of bone-metastatic patients compared with other groups, while no significant differences were observed for CXCL6 (Figure 12E). Contrary to the CXCL5 results, serum samples from bone-metastatic patients showed significantly reduced IL-8 concentrations relative to normal and localized samples (Figure 12F). Furthermore, no significant correlation was found between the CXCL5 or IL-8 serum concentrations and the age of patients for each group, respectively (Supplemental Figure 10B). Altogether these findings suggest the predominant role of proinflammatory CXCL5 in prostate cancer bone metastasis in concert with the increased phagocytic circulating CD68$^+$CD14$^+$CD16$^+$ monocytic cell population.

Discussion

Persistent inflammation in the tumor microenvironment is a common denominator of cancer progression characterized by the infiltration of myeloid cells that facilitate tumor expansion and metastasis (44). Chronic inflammation increases cell stress and tissue damage, which induces apoptotic/necrotic cell death. Conse-

quently, several aggressive tumors are characterized by high apoptotic rates, which are often underestimated as a result of efficiency of clearance (efferocytosis) (11). Efferocytosis is a fundamental function of professional phagocytes (mainly macrophages) and an essential mechanism of normal tissue homeostasis that also prevents inflammation. However, here we present new evidence suggesting that the response of bone marrow macrophages when engaged in efferocytosis of prostate cancer cells differs from the response when engaged with cells that bone marrow macrophages would normally encounter, such as osteoblasts and stromal cells.

Cancer cell efferocytosis was found to induce an inflammatory response in macrophages characterized by the expression of CCL5, CXCL1, CXCL5, and IL-6, which have been correlated with tumor inflammation mechanisms and metastasis in several cancer types (45, 46). Accordingly, these findings suggest that the induction of efferocytosis leads to activation of NF-κB(p65) and Stat3 signaling and proinflammatory cytokine expression. Blocking NF-κB(p65) or Stat3 signaling mitigated the expression of inflammatory cytokines in macrophages, while simultaneous inactivation of these pathways blocked the efferocytic function of macrophages. Since neither Stattic nor Bay11-7082 inhibited efferocytosis when used alone, these findings further suggest that these two pathways are not only activated by efferocytosis, but are critical components of this mechanism, where at least one has to be fully active for this essential function of macrophages. In accordance, NF-κB(p65) and Stat3 are steadily activated in immune cells, where they selectively regulate each other to trigger amplification loops that stimulate the production of protumor inflammatory factors (7, 24, 25). It has been suggested that continuous activation of Stat3 is a prerequisite for these tumor-promoting immune responses (47). Furthermore, activation of Stat3 by efferocytosis mediates the M2-like polarization of bone marrow macrophages (12). In vivo studies in breast and colon cancer showed that efferocytosis induced M2 polarization and metastasis, while increased cell death correlated with poorer outcomes (13, 48). Moreover, the proinflammatory cytokine IL-6 induced M2-like macrophage polarization in human macrophages (49). Our findings suggest that efferocytosis induces tumor-promoting inflammation mediated by the persistent activation of Stat3 and NF-κB(p65) in macrophages.

The bone marrow is a myeloid-rich microenvironment for seeding and colonization of metastatic cells. Using apoptosis-inducible murine RM1 prostate cancer cells and bone vossicles as a syngeneic model of osseous environmental tumor growth, it was demonstrated that induced cancer death accelerated tumor progression. RM1 cells were chosen in this study as these cells are derived from prostate epithelium of C57BL/6J mice and overexpress the Ras and Myc oncogenes, which resembles the oncogene-specific gene expression signatures of prostate cancer patient samples and is associated with prostate cancer progression (50, 51). The vossicle model provides an osseous scaffold for tumor growth where cancer cells are implanted directly in the interacting bone niche. This interaction between tumor and bone is critical, especially at the early stages of tumor growth. The importance of bone in the vossicle serving as scaffold was demonstrated in previous experiments in which tumor growth was accelerated in the vossicles isolated from a *Gas6*$^{-/-}$ mouse relative to controls after implantation in the same host. In these experiments tumor growth was assessed in vossicles where tumors overgrew the bone scaffolds (31). Another example of the vossicle model highlighting the bone microenvironment in tumor progression revealed that ablation of the osteoblast niche hindered prostate cancer growth in tumor vossicles (17). Furthermore, it was recently reported that macrophage ablation decelerated tumor growth using the RM1/vossicle model (9).

Elevated numbers of apoptotic cells were observed in the tumor vossicles where apoptosis was induced, and cell death induced a higher percentage of F4/80$^+$CD206$^+$ (M2-like) macrophages in tumors, which correlates with increased polarization induced by efferocytosis (12). Furthermore, CD11b$^+$Gr-1$^+$ cells, expressing markers of myeloid-derived suppressor cells (MDSCs), were also increased in tumors where cell death was induced. Although overlapping values of different immune cell populations were detected by flow cytometry between VEH- and AP-treated groups, this could be explained by the significant level of apoptosis found in RM1-iC9 control tumors and/or the possibility that AP treatment did not equally reach all cancer cells because of the complexity of large tumors. For similar reasons, a high variability in the CXCL5 concentrations was detected in the tumors linked to the various levels of apoptosis, which would overlap in some cases with controls. While we cannot exclude the important role of other proinflammatory cytokines, the critical role of CXCL5 is further supported by the significant correlation found between CXCL5 levels and tumor weight.

Other studies have identified CXCL5 as a predictor for bone-metastatic prostate cancer (52), and in a breast cancer metastatic model it was shown that this cytokine is a factor secreted by tumor-associated osteoblasts to function as an inducer of epithelial-to-mesenchymal transition and metastasis (53). Furthermore, in a model of rhabdomyosarcoma, it was demonstrated that antibody-mediated neutralization of CXCR2 (a receptor for CXCL5) enhanced anti-PD1 effectiveness by preventing the tumor infiltration of the CD11b$^+$Ly6G^{hi} suppressor cells (54). However, none of these works identified the proinflammatory efferocytic macrophage as a trigger of tumor growth in the bone microenvironment.

Using the CXCL5$^{-/-}$ mice in a syngeneic tumor vossicle model delineated the crucial role of host-derived CXCL5 in the mechanism of cell death–induced tumor progression. CXCL5 deficiency significantly inhibited tumor progression in bone vossicles. Although the cytokine array might have missed other cytokines represented at lower concentrations, CXCL5 was expressed at considerable levels, and the major contribution was from the host microenvironment and not the cancer cells. Intriguingly, ELISA analysis showed reduced levels of CXCL1 in CXCL5$^{-/-}$ vossicles versus WT. Although CXCL1, a cytokine that interacts with the same receptor (CXCR2) as CXCL5, was expressed at lower levels in the tumor in comparison with CXCL5, these results are consistent with reduced cell death–induced inflammation mediated by CXCL5 deficiency in the vossicles.

Analysis of CXCL5$^{-/-}$ tumor vossicles revealed reduced percentages of M2-like (F4/80$^+$CD206$^+$) and phagocytic (CD68$^+$F4/80$^+$) macrophages as well as inflammatory Ly6B$^+$ cells and granulocytic CD11b$^+$Gr-1$^+$ cells that characterize MDSCs, all of which aligns with reduced inflammation and efferocytosis and the role of CXCL5 as a crucial chemoattractant of MDSCs. Importantly, and in contrast, increased influx of CD86$^+$ cells was identified within CXCL5$^{-/-}$

tumors as compared with WT. Recent findings using a mouse model of lung carcinoma demonstrated the role of CD86$^+$ myeloid cells in the tumor microenvironment as mediators of the antitumoral effects of carbon monoxide treatment (55), where depletion of CD86$^+$ cells with neutralizing antibody accelerated tumor growth. These results suggest that the reduced tumor progression shown in CXCL5$^{-/-}$ mice is at least partially due to increased CD86$^+$ cells with antitumor activity.

Flow cytometry and IHC results included overlapping values within the F4/80, Ly6B, and CD86 populations between WT and CXCL5$^{-/-}$ mice, suggesting that other proinflammatory cytokines may play a role and partially compensate for the CXCL5 deficiency to support tumor growth. Nevertheless, the osseous vossicle model presented valuable information about the changes in immune cell populations infiltrating the tumors associated with the activation of apoptosis and efferocytosis and in correlation with tumor progression.

Mixed osteoblastic and osteolytic lesions occur in patients with metastatic prostate cancer, all characterized by aberrant bone remodeling where osteoblastic bone formation and signaling are linked to osteolytic bone resorption (56). Previous findings using RM1 cells showed that macrophage depletion decelerated tumor growth but had differential effects on bone, dependent on mode of depletion, suggesting that in bone metastasis, macrophages may be more important for tumor progression than their effects in the bone (9). In the present study with RM1-iC9 cancer cells, the apoptosis inducer AP increased apoptotic cell engulfment, which was accompanied by accelerated growth of cancer cells. This rapid in vivo increase in cancer cells after AP treatment was not observed in vitro in cocultures of macrophages and RM1-iC9 cells (no change in nonengulfed cancer cells relative to VEH controls) (Supplemental Figure 6C). This result could be associated with the activation of inflammation-mediated immunosuppression within the bone microenvironment, allowing cancer cells to grow faster in a debilitated immune environment.

The accelerated tumor progression in the bone reported here resulted in increased osteolysis, necrotic cell death, and inflammation as detected by increased F4/80$^+$ and Ly6B$^+$ cell infiltration. Previous in vivo studies in prostate cancer models suggest that activation of CD11b$^+$Gr-1$^+$ cells in the bone marrow was mediated by IL-6 to accelerate tumor progression (34, 35). These findings suggest that increased bone marrow macrophage infiltration into the tumors results in CXCL5 and other proinflammatory cytokines that facilitate recruitment and activation of CD11b$^+$Gr-1$^+$, which enhances immunosuppression and tumor growth. Similarly, AP-treated tumors in CXCL5-deficient mice resulted in decelerated tumor progression and osteolysis, supporting the critical role of this cytokine; however, the overlap variability detected in some tumor areas and bone volumes suggests a potential role of other efferocytosis-induced proinflammatory cytokines in tumor progression. Furthermore, because osteolytic bone destruction was predominantly found in the in vivo models used in these studies, these findings may not be fully applicable to the osteoblastic lesions observed in human skeletal metastases.

CD14$^+$CD16$^+$ monocytes account for only 8% of all monocytes and exhibit a higher rate of phagocytosis, which is associated with acute and chronic inflammation (57). In metastatic gastrointestinal carcinoma, patients exhibited a significant elevation in a unique CD16$^+$ blood-monocyte population, which did not correlate with sepsis or bacterial infection (58). The presence of this monocyte subset predicted tissue invasiveness of cholangiocarcinoma and was elevated in patients with solid tumors. In the present study we analyzed phagocytic circulating blood monocytes (CD68$^+$) that were either classical (CD14$^+$CD16$^-$), nonclassical (CD14$^+$CD16$^+$), or patrolling (CD14^{dim}CD16$^+$) in patients with prostate cancer bone metastasis and noncancerous control patients. While no difference was found in total CD14$^+$CD16$^-$ monocytes relative to normal (noncancer controls), a significant increase was identified in the CD14$^+$CD16$^+$ and the CD14^{dim}CD16$^+$ (low CD14) monocytes in bone-metastatic patients with overlap in populations observed compared with normal controls, which may be related to the bone-metastatic disease being at different stages of progression. It is likely that at early stages of metastatic disease these values may be closer to normal, while more advanced metastatic disease would exhibit the highest increase in these cell populations. Although the CD14^{dim}CD16$^+$ monocytes have been shown to respond poorly to bacterial signals, they also express high levels of selected inflammatory cytokines in response to viruses via TLR7 and TLR8 (41). Studies on human monocytes indicated that CD14$^+$CD16$^+$ cells play an important role in inflammatory diseases such as rheumatoid arthritis (42), and a recent report suggests that these nonclassical monocytes display inflammatory features (59), which correlates with our findings showing increased CD68$^+$CD14$^+$CD16$^+$ nonclassical phagocytic monocytes and proinflammatory CXCL5 in blood serum of bone-metastatic compared with normal (noncancer) patients. Our results further suggest an important role of both CD14^{dim}CD16$^+$ and CD14$^+$CD16$^+$ monocytes in metastasis-promoting inflammatory responses.

In mice, CXCL5 exhibits a predominant role in the neutrophil influx to the lung as a result of inflammation induced by LPS inhalation, which aligns with its role in human inflammatory diseases as a neutrophil chemoattractant (38). The expression of CXCL6, a human homolog of mouse CXCL5 (60), was significantly upregulated in prostate cancer tissues and correlated with high Gleason scores (≥7) (61). However, analysis of blood serum from prostate cancer bone-metastatic patients revealed differences in CXCL5 when comparing with normal or high-risk localized cancer, while no significant differences were observed for CXCL6. Recently it has been proposed that murine CXCL5 is the functional homolog of human IL-8 (62); however, contrary to the findings with human CXCL5, the analysis of IL-8 serum levels in the same patient cohort showed higher IL-8 expression in the serum of noncancer and localized cancer relative to the bone-metastatic group. Further analysis with human macrophages will provide clues and help clarify the production of such cytokines induced by efferocytosis.

In summary, these findings reveal a new mechanism by which the clearance of dying tumor cells by macrophages induces persistent inflammation in the tumor bone microenvironment via expression of CXCL5 and other proinflammatory cytokines to facilitate cancer progression (Figure 13). Since enhanced cell death and efferocytosis are produced by cancer therapies, the identification of CXCL5 as a crucial factor in this mechanism provides an important clue for designing additional successful therapies.

Methods

Cell lines and animals. Murine prostate cancer RM1 cells were originally a gift from Timothy C. Thompson (Baylor College of Medicine, Houston, Texas, USA) (63, 64). Apoptosis-inducible RM1-iC9 cells were developed by transduction of murine RM1 with the viral construct for inducible caspase-9 (iC9) as previously described (23). The newly constructed RM1-iC9 cells were characterized by an independent laboratory (IDEXX BioResearch), which confirmed origination from the C57BL/6J mouse strain, the same profile as the parent RM1, and no contamination was detected. PC3 cells (also tested by IDEXX BioResearch) were obtained from the American Type Culture Collection (ATCC). MC3T3-E1 subclone 4 (MC4) cells (ATCC CRL2593) were provided by Renny T. Franceschi (University of Michigan). C57BL/6J mouse primary prostate epithelial cells (MPECs) were obtained from Cell Biologics (C57-6038).

All animal experiments were performed with approval from the University of Michigan Institutional Animal Care and Use Committee. Control WT mice (C57BL/6J) were purchased from the Jackson Laboratory. CXCL5$^{-/-}$ knockout mice on a C57BL/6J background were donated by George Scott Worthen and Junjie Mei (Division of Neonatology, Children's Hospital of Philadelphia, University of Pennsylvania, Philadelphia, Pennsylvania, USA) (38).

Vossicle (vertebral body) subcutaneous RM1-iC9 tumors. The vossicle model, which provides an osseous scaffold for tumor growth in a bone microenvironment, has been previously described (9, 31). Detailed description is provided in Supplemental Methods.

Intratibial injection model. Apoptosis-inducible RM1-iC9 murine prostate cancer cells (2×10^3) or RM1-iC9–GFP (RM1-iC9 cells transduced with GFP-reporter lentiviral construct; Lenti-GFP, University of Michigan Vector Core) were injected in the left tibiae of C57BL/6J mice under anesthesia as previously described (9). Detailed description is provided in Supplemental Methods.

Human mononuclear cell isolation. Human peripheral blood mononuclear cells were isolated from 7.5 ml of venous blood collected in EDTA-coated vacutainer tubes (Becton Dickinson). Samples were collected at the University of Michigan Comprehensive Cancer Center from patients with prostate cancer bone metastases as well as from healthy donors without any cancer history. Complete description is provided in Supplemental Methods.

Statistics. Statistical analyses were performed in GraphPad Prism 6 (GraphPad Software Inc.) using unpaired 2-tailed Student's *t* test to compare differences between 2 groups with significance of *P* less than 0.05. One-way ANOVA with multiple-comparisons tests was used to compare 3 or more groups with significance of *P* less than 0.05. The in vivo tumor progression was analyzed using 2-way ANOVA with multiple comparisons. Human peripheral blood mononuclear cell populations and human ELISA data were analyzed using nonparametric rank tests; 2-group comparisons were tested with a Wilcoxon rank test, and when more than 2 groups were tested the Kruskal-Wallis rank test was used at significance of *P* less than 0.0083 (using the Bonferroni multiple-comparisons adjustment).

TRACER data from multiple experimental repeats were combined. Measurements were $\log_2$-transformed and normalized to the average intensity of the control reporter, which contained only the minimal TATA-box promoter. The data were further normalized to background, defined as cells transfected with reporter virus but not administered apoptotic cells. Finally, data were normalized to the initial reporter measurement for each treatment condition at 0 hours. Statistical significance among background and experimental groups was determined using the R package limma (65). To generate heatmaps, the $\log_2$ fold change for each condition and time point was averaged among replicates. Reporters were grouped into 4 clusters using *k*-means clustering.

Study approval. All participating patients were enrolled in our prospective study (HUM0052405), which was approved by the University of Michigan Medical School Institutional Review Board (Ann Arbor, Michigan, USA). All patients provided their written informed consent prior to their participation in the study.

Additional methods and extended descriptions are provided in Supplemental Methods.

Author contributions

HR, JDJ, and LKM conceived and designed the study. YW, KJP, TMM, and ETK provided human samples, and JEN provided the apoptosis-inducible construct and expertise. HR, MCP, JDJ, SW, AJK, and RK performed experiments. HR, JDJ, MCP, SW, AJK, RK, LDS, and LKM contributed to experimental design and data analysis. JEW contributed to tissue data analysis, images and expertise. SDN performed statistical analysis. MCP, SW, and HR created figures. HR, LKM, AJK, JDJ, MCP, SW, RK, and LDS contributed to manuscript writing. All authors revised and edited the manuscript.

Acknowledgments

We are indebted to George Scott Worthen and Junjie Mei for providing CXCL5$^{-/-}$ mice. We thank Fabiana Soki, Megan Michalski, and Benjamin Sinder for technical assistance, and thoughtful discussions. We also thank Sasha Meshinchi for confocal microscopy assistance (University of Michigan Microscopy Facility), David Adams for assistance with Amnis Imaging flow cytometer, Michelle Lynch for μCT assistance, and Chris Strayhorn and Theresa Cody for histology sectioning. We are very grateful to Victoria Zakrzewski, Kenneth Rieger, and Serk In Park for artistic contributions. This work was supported by NIH awards P01-CA093900 to LKM, KJP, and ETK, R01-CA173745 to LDS, R01-DK053904 to LKM, R01-DE21139 and R01-DE23220 to JEN, and R01GM093183 to LDS; and Department of Defense awards W81XWH-14-1-0408 to JDJ, W81XWH-14-1-0287 to TMM, and Prostate Cancer Foundation (PCF) Young Investigator Award to TMM.

Address correspondence to: Laurie K. McCauley, University of Michigan, School of Dentistry, 1101 N. University Avenue, Ann Arbor, Michigan 48109-1078, USA. Phone: 734.763.3311; E-mail: mccauley@umich.edu.

1. Weilbaecher KN, Guise TA, McCauley LK. Cancer to bone: a fatal attraction. *Nat Rev Cancer*. 2011;11(6):411–425.
2. Roodman GD. Mechanisms of bone metastasis. *N Engl J Med*. 2004;350(16):1655–1664.
3. Mantovani A. La mala educación of tumor-associated macrophages: diverse pathways and new players. *Cancer Cell*. 2010;17(2):111–112.
4. Mantovani A, Allavena P, Sica A, Balkwill F. Cancer-related inflammation. *Nature*. 2008;454(7203):436–444.
5. Lu X, et al. VCAM-1 promotes osteolytic expansion of indolent bone micrometastasis of breast cancer by engaging α4β1-positive osteoclast progenitors. *Cancer Cell*. 2011;20(6):701–714.

6. Chen Q, Zhang XH, Massagué J. Macrophage binding to receptor VCAM-1 transmits survival signals in breast cancer cells that invade the lungs. *Cancer Cell*. 2011;20(4):538–549.
7. Roca H, McCauley LK. Inflammation and skeletal metastasis. *Bonekey Rep*. 2015;4:706.
8. Germano G, Mantovani A, Allavena P. Targeting of the innate immunity/inflammation as complementary anti-tumor therapies. *Ann Med*. 2011;43(8):581–593.
9. Soki FN, et al. Bone marrow macrophages support prostate cancer growth in bone. *Oncotarget*. 2015;6(34):35782–35796.
10. Mills CD, Lenz LL, Harris RA. A breakthrough: macrophage-directed cancer immunotherapy. *Cancer Res*. 2016;76(3):513–516.
11. Gregory CD, Pound JD. Cell death in the neighbourhood: direct microenvironmental effects of apoptosis in normal and neoplastic tissues. *J Pathol*. 2011;223(2):177–194.
12. Soki FN, et al. Polarization of prostate cancer-associated macrophages is induced by milk fat globule-EGF factor 8 (MFG-E8)-mediated efferocytosis. *J Biol Chem*. 2014;289(35):24560–24572.
13. Stanford JC, et al. Efferocytosis produces a prometastatic landscape during postpartum mammary gland involution. *J Clin Invest*. 2014;124(11):4737–4752.
14. Michalski MN, Koh AJ, Weidner S, Roca H, McCauley LK. Modulation of osteoblastic cell efferocytosis by bone marrow macrophages. *J Cell Biochem*. 2016;117(12):2697–2706.
15. McCabe NP, Madajka M, Vasanji A, Byzova TV. Intraosseous injection of RM1 murine prostate cancer cells promotes rapid osteolysis and periosteal bone deposition. *Clin Exp Metastasis*. 2008;25(5):581–590.
16. Kaighn ME, Narayan KS, Ohnuki Y, Lechner JF, Jones LW. Establishment and characterization of a human prostatic carcinoma cell line (PC-3). *Invest Urol*. 1979;17(1):16–23.
17. Shiozawa Y, et al. Human prostate cancer metastases target the hematopoietic stem cell niche to establish footholds in mouse bone marrow. *J Clin Invest*. 2011;121(4):1298–1312.
18. Acharyya S, et al. A CXCL1 paracrine network links cancer chemoresistance and metastasis. *Cell*. 2012;150(1):165–178.
19. Erez N, Truitt M, Olson P, Arron ST, Hanahan D. Cancer-associated fibroblasts are activated in incipient neoplasia to orchestrate tumor-promoting inflammation in an NF-κB-dependent manner. *Cancer Cell*. 2010;17(2):135–147.
20. Weiss MS, et al. Dynamic transcription factor activity and networks during ErbB2 breast oncogenesis and targeted therapy. *Integr Biol (Camb)*. 2014;6(12):1170–1182.
21. Iwanaszko M, Kimmel M. NF-κB and IRF pathways: cross-regulation on target genes promoter level. *BMC Genomics*. 2015;16:307.
22. Moschonas A, Ioannou M, Eliopoulos AG. CD40 stimulates a "feed-forward" NF-κB-driven molecular pathway that regulates IFN-β expression in carcinoma cells. *J Immunol*. 2012;188(11):5521–5527.
23. Nör JE, Hu Y, Song W, Spencer DM, Núñez G. Ablation of microvessels in vivo upon dimerization of iCaspase-9. *Gene Ther*. 2002;9(7):444–451.
24. Yu H, Lee H, Herrmann A, Buettner R, Jove R. Revisiting STAT3 signalling in cancer: new and unexpected biological functions. *Nat Rev Cancer*. 2014;14(11):736–746.
25. Yu H, Pardoll D, Jove R. STATs in cancer inflammation and immunity: a leading role for STAT3. *Nat Rev Cancer*. 2009;9(11):798–809.
26. Schust J, Sperl B, Hollis A, Mayer TU, Berg T. Stattic: a small-molecule inhibitor of STAT3 activation and dimerization. *Chem Biol*. 2006;13(11):1235–1242.
27. Jeong JH, Park SJ, Dickinson SI, Luo JL. A constitutive intrinsic inflammatory signaling circuit composed of miR-196b, Meis2, PPP3CC, and p65 drives prostate cancer castration resistance. *Mol Cell*. 2017;65(1):154–167.
28. Pierce JW, et al. Novel inhibitors of cytokine-induced IkappaBalpha phosphorylation and endothelial cell adhesion molecule expression show anti-inflammatory effects in vivo. *J Biol Chem*. 1997;272(34):21096–21103.
29. Miller SC, et al. Identification of known drugs that act as inhibitors of NF-κB signaling and their mechanism of action. *Biochem Pharmacol*. 2010;79(9):1272–1280.
30. Davies LC, et al. Distinct bone marrow-derived and tissue-resident macrophage lineages proliferate at key stages during inflammation. *Nat Commun*. 2013;4:1886.
31. Jung Y, et al. Prevalence of prostate cancer metastases after intravenous inoculation provides clues into the molecular basis of dormancy in the bone marrow microenvironment. *Neoplasia*. 2012;14(5):429–439.
32. Begley LA, et al. CXCL5 promotes prostate cancer progression. *Neoplasia*. 2008;10(3):244–254.
33. Biswas SK, Mantovani A. Macrophage plasticity and interaction with lymphocyte subsets: cancer as a paradigm. *Nat Immunol*. 2010;11(10):889–896.
34. Yang L, et al. Expansion of myeloid immune suppressor Gr^+CD11b^+ cells in tumor-bearing host directly promotes tumor angiogenesis. *Cancer Cell*. 2004;6(4):409–421.
35. Park SI, et al. Parathyroid hormone-related protein drives a $CD11b^+Gr1^+$ cell-mediated positive feedback loop to support prostate cancer growth. *Cancer Res*. 2013;73(22):6574–6583.
36. Geissmann F, Jung S, Littman DR. Blood monocytes consist of two principal subsets with distinct migratory properties. *Immunity*. 2003;19(1):71–82.
37. Caillou B, et al. Tumor-associated macrophages (TAMs) form an interconnected cellular supportive network in anaplastic thyroid carcinoma. *PLoS One*. 2011;6(7):e22567.
38. Mei J, et al. CXCL5 regulates chemokine scavenging and pulmonary host defense to bacterial infection. *Immunity*. 2010;33(1):106–117.
39. Wong KL, et al. Gene expression profiling reveals the defining features of the classical, intermediate, and nonclassical human monocyte subsets. *Blood*. 2011;118(5):e16–e31.
40. Frankenberger M, et al. Transcript profiling of CD16-positive monocytes reveals a unique molecular fingerprint. *Eur J Immunol*. 2012;42(4):957–974.
41. Cros J, et al. Human CD14dim monocytes patrol and sense nucleic acids and viruses via TLR7 and TLR8 receptors. *Immunity*. 2010;33(3):375–386.
42. van de Veerdonk FL, Netea MG. Diversity: a hallmark of monocyte society. *Immunity*. 2010;33(3):289–291.
43. Hol J, Wilhelmsen L, Haraldsen G. The murine IL-8 homologues KC, MIP-2, and LIX are found in endothelial cytoplasmic granules but not in Weibel-Palade bodies. *J Leukoc Biol*. 2010;87(3):501–508.
44. Hiratsuka S, Watanabe A, Aburatani H, Maru Y. Tumour-mediated upregulation of chemoattractants and recruitment of myeloid cells predetermines lung metastasis. *Nat Cell Biol*. 2006;8(12):1369–1375.
45. Sottnik JL, Dai J, Zhang H, Campbell B, Keller ET. Tumor-induced pressure in the bone microenvironment causes osteocytes to promote the growth of prostate cancer bone metastases. *Cancer Res*. 2015;75(11):2151–2158.
46. Rutkowski MR, et al. Microbially driven TLR5-dependent signaling governs distal malignant progression through tumor-promoting inflammation. *Cancer Cell*. 2015;27(1):27–40.
47. Lee H, Deng J, Xin H, Liu Y, Pardoll D, Yu H. A requirement of STAT3 DNA binding precludes Th-1 immunostimulatory gene expression by NF-κB in tumors. *Cancer Res*. 2011;71(11):3772–3780.
48. Yang M, Liu J, Piao C, Shao J, Du J. ICAM-1 suppresses tumor metastasis by inhibiting macrophage M2 polarization through blockade of efferocytosis. *Cell Death Dis*. 2015;6:e1780.
49. Roca H, Varsos ZS, Sud S, Craig MJ, Ying C, Pienta KJ. CCL2 and interleukin-6 promote survival of human $CD11b^+$ peripheral blood mononuclear cells and induce M2-type macrophage polarization. *J Biol Chem*. 2009;284(49):34342–34354.
50. Ju X, et al. Novel oncogene-induced metastatic prostate cancer cell lines define human prostate cancer progression signatures. *Cancer Res*. 2013;73(2):978–989.
51. Koh CM, Bieberich CJ, Dang CV, Nelson WG, Yegnasubramanian S, De Marzo AM. MYC and prostate cancer. *Genes Cancer*. 2010;1(6):617–628.
52. Sung SY, et al. Coevolution of prostate cancer and bone stroma in three-dimensional coculture: implications for cancer growth and metastasis. *Cancer Res*. 2008;68(23):9996–10003.
53. Hsu YL, Hou MF, Kuo PL, Huang YF, Tsai EM. Breast tumor-associated osteoblast-derived CXCL5 increases cancer progression by ERK/MSK1/Elk-1/snail signaling pathway. *Oncogene*. 2013;32(37):4436–4447.
54. Highfill SL, et al. Disruption of CXCR2-mediated MDSC tumor trafficking enhances anti-PD1 efficacy. *Sci Transl Med*. 2014;6(237):237ra67.
55. Nemeth Z, et al. Alterations of tumor microenvironment by carbon monoxide impedes lung cancer growth. *Oncotarget*. 2016;7(17):23919–23932.
56. Larson SR, et al. Characterization of osteoblastic and osteolytic proteins in prostate cancer bone metastases. *Prostate*. 2013;73(9):932–940.
57. Scherberich JE, Nockher WA. $CD14^{++}$ monocytes, $CD14^+/CD16^+$ subset and soluble CD14 as biological markers of inflammatory systemic diseases and monitoring immunosuppressive therapy. *Clin Chem Lab Med*. 1999;37(3):209–213.
58. Subimerb C, et al. Circulating CD14(+) CD16(+)

monocyte levels predict tissue invasive character of cholangiocarcinoma. *Clin Exp Immunol*. 2010;161(3):471–479.
59. Mukherjee R, Kanti Barman P, Kumar Thatoi P, Tripathy R, Kumar Das B, Ravindran B. Non-classical monocytes display inflammatory features: validation in sepsis and systemic lupus erythematous. *Sci Rep*. 2015;5:13886.
60. Zlotnik A, Yoshie O. The chemokine superfamily revisited. *Immunity*. 2012;36(5):705–716.
61. Liu Q, et al. Interleukin-1β promotes skeletal colonization and progression of metastatic prostate cancer cells with neuroendocrine features. *Cancer Res*. 2013;73(11):3297–3305.
62. Yang YH, et al. Semaphorin 4D promotes skeletal metastasis in breast cancer. *PLoS One*. 2016;11(2):e0150151.
63. Baley PA, Yoshida K, Qian W, Sehgal I, Thompson TC. Progression to androgen insensitivity in a novel in vitro mouse model for prostate cancer. *J Steroid Biochem Mol Biol*. 1995;52(5):403–413.
64. Thompson TC, Southgate J, Kitchener G, Land H. Multistage carcinogenesis induced by ras and myc oncogenes in a reconstituted organ. *Cell*. 1989;56(6):917–930.
65. Smyth GK. Linear models and empirical Bayes methods for assessing differential expression in microarray experiments. *Stat Appl Genet Mol Biol*. 2004;3(1):https://doi.org/10.2202/1544-6115.1027.

HOLOGIC®
The Science of Sure

Powerful images.
Clear answers.

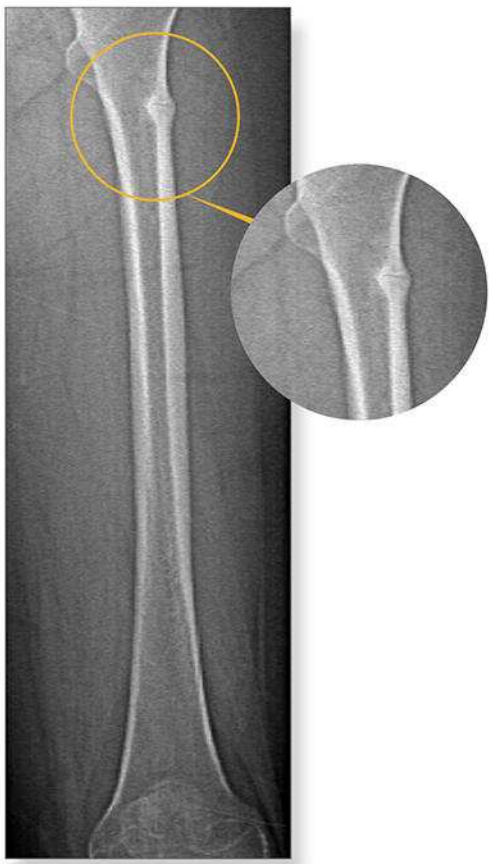

Manage Patient's concerns about Atypical Femur Fracture*

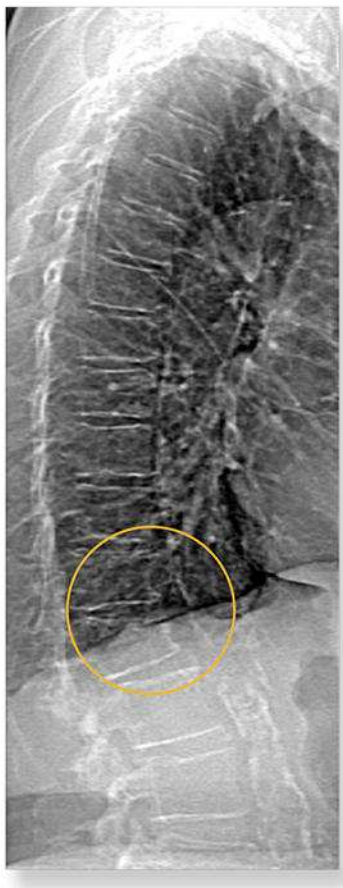

Vertebral Fracture Assessment – a critical part of a complete fracture risk assessment

Advanced Body Composition® Assessment – the power to see what's inside

Contact your Hologic rep today at insidesales@hologic.com

*Incomplete Atypical Femur Fractures imaged with a Hologic densitometer, courtesy of Prof. Cheung, University of Toronto

www.hologic.com | info@hologic.com | 1.781.999.7300

ORIGINAL ARTICLE

JBMR®

Bone Mass Is Compromised by the Chemotherapeutic Trabectedin in Association With Effects on Osteoblasts and Macrophage Efferocytosis

Benjamin P Sinder,[1] Laura Zweifler,[1] Amy J Koh,[1] Megan N Michalski,[1] Lorenz C Hofbauer,[2] Jose Ignacio Aguirre,[3] Hernan Roca,[1] and Laurie K McCauley[1,4]

[1]Department of Periodontics and Oral Medicine, University of Michigan School of Dentistry, Ann Arbor, MI, USA
[2]Center for Healthy Aging, Technische Universität Dresden Technical University Medical Center, Dresden, Germany
[3]Department of Physiological Sciences, College of Veterinary Medicine, University of Florida, FL,, USA
[4]Department of Pathology, University of Michigan, Medical School, Ann Arbor, MI, USA

ABSTRACT

Macrophages have established roles supporting bone formation. Despite their professional phagocytic nature, the role of macrophage phagocytosis in bone homeostasis is not well understood. Interestingly, apoptosis is a pivotal feature of cellular regulation and the primary fate of osteoblasts is apoptosis. Efferocytosis (phagocytosis of apoptotic cells) is a key physiologic process for the homeostasis of many tissues, and is associated with expression of osteoinductive factors. To test effects of macrophage depletion and compromised phagocytosis on bone, 16-week-old male C57BL/6J mice were treated with trabectedin—a chemotherapeutic with established anti-macrophage effects. Trabectedin treatment reduced F4/80+ and CD68+ macrophages in the bone marrow as assessed by flow cytometry, osteal macrophages near the bone surface, and macrophage viability in vitro. Trabectedin treatment significantly reduced marrow gene expression of key phagocytic factors (*Mfge8*, *Mrc1*), and macrophages from treated mice had a reduced ability to phagocytose apoptotic mimicry beads. Macrophages cultured in vitro and treated with trabectedin displayed reduced efferocytosis of apoptotic osteoblasts. Moreover, efferocytosis increased macrophage osteoinductive TGF-β production and this increase was inhibited by trabectedin. Long-term (6-week) treatment of 16-week-old C57BL/6J mice with trabectedin significantly reduced trabecular BV/TV and cortical BMD. Although trabectedin reduced osteoclast numbers in vitro, osteoclast surface in vivo was not altered. Trabectedin treatment reduced serum P1NP as well as MS/BS and BFR/BS, and inhibited mineralization and *Runx2* gene expression of osteoblast cultures. Finally, intermittent PTH 1-34 (iPTH) treatment was administered in combination with trabectedin, and iPTH increased trabecular bone volume fraction (BV/TV) in trabectedin-treated mice. Collectively, the data support a model whereby trabectedin significantly reduces bone mass due to compromised macrophages and efferocytosis, but also due to direct effects on osteoblasts. This data has immediate clinical relevance in light of increasing use of trabectedin in oncology. © 2017 American Society for Bone and Mineral Research.

KEY WORDS: EFFEROCYTOSIS; MACROPHAGES; TRABECTEDIN; PARATHYROID HORMONE; OSTEOIMMUNOLOGY

Introduction

Bone not only provides a rigid structure enabling locomotion, but also houses critical physiologic functions such as hematopoiesis and supports the immune system. The environment of diverse cells in the bone marrow interact with their osteoblast and osteoclast neighbors on the bone surface, regulating bone homeostasis and structure. Myeloid cells are white blood cells that comprise a large portion (15% to 25%) of the marrow, and acquire defined roles regulating the development, homeostasis, and healing of many tissues. Investigating the role of myeloid cells in the bone marrow and specifically osteal macrophages in bone homeostasis was the focus of this study.

Despite the large number of macrophages in bone, their role supporting bone formation has only recently emerged.[1,2] Evidence includes reports of depletion of a broad spectrum of monocyte and macrophage cells under the *csf1r* promoter leading to reduced osteoblast activity in vitro and in vivo, and significantly less bone mass.[3,4] In addition, histologic studies identified a population of osteal macrophages (also known as OsteoMacs) that line a majority of bone formation surfaces in vivo,[3] further linking bone resident macrophages to their support of bone formation. Interestingly, although macrophages ("big-eaters" in Greek) are literally named for their phagocytic ability, the professional phagocytic role of osteal macrophages in bone homeostasis has been largely overlooked.

Received in original form December 10, 2016; revised form June 7, 2017; accepted June 9, 2017. Accepted manuscript online June 10, 2017.
Addresscorrespondence to: Laurie K McCauley, DDS, MS, PhD, University of Michigan School of Dentistry, 1011 N. University Ave., Ann Arbor, MI 48109, USA. E-mail: mccauley@umich.edu
Additional Supporting Information may be found in the online version of this article.
Journal of Bone and Mineral Research, Vol. 32, No. 10, October 2017, pp 2116–2127
DOI: 10.1002/jbmr.3196

Macrophages eat a variety of targets including apoptotic cells. Given that the primary fate of osteoblasts is apoptosis[5,6] and osteal macrophages are found intimately associated with osteoblast-lined bone surfaces,[2,3] macrophages may support bone formation via their clearance of apoptotic bone cells. Yet the consequence of altered macrophage clearance of apoptotic osteoblasts is unclear.

Efferocytosis (phagocytosis of apoptotic cells) is an area of interest that has key physiologic roles in lung homeostasis,[7,8] atherosclerosis,[9,10] disease states such as systemic lupus erythematosus,[11] and cancer.[12] In addition to clearing apoptotic cells and preventing buildup of a toxic microenvironment, efferocytosis also causes macrophage expression of specific chemoattractant and stimulatory cytokines such as TGF-β[13,14] and CCL-2.[15] Recent data strongly suggests a role for efferocytosis in bone homeostasis. For example, although broad depletion of monocytes and macrophages decreased bone mass, an experimental model with increased phagocytic CD68+ cells had increased bone mass.[4] In addition, increases in CD163+ cells and efferocytic gene expression (eg, MFG-E8, MRC1, ARG1) further suggested that changes in macrophage efferocytosis were related to the bone phenotype. However, efferocytosis was not directly assessed in that study. Therefore, the purpose of this study was to examine the role of macrophages and their efferocytic function in bone biology.

Specifically, we determined whether a model with decreased phagocytic CD68+ macrophages and reduced efferocytosis would result in low bone mass. In the present study, macrophages were manipulated via the chemotherapeutic agent trabectedin, which has been shown to selectively inhibit macrophages.[16] There is also strong clinical motivation for this work. Although trabectedin was recently approved by the US Food and Drug Administration (FDA) for use in patients with soft-tissue sarcomas, and is presently in multiple clinical trials for additional forms of cancer,[17] its impact on bone is unknown.

Materials and Methods

Animals

All animal experiments were performed with the approval of the University of Michigan Committee for the Use and Care of Animals. Skeletally mature 16-week-old C57BL/6J male mice (Jackson Laboratory, Bar Harbor, ME, USA) were used unless otherwise noted in long-term and short-term treatment regimens, housed three to five per cage in specific pathogen free (SPF) conditions, fed 5001 chow (Purina), randomized to groups, and given IDs for blinding during subsequent analyses. Trabectedin (Yondelis, PharmaMar, Madrid, Spain) was dissolved in dimethyl sulfoxide (DMSO) at a stock concentration of 1mM, and stored at –20°C until use. A long-term (6-week) treatment regimen was used where animals were administered trabectedin (0.15 mg/kg, i.v. tail vein, biweekly) or vehicle (0.9% saline and DMSO) under isoflurane. Trabectedin treatments were blinded to the injector. Because local tail vein injection site reactions can occur with trabectedin, 14 animals were allocated to the long-term trabectedin group, three of which were euthanized early due to local tail vein injection site reactions resulting in $n = 11$/group. A short-term treatment regimen (1 week) included a single injection of trabectedin (0.15 mg/kg, tail vein) or vehicle given at 16 weeks of age with $n = 8$/group. To assess the effect of anabolic intermittent parathyroid hormone 1-34 (iPTH) on macrophages and osteoblasts in conjunction with trabectedin, mice were treated with iPTH (50 μg/kg body weight, daily) or vehicle (0.9% saline [Veh]) with or without trabectedin (0.15 mg/kg, i.v. tail vein and retro-orbital, biweekly) for 6 weeks with $n = 10$ to 13/group. One Veh/iPTH mouse did not recover after isoflurane and vehicle i.v. injection, leaving Veh/Veh $n = 10$, Veh/iPTH $n = 9$, Trabectedin/Veh $n = 12$, Trabectedin/iPTH $n = 13$. Trabectedin treatment began 3 days prior to iPTH to ensure trabectedin effects at the onset of iPTH. For dynamic histomorphometry analysis, a cohort of animals ($n = 12$/group) were treated with trabectedin or vehicle (0.15 mg/kg), given calcein (30 mg/kg) injections 5 and 2 days before euthanasia, and euthanized 1 week after the single trabectedin injection.

Blood and serum ELISAs

Blood was harvested at euthanasia by intracardiac puncture, allowed to coagulate for several hours at room temperature, serum separated by centrifugation, stored at –80°C, and P1NP and tartrate-resistant acid phosphatase 5b (TRAcP5b) (Immunodiagnostics Systems, The Boldons, UK) were measured using enzyme immunoassays.

Flow cytometry

Marrow was flushed from the femur of mice immediately after euthanasia in FACS buffer (PBS with 2% FBS, 0.5mM EDTA). Each stain included 1×10^6 cells with anti-mouse F4/80 (BioLegend, San Diego, CA, USA, or Abcam, Cambridge, MA, USA; A3-1) or anti-mouse CD68 (BioLegend; FA-11). Isotype controls were used to confirm specificity. Flow cytometry was performed using a FACS AriaIII (BD Biosciences, San Jose, CA, USA).

Micro–computed tomography

Dissected and fixed (10% Neutral Buffered Formalin – NBF, 24hrs) tibiae were scanned by ex-vivo micro–computed tomography (μCT) at a 12-μm voxel size (Scanco μCT-100; Scanco Medical AG, Brüttisellen, Switzerland) and assessed following established guidelines.[18] Trabecular bone parameters were measured over 40 slices (480 μm) immediately distal to the proximal growth plate by manually outlining the endocortical border and thresholding at 180 mg/cm^3. Cortical bone parameters were measured over 30 slices (360 μm) extending distally from a location 3 mm proximal to the tibia-fibula junction. A threshold of 280 mg/cm^3 was used for cortical bone.

Histomorphometry and dynamic histomorphometry

Tibias were fixed in 10% neutral buffered formalin (NBF), stored in 70% ETOH, decalcified in 14% ethylenediaminetetraacetic acid (EDTA), embedded in paraffin, and sectioned at 5 μm. A central slice of the proximal tibia was stained by H&E and bone morphometry was analyzed using OsteoMeasure software (OsteoMetrics, Decatur, GA, USA) and an Olympus (Tokyo, Japan) microscope for bone area/tissue area (BA/TA), Tb.Th, and Tb.N.[19,20] The ROI began ~200 μm distal to the proximal growth plate, extended 1215 μm distally, and was 1150 μm wide (or 50 μm from endocortical surface). An adjacent section was stained for tartrate resistant acid phosphatase (TRAP; Sigma, St. Louis, MO, USA; 387A) and hematoxylin. Using the ROI described above, osteoclast surface (Oc.S), bone surface (BS), and number of osteoclasts were quantified.[19] Similarly, osteal macrophages were quantified by immunostaining of adjacent paraffin sections for F4/80 (Abcam; ab6640; Anti-Rat HRP-DAB

Kit; R&D Systems, Minneapolis, MN, USA) and identified by their proximity of within three cell diameters of the bone surface.[21] Osteal macrophage number normalized to tissue area and bone surface were quantified. Dynamic histomorphometry was performed in 16-week-old C57BL/6J male mice treated with vehicle or trabectedin (0.15 mg/kg i.v., $n = 12$/group) and given calcein injections 5 days and 2 days before euthanasia at 17 weeks of age. In brief, tibias were cut cross-sectionally, placed in 10% phosphate-buffered formalin for 48 hours, dehydrated in ethanol, and embedded undecalcified in methyl methacrylate. The proximal tibias were sectioned longitudinally at 8 μm thicknesses with a Leica/Jung 2065 microtome and used to measure fluorochrome-based indices of bone formation. The ROI began 0.4 mm distal to the growth plate and excluded the primary spongiosa and cancellous bone within 0.1 mm of the endocortical surfaces, including a 1.2 mm (width) by 3.6 mm (length) area. Mineral apposition rate (MAR), SL (Single Label), DL (Double Label), mineralizing surface (MS/BS), and bone formation rate per unit of bone surface (BFR/BS) were enumerated or calculated following recommendations of the Histomorphometry Nomenclature Committee of the American Society of Bone and Mineral Research.[20]

RT-PCR

Bone marrow was flushed with TRIzol from the femur of mice treated with trabectedin or vehicle for 1 week, and RNA was isolated. For cell culture experiments, RNA was isolated with the RNeasy system (Qiagen, Valencia, CA, USA). In each case, RNA was quantified (Nanodrop, Thermo Fisher Scientific, Waltham,

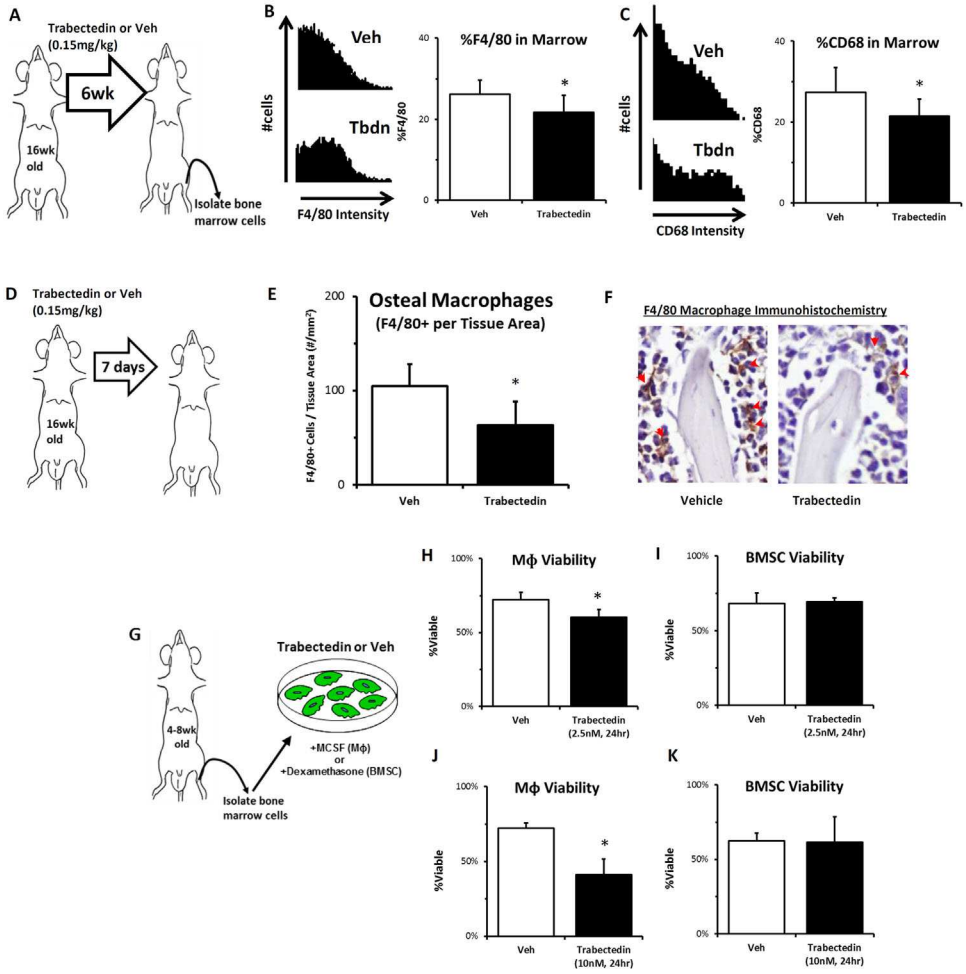

Fig. 1. Trabectedin treatment inhibits macrophages. (*A*) Male 16-week-old C57BL/6J mice treated with trabectedin (Tbdn) or vehicle (Veh) for 6 weeks (0.15 mg/kg, three biweekly injections, $n = 9$ to 13/group). After marrow extraction, cells were stained for F4/80 (*B*) and phagocytic marker CD68 (*C*), and analyzed by flow cytometry, with representative images shown. (*D–F*) In animals treated for 1 week with trabectedin, tibial paraffin sections of metaphyseal trabecular bone and stained for F4/80 by immunohistochemistry. Osteal macrophages per tissue area were quantified (*E*) and representative images are shown (*F*) with red arrows denoting examples of osteal macrophages (F4/80+ and within 3 cell diameters of bone surface). (*G*, *H*, *J*) To confirm a direct effect of trabectedin on macrophages, macrophages (Mϕ) were expanded from the bone marrow from 4-week-old to 8-week-old C57BL/6J mice with M-CSF, and viability assessed by trypan blue exclusion after trabectedin treatment. (*G*, *I*, *K*) Similarly, BMSCs from 4-week-old to 8-week-old C57BL/6J mice were expanded with dexamethasone, viability assessed after trabectedin treatment. Data are mean ± SD. $^{*}p < 0.05$ versus Veh. Mϕ = macrophages; Tbdn = trabectedin; Veh = vehicle.

MA, USA) and cDNA generated via reverse transcriptase reactions. cDNA products were amplified and detected with TaqMan Gene Expression PCR master mix (Applied Biosystems, Foster City, CA, USA) and TaqMan probes included *Mfge8* (Mm00500549_m1), *Mrc1* (Mm01329362_m1), Mertk (Mm00434920_m1), and *Runx2* (Mm00501584_m1). *Gapdh* (*Mm99999915_g1*) was used as the reference for bone marrow, and Actb (Mm02619580_g1) was used for as a reference for in vitro experiments. Real-time PCR was analyzed on a ViiA7 (Applied Biosystems, Foster City, CA, USA) and quantified via the comparative threshold cycle (ΔΔCt) method.[22]

Ex vivo phagocytosis assay

Bone marrow was flushed from the femur of mice 1 week after a single dose of trabectedin or vehicle and immediately co-cultured with FITC+ 5-μm-diameter apoptotic-mimicry beads (Bangs Laboratories, Fishers, IN, USA) with a 1.1 ratio of cells: beads at 37 °C (4 °C was used as a control) in a flow cytometry tube. After 5 hours, cells were fixed with 1% formalin on ice for 1 hour, stained for F4/80 (APC), and analyzed by flow cytometry to assess phagocytosis. To visualize bead internalization and attachment to macrophages, samples were further analyzed using ImageStream (EMD Millipore, Billerica, MA, USA).

Efferocytosis of apoptotic osteoblasts in vitro

Primary macrophages were cultured by flushing bone marrow from the hindlimbs of 4-week-old to 8-week-old C57BL/6J with macrophage colony stimulating factor (M-CSF, 30 ng/mL; PeproTech, Rocky Hill, NJ, USA) for 1 week, and 750,000 cells were split into each well of a six-well plate as described.[15] Macrophages attached overnight in α-MEM media with 5% FBS and 15 ng/mL M-CSF, and subsequently treated with 2.5nM trabectedin in DMSO or vehicle (DMSO) for 12 hours in low serum media (0.25% FBS). Prior to co-culture, osteoblastic MC4 (MC3T3-E1 subclone4)[23] cells were expanded, stained (DeepRed CellTracker; Thermo Fisher Scientific, Rockford, IL, USA), induced to apoptosis by 30 min of exposure to a UV light source (>90% Trypan Blue+), allowed to recover for 2 hours at 37°C, and added in equal number (1:1) to trabectedin-treated and vehicle-treated macrophages as described.[15] After 1 hour, the efferocytic co-culture was stopped by fixation with 1% formalin, cells were harvested, and macrophages were stained green (FITC, F4/80). Efferocytosis was assessed as the percentage of double positive FITC macrophages and Deep Red–stained apoptotic MC4 cells by flow cytometry.

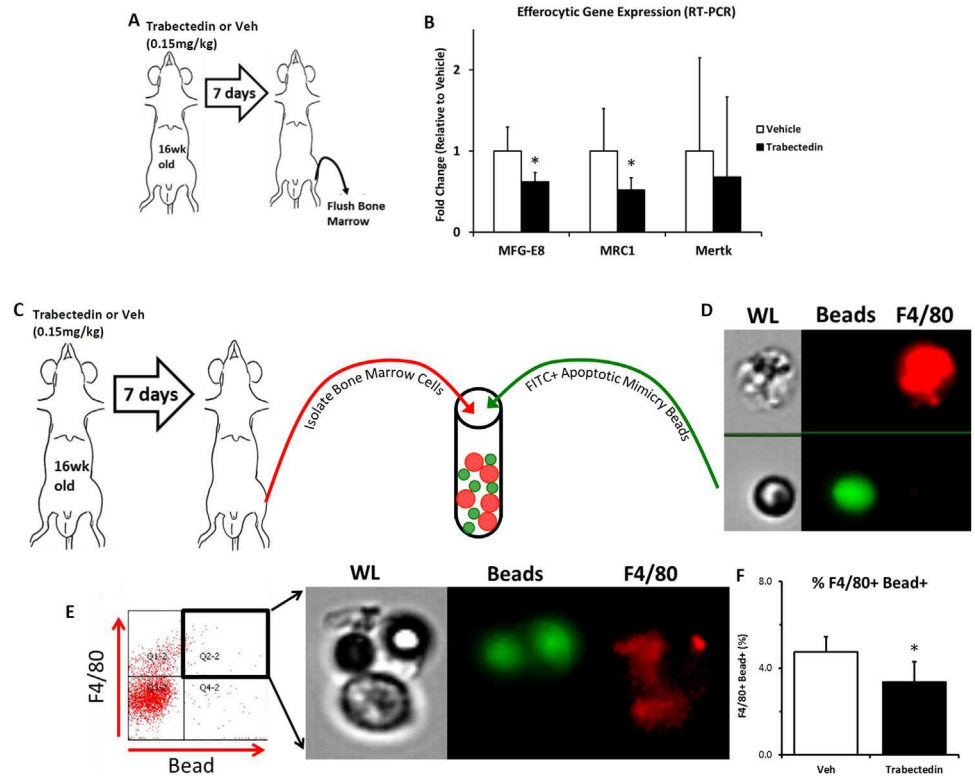

Fig. 2. In vivo trabectedin treatment reduces phagocytic ability of macrophages. (*A*) Sixteen-week-old male C57BL/6J mice were treated for 1 week with trabectedin (0.15 mg/kg) or vehicle (Veh). Marrow was extracted and mRNA isolated to assess gene expression. (*B*) Significantly decreased expression of *Mfge8* (linker protein that facilitates efferocytosis) and *Mrc1* (marker of alternatively activated efferocytic macrophages), and unaltered levels of Mertk (protein that facilitates efferocytosis). (*C*) Fresh bone marrow cells were isolated from 16-week-old male C57BL/6J mice treated for 1 week with trabectedin (0.15 mg/kg) or Veh, and immediately co-cultured with FITC+ apoptotic mimicry beads. After 5 hours of phagocytosis, co-cultures were fixed, macrophages were stained for F4/80 (*D*), and the percent of F4/80+ macrophages that ingested or were attached to a FITC+ bead was assessed via flow cytometry (*E*). Trabectedin significantly reduced phagocytosis within the F4/80 macrophage population (*F*). $n = 8$/group. Data are mean ± SD. $^*p < 0.05$ versus Veh. Veh = vehicle; WL = White Light.

TGF-β secretion by efferocytic macrophages

Macrophages treated with vehicle or trabectedin were co-cultured with apoptotic MC4 cells as described in previous methods section. After 18 hours of co-culture, supernatants were harvested to assess secreted TGF-β by macrophages in response to efferocytosis. Supernatants were exposed to acid to convert to active TGF-β, and then active TGF-β was assessed with a commercially available ELISA (R&D Systems). The α-MEM media supplemented with 0.25% FBS contained undetectable levels of TGF-β (data not shown).

Viability of macrophages, MC4 cells, calvarial osteoblasts, and bone marrow stromal cells

Macrophages from 4-week-old to 8-week-old C57BL/6J mice were expanded with M-CSF and plated at 750,000 per well in six-well tissue culture plates as described in previous "Efferocytosis of apoptotic osteoblasts in vitro" methods section. MC4 cells, and bone marrow stromal cells (BMSCs) isolated from 4-week-old to 8-week-old C57BL/6J mice and expanded with 10nM dexamethasone, were cultured as described. Primary calvarial osteoblasts were isolated from 4-day-old to 10-day-old C57BL/6J mice per published protocols.[24] BMSCs, MC4 cells, and macrophages were treated with vehicle (DMSO) or trabectedin. Cells were removed from the plate with 0.25% trypsin immediately after treatment, or after being returned to normal α-MEM with 10% FBS for 4 days, and viability and cell number were assessed by trypan blue staining with a hemocytometer.

Osteoclast formation and resorption assays

Marrow was flushed from the long bones of 4-week-old to 8-week-old C57BL/6J mice into a 100-mm dish in α-MEM with 10% FBS and 1% penicillin-streptomycin-glutamine (PSG) overnight. The next day, suspension cells were re-plated in new 100-mm Petri culture plastic dishes with 30 ng/mL of M-CSF, and expanded for 4 to 5 days until confluent. Cells were then split with ice-cold PBS containing 1 μM EDTA and re-plated at 60,000/cm^2 in 48-well or 96-well plates with 30 ng/mL of M-CSF and 50 ng/mL of murine RANKL (PeproTech, Rocky Hill,

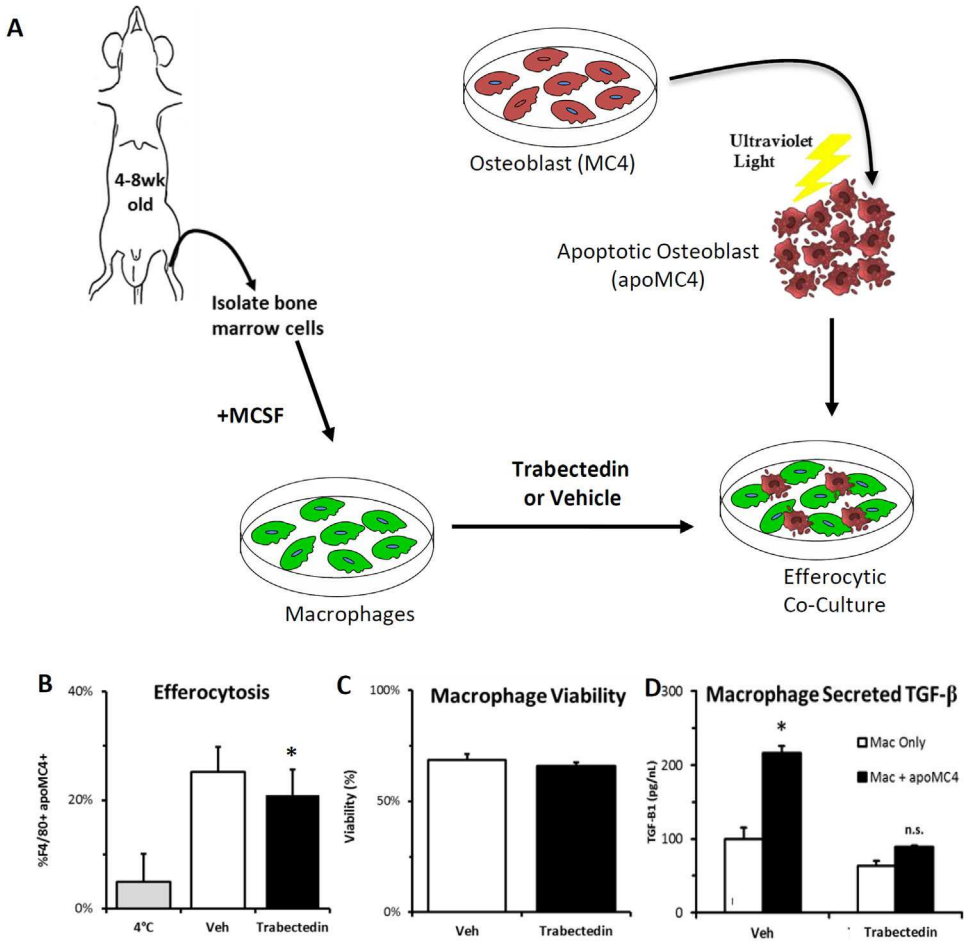

Fig. 3. Reduced macrophage efferocytosis with trabectedin in vitro. (*A*) Marrow was extracted from 4-week-old to 8-week-old C57BL/6J mice, and macrophages expanded with M-CSF for 1 week. MC4 cells were stained red via DeepRedCell tracker dye, induced to apoptosis by UV light, and subsequently added to macrophages that were treated with trabectedin or vehicle. Macrophages were subsequently stained for F4/80 with an FITC fluorophore. (*B*) Efferocytosis was assessed by double-positive F4/80 and apoptotic MC4 cells, and efferocytosis was reduced by trabectedin pretreatment at a dose (2.5nM, 12 hours) that did not affect (*C*) macrophage viability ($n = 6$ to 9/group). (*D*) Macrophages secreted significantly more osteoinductive TGF-β with efferocytosis, and this increase was inhibited by trabectedin (10nM, 24 hours) in vitro as assessed by ELISA ($n = 3$/group). Data are mean ± SD. $^*p < 0.05$ versus Veh. Veh = vehicle.

NJ, USA). Once multinucleated osteoclasts began forming (4 to 5 days), wells were treated with trabectedin or vehicle. Cells were subsequently fixed with 10% formalin, stained for TRAP (Sigma, St. Louis, MO, USA; 387A), and enumerated. To assess effects of trabectedin on resorption, similar experiments were carried out on 96-well Corning Osteo Assay plates (Sigma, St. Louis, MO, USA) coated with hydroxyapatite, and hydroxyapatite dissolution was assessed. Macrophages were first grown as described above in separate plates with M-CSF and then similarly split in equal number into wells of Corning Osteo Assay plates and RANKL added. After osteoclastogenesis on D3-D4 in the Corning Osteo Assay plate, cells were treated with trabectedin at specified doses, replaced with normal osteoclast media for an additional 24 hours after treatment, and resorption area was quantified as the percent of white area.

Osteoblast mineralization and gene expression

Primary calvarial osteoblasts were isolated from 4-day-old to 10-day-old C57BL/6J mice per published protocols,[24] and cultured in α-MEM with 10% FBS and 1% PSG. Once cells reached confluence (day 0), media was supplemented with 50μM ascorbic acid for gene expression or 50 μM ascorbic acid plus 10mM β-glycerol phosphate for mineralization assays with every media change. MC4 cells were grown under identical conditions. Osteoblasts used for gene expression were treated from day 4 to day 5 with varying doses of trabectedin and RNA was collected on day 5. Osteoblasts assayed for mineralization were similarly treated from day 4 to day 5, subsequently replaced with media supplanted with 50μM ascorbic acid plus 10mM β-glycerol phosphate and allowed to mineralize to day 14 (MC4) or day 21 (calvarial osteoblasts). Von Kossa staining was performed as described.[25]

Statistical analysis

Student's *t* test, or paired *t* test, was used where appropriate and after normality was assessed. The trabectedin and iPTH in vivo data with 2×2 experimental design was analyzed by two-way ANOVA, and least significant difference (LSD) post hoc test. Power analysis calculations assuming 5% type I error indicated that $n = 8$/group had a 85% chance to detect a difference between means based on 1.5 standard deviations between groups—assumptions based on historical data. Values of $p < 0.05$ were considered significant, and data are shown as mean ± SD.

Results

Trabectedin inhibits macrophages and phagocytic cells in vivo and in vitro

Trabectedin treatment in vivo reduced F4/80+ macrophages in the bone marrow by 16% compared to vehicle when assessed after 6 weeks of treatment (Fig. 1*A*, *B*). In addition,

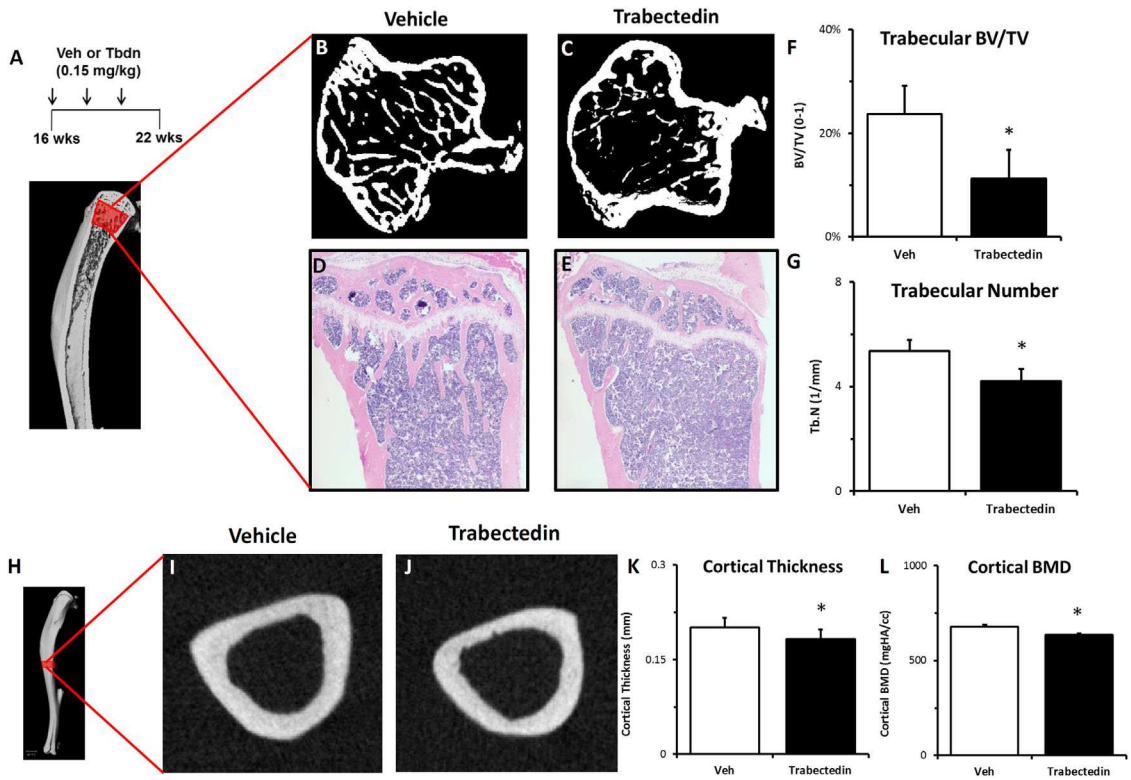

Fig. 4. Trabectedin reduces trabecular and cortical bone properties. (*A*) Long-term treatment regimen (6 weeks, 0.15 mg/kg, 3×) with trabectedin (Tbdn) or vehicle (Veh) was used to assess whole-bone changes the proximal tibia of 16-week-old male C57BL/6J mice. (*B–E*) Representative μCT and H&E images show reduced trabecular bone mass with treatment. (*F*, *G*) Quantification of μCT revealed a decrease in trabecular BV/TV due to significantly reduced trabecular number. (*H*) Trabectedin effects were also assessed in cortical bone of the diaphyseal tibia. (*I*, *J*) Representative μCT images show decreased cortical bone, including reduced cortical thickness (*K*) and BMD (*L*). $n = 11$/group. Data are mean ± SD. $^{*}p < 0.05$ versus Veh. Tbdn = trabectedin; Veh = vehicle.

phagocytic CD68+ cells in the bone marrow were reduced by 23% with trabectedin treatment (Fig. 1*C*). Osteal macrophages, identified as F4/80+ cells near the bone surface, were significantly reduced (–39%) per tissue area (Fig. 1*D–F*) as well as per bone surface (data not shown). In vitro experiments confirmed trabectedin directly inhibits macrophages. Primary murine macrophages grown with M-CSF for 1 week were treated with trabectedin and viability assessed by trypan blue exclusion. Treatment for 24 hours with 10nM trabectedin significantly decreased macrophage viability by 43%, and 24 hours with 2.5nM trabectedin decreased macrophage viability by 17% (Fig. 1*G*, *H*, *J*). BMSCs expanded from marrow with dexamethasone were treated with identical doses of trabectedin and no significant difference in viability was observed (Fig. 1*I*, *K*), indicating relative specificity to the myeloid lineage.

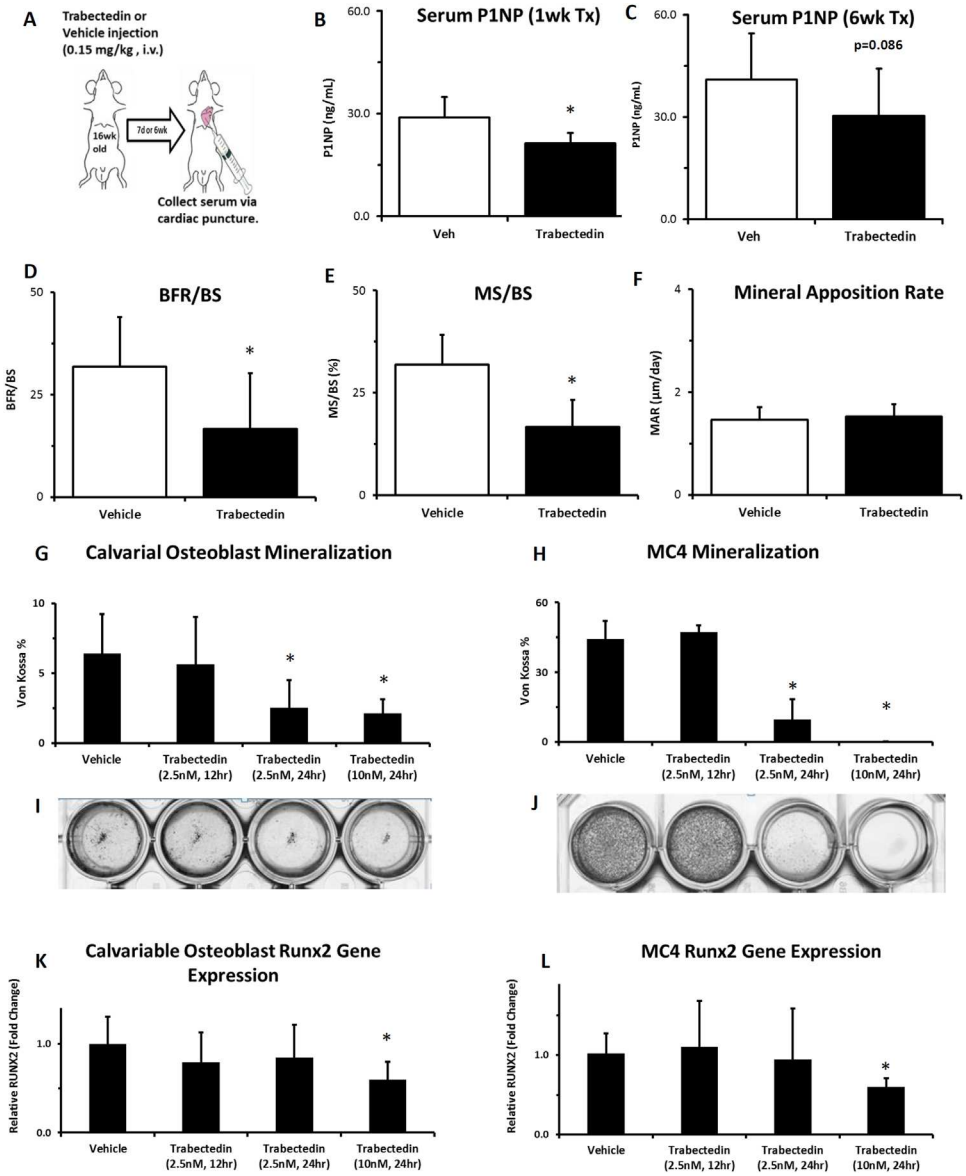

Fig. 5. Trabectedin reduces markers for bone formation and mineralization. (*A*) Short-term (1 week, single injection 0.15 mg/kg, $n = 8$/group) or long-term (6 weeks, 3 biweekly injections, 0.15 mg/kg, $n = 11$/group) with trabectedin or vehicle (Veh) reduced serum P1NP, a marker of bone formation. (*D–F*) A cohort ($n = 12$/group) of mice were treated with trabectedin or vehicle for 1 week as shown in *A* and given calcein injections 5 or 2 days prior to euthanasia to facilitate dynamic histomorphometric analysis of tibial trabecular bone. Trabectedin treatment significantly reduced BFR/BS and MS/BS, but not MAR. (*G*, *I*) To assess direct effects of trabectedin on osteoblasts, calvarial osteoblasts were isolated from 4-day-old to 10-day-old C57BL/6J mice and treated with trabectedin from days 4 to 5, replaced with normal mineralization media with ascorbic acid and beta-glycerophosphate until day 21, and stained for Von Kossa ($n = 6$/group). Representative images are shown. (*H*, *J*) The same treatment strategy as in *G*, *I* was used in the MC4 cell line, and stained via Von Kossa at day 14 ($n = 6$/group). (*K*, *L*) To assess effects of trabectedin on osteoblast gene expression, both calvarial osteoblasts and MC4 cells were treated with trabectedin from days 4 to 5 and assessed by RT-PCR for relative *Runx2* expression ($n = 6$/group). $^{*}p < 0.05$ relative to Veh. Data are mean ± SD. Tx = treatment; Veh = vehicle.

Trabectedin leads to reduced efferocytic gene expression and reduced macrophage efferocytosis

One week after a single injection of trabectedin, total gene expression in the marrow showed reduced levels of key macrophage efferocytosis mediators *Mfge8* (–48%) and *Mrc1* (–38%) (Fig. 2*A*, *B*). To assess functional changes in phagocytosis, marrows harvested from mice 1 week after a single injection of trabectedin were immediately co-cultured with FITC+ apoptotic mimicry beads. The co-culture was stained for F4/80 and flow cytometry analysis revealed a significant decrease (–28%) in phagocytosis as indicated by the %F4/80+Bead+ cells (Fig. 2*C*–*F*). In vitro experiments extended this finding using apoptotic osteoblasts as the prey. Apoptotic osteoblastic MC4 cells were added in co-culture to primary macrophages that were treated with trabectedin. Trabectedin treatment of macrophages reduced their efferocytosis of apoptotic MC4 osteoblasts as indicated by significantly reduced double-positive (%F4/80+ apMC4+) cells without significant compromise in viability (Fig. 3*A*–*C*). Macrophage efferocytosis significantly increased secretion of osteoinductive TGF-β, and this increase was inhibited by trabectedin in vitro (Fig. 3*D*).

Trabectedin significantly reduces trabecular and cortical bone mass

The bone phenotype was evaluated in mice treated with trabectedin for 6 weeks (three biweekly administrations). In the proximal tibia, BV/TV was significantly reduced (–52%) compared to vehicle controls as measured by μCT (Fig. 4*A*–*F*). Reductions in BV/TV were the result of large decreases in Tb.N (–21%) (Fig. 4*G*) and increases in Tb.Sp but no significant change in Tb.Th (data not shown). Histologic evaluation of the proximal tibia on H&E-stained sections (Fig. 4*D*, *E*) confirmed the μCT data, and showed an 84% reduction in BA/TA (data not shown). In cortical bone of the diaphyseal tibia, similar findings of decreased bone mass were observed, evidenced by reduced cortical thickness (–9%) and cortical BMD (–6%) (Fig. 4*H*–*L*). Ct.Ar/Tt.Ar was significantly reduced (–7%), Ct.Ar trended less (–9%, $p = 0.06$), and Tt.Ar was unchanged ($p = 0.72$) (data not shown).

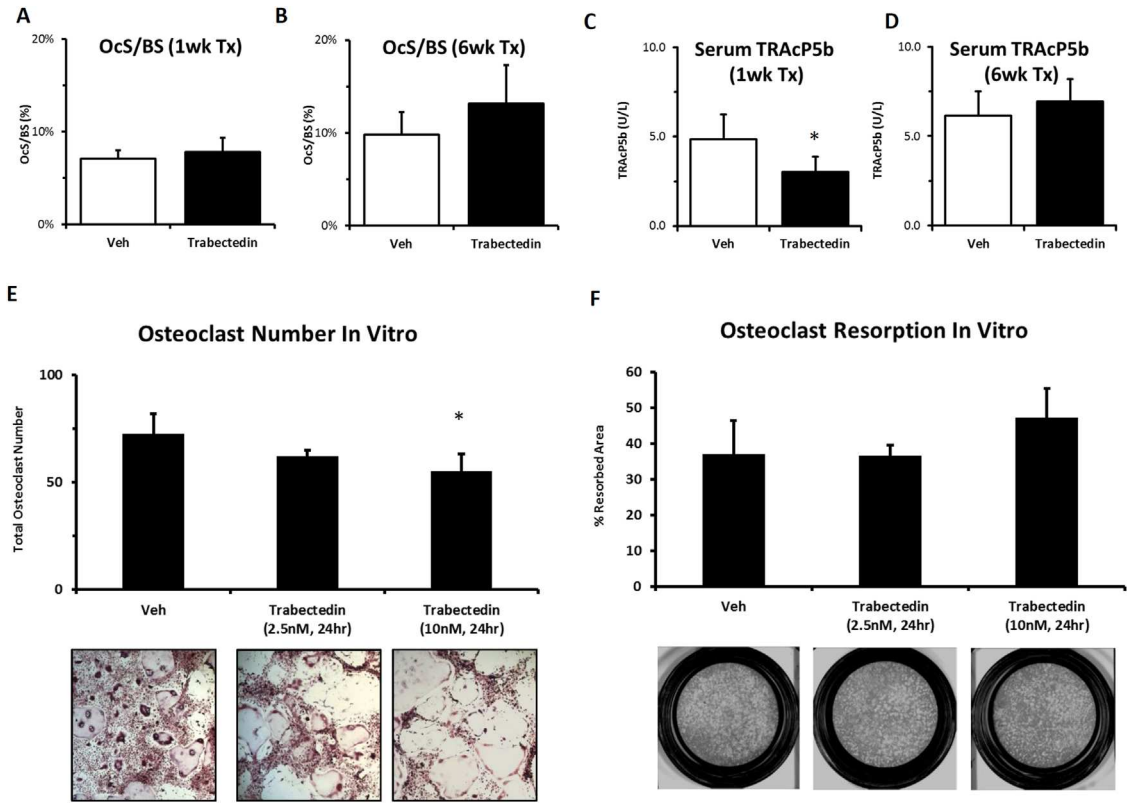

Fig. 6. Analysis of trabectedin effects on osteoclasts. (*A*,*B*) Both short-term (1 week, single injection 0.15 mg/kg, $n = 8$/group) or long-term (6 weeks, 3 biweekly injections 0.15mg/kg, $n = 11$/group) trabectedin treatment regimens were performed and OcS/BS was assessed by TRAP staining of a central slice of the proximal tibia. (*C*, *D*) In these same mice, serum TRAcP5b was quantified. (*E*) To assess direct effects of trabectedin on osteoclast number in vitro, osteoclasts were cultured from the marrow of 4-week-old to 8-week-old C57BL/6J mice with M-CSF and RANKL. After osteoclastogenesis on days 4 to 5, cells were treated with trabectedin at specified doses, stained for TRAP, and enumerated ($n = 6$/group). Representative images are shown beneath. (*F*) To assess functional changes in resorption with trabectedin, osteoclasts were grown on Corning Osteo Assay plates under identical conditions, treated with trabectedin on days 4 to 5, replaced with normal osteoclast media for an additional 24 hours after treatment, and resorption area was quantified as the percent of white area. Representative images are shown. $^{*}p < 0.05$ relative to Veh. Data are mean ± SD. Veh = vehicle; OcS/BS = osteoclast surface per bone surface.

Trabectedin reduces bone formation, and directly inhibits osteoblast gene expression and mineralization in vitro

Serum P1NP, a marker of bone formation, was significantly decreased (–27%) 1 week after a single trabectedin injection, and trended toward a decrease (–26%, $p = 0.086$) after 6 weeks of trabectedin treatment (Fig. 5*A*–*C*). Dynamic histomorphometry of tibial trabecular bone 1 week after a single of injection of trabectedin showed significantly reduced MS/BS (–42%) and BFR/BS (–48%) (Fig. 5*D*, *E*). The remaining areas of dual label after trabectedin treatment showed no significant change in MAR relative to vehicle (Fig. 5*D*–*F*). To determine if reductions in bone formation were related to direct effects of trabectedin on osteoblastic cells, osteoblast in vitro assays were performed. Primary calvarial osteoblasts were cultured in mineralization media, and treated with trabectedin from day 4 to day 5, and subsequently allowed to mineralize in trabectedin-free mineralization media to day 21. At day 21, Von Kossa staining revealed significantly less mineralization in calvarial osteoblasts treated with trabectedin (Fig. 5*G*, *I*). *Runx2* gene expression was also reduced in primary calvarial osteoblast cells using the same treatment strategy and assessing acute gene expression on day 5 in the highest trabectedin dose (Fig. 5*K*). Both of these findings in primary calvarial osteoblasts were corroborated by parallel experiments performed in the MC4 cell line (Fig. 5*H*, *J*, *L*). In MC4 cells, *Runx2* gene expression was significantly reduced at day 5 (Fig. 5*I*), and mineralization was significantly lower at day 14 with trabectedin treatment (Fig. 5*E*, *G*). Using an identical treatment protocol in both calvarial and MC4 osteoblasts, but assessing cell viability, it was found that after 24 hours treatment did not significantly impact osteoblast viability (Supporting Fig. 1A). However, treatment for 24 hours, and then replacement with normal media for 4 additional days led to significantly compromised osteoblast cell number by day 5 (Supporting Fig. 1B).

Trabectedin effects on osteoclasts

Histologic osteoclast analysis by TRAP staining in sections of the proximal tibia revealed no change in Oc.S/BS 1week after a single injection of trabectedin, or after 6 weeks of biweekly treatment (Fig. 6*A*, *B*). Similar histologic TRAP staining data was observed for N.Oc/BS (data not shown). Serum analysis of TRAcP5b showed no change after 6 weeks of treatment, but did show a significant decrease 1 week after a single injection (–38%) (Fig. 6*C*, *D*). To assess direct effects of trabectedin on osteoclasts, primary murine osteoclasts were differentiated with RANKL and treated with trabectedin. After cells differentiated into osteoclasts on approximately day 4 of culture, trabectedin treatment decreased the total number of multinucleated TRAP+ cells by 24% (Fig. 6*E*). Detailed analysis revealed that while trabectedin decreased the number of smaller osteoclasts with dense cytoplasm, large osteoclasts were similar in number with treatment but appeared to have less dense cytoplasm with trabectedin treatment. To assess functional effects of trabectedin on bone resorption in vitro, osteoclasts were cultured on hydroxyapatite coated plates. After osteoclasts began to form on approximately day 4 of culture, wells were treated with trabectedin for 24 hours, subsequently replaced with normal osteoclast media for 24 additional hours, and assessed for resorption pits. No significant change in resorption pit area was detected with trabectedin treatment (Fig. 6*F*).

Anabolic PTH treatment in combination with trabectedin

Anabolic treatment with intermittent PTH 1-34 (iPTH) significantly increased tibial trabecular BV/TV due to increases in Tb.N in non–trabectedin-treated mice (Fig. 7*A*–*C*). Similar to Fig. 4, 6 weeks of trabectedin treatment reduced trabecular BV/TV due to a reduction in Tb.N. iPTH treatment significantly increased BV/TV in trabectedin-treated mice due to significant changes in Tb.N. However, Tb.N in mice treated with both iPTH and trabectedin was significantly less than untreated Veh/Veh controls (Fig. 7*C*). BV/TV in mice receiving both trabectedin and iPTH was not significantly different than untreated control mice.

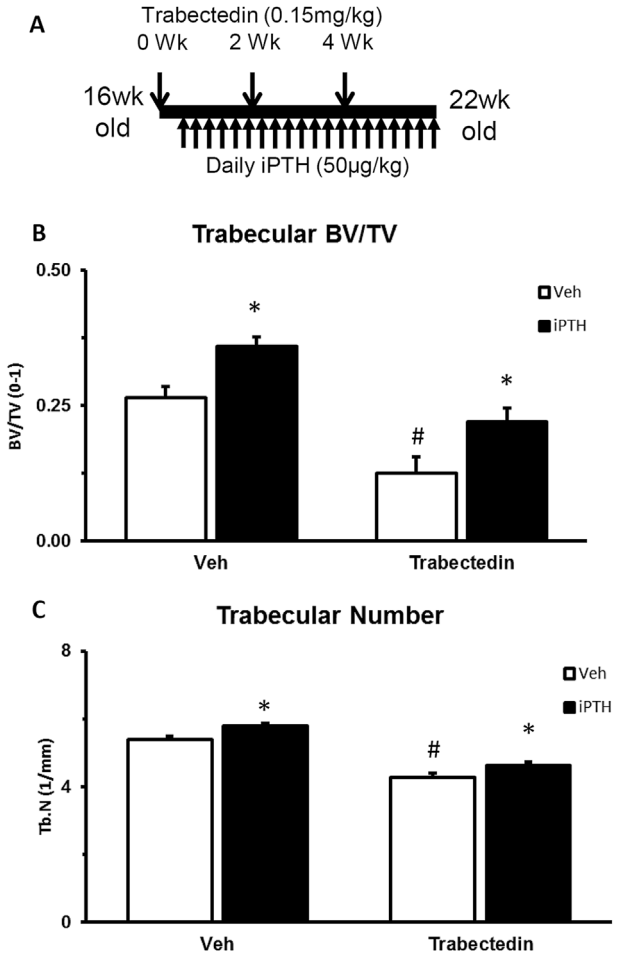

Fig. 7. Anabolic PTH partially rescues trabectedin treatment effects. (*A*) Male 16-week-old C57BL/6J mice were treated in a 2 × 2 study design for 6 weeks with either trabectedin or its vehicle control, and/or intermittent PTH 1-34 (iPTH) or its vehicle control ($n = 9$ to 13/group). To ensure trabectedin was having biologic activity at the commencement of anabolic therapy, iPTH was started 3 days after the first trabectedin injection. (*B*) Trabectedin significantly reduced trabecular tibial BV/TV, iPTH increased BV/TV, and iPTH was able to increase BV/TV in trabectedin treated mice. (*C*) Changes in BV/TV were largely due to changes in Tb.N. On an absolute level, untreated vehicle control mice had a greater Tb.N than mice treated with both trabectedin and iPTH, suggesting iPTH did not completely rescue the trabectedin phenotype. $^{*}p < 0.05$ versus respective vehicle. $\#p < 0.05$ versus vehicle/vehicle. Data are mean ± SD. Veh = vehicle.

Discussion

This study focused on macrophage contributions to skeletal homeostasis and adds new data to the field of osteoimmunology. Although significant contributions have been made that show the effect of macrophage number on bone, data in this study extends the field by examining functional changes in macrophage efferocytosis, thereby highlighting a new mechanism by which macrophages impact bone mass. The results also have immediate clinical relevance as trabectedin is currently administered to patients for the treatment of cancer,[17] with no information about the impact on the skeleton. Thus, the data presented in this study has immediate implications for patients receiving trabectedin treatment.

The results of this study add to a growing body of literature highlighting the impact of osteal macrophages on bone formation and bone mass. Previously, data found an association between elevated phagocytic CD68+ cells, increased levels of efferocytic genes, and increased bone mass.[4] Because efferocytosis was not directly assessed, a central purpose of the present study was to determine whether a model with reduced CD68+ cells and efferocytosis would have an associated decrease in bone mass. Indeed, trabectedin treatment in mice reduced phagocytic CD68+ macrophages and decreased bone mass. Importantly, we extended the investigation of decreased efferocytic gene expression and directly assayed changes in phagocytosis and efferocytosis with trabectedin. Data show that F4/80+cells were less able to phagocytose apoptotic mimicry beads, suggesting that the macrophages were not only fewer in number but also less functional. This data was corroborated by in vitro studies showing that trabectedin-treated macrophages were less able to phagocytose apoptotic osteoblasts. Of note, macrophages efferocytosing apoptotic osteoblasts secreted significantly more TGF-β, a well-characterized osteoinductive factor, suggesting a functional consequence of efferocytosis. This increase was inhibited by macrophage pretreatment with trabectedin. We note that our data do not prove that efferocytosis and macrophage-derived TGF-β are responsible for bone forming effects, and it may be that apoptotic cell clearance itself is responsible for a positive impact of macrophage efferocytosis on bone. Collectively, these data supports a model whereby macrophages promote bone homeostasis in part by their efferocytic function.

In addition to effects on macrophages, we also observed effects of trabectedin on bone formation in vivo as well as direct effects on osteoblasts in vitro. The in vivo serum marker of bone formation, P1NP, showed reduced levels with trabectedin treatment. Similarly, dynamic histomorphometry of metaphyseal tibial trabecular bone also showed reduced bone formation as evidenced by significantly lower MS/BS and BFR/BS with trabectedin treatment. One possibility to explain reduced serum P1NP and bone formation in vivo is that it is an indirect effect of inhibiting macrophages[4,26] and compromising efferocytosis. However, to determine if trabectedin may also have a direct effect on osteoblasts, we treated primary calvarial, and MC4 osteoblasts in vitro with trabectedin. Our data showed that trabectedin inhibited mineralization of both calvarial osteoblasts, and MC3T3 (subclone 4) cells in vitro. Moreover, this inhibition of mineralization was corroborated by reduced *Runx2* gene expression in both osteoblast cell types. Although this data demonstrates a direct effect of trabectedin on osteoblasts, the mechanism underlying the data is unclear. We note that mineralization effects on trabectedin are greater in magnitude than effects on *Runx2*, suggesting that mineralization effects may also be due to general toxicity to osteoblasts (Supporting Fig. 1). Trabectedin interacts with TNF-related apoptosis-inducing ligand (TRAIL), which mediates its monocytic cell inhibition. TRAIL receptors are present on osteoblasts, and may regulate cell death under certain conditions.[27–29] Other possibilities include that trabectedin can bind to the DNA minor groove and inhibit FUS/CHOP (Fused in Sarcoma/C/EBP homologous protein) fusion proteins that support osteoblasts,[30,31] and cells deficient in homologous recombination are particularly sensitive to trabectedin effects. Regardless of the mechanism, trabectedin did appear to directly influence osteoblasts, even though its effect on cell viability was greater in macrophages than BSMCs.

Trabectedin effects on osteoclasts were more varied. Trabectedin treatment of osteoclasts in vitro showed decreased osteoclast number after a short-term treatment period. Although serum TRAcP5b was reduced in vivo 1 week after a single injection of trabectedin, it was not significantly altered after 6 weeks of trabectedin treatment. Most importantly, histologic analysis of osteoclasts on the trabecular bone surface revealed no significant difference or trend after 1 week or 6 weeks of trabectedin treatment. That trabectedin is capable of directly effecting osteoclasts is not surprising given its already established impact on macrophages. Indeed, osteoclasts are susceptible to TRAIL-mediated apoptosis.[32,33] However, the in vivo analyses of osteoclasts on the bone surface showed no significant change. It may be that that analysis of osteoclast surface at time points closer to the injection of trabectedin (<1 week) would show a difference and align with observed in vitro effects. We note that previous analysis of osteoclast on the bone surface in models of macrophage depletion such as the MAFIA (Macrophage Fas-Induced apoptosis) and clodronate models similarly did not show a significant difference.[4] This may collectively suggest that osteoclasts are a prioritized and conserved differentiation pathway of the myeloid lineage, or have the ability to quickly reconstitute.

The results of this work have immediate clinical relevance to patients currently receiving trabectedin for a variety of sarcomas. In particular, these patients may be at increased risk of fracture on account of reduced bone mass. Moreover, trabectedin is currently being explored for the treatment of breast and prostate cancer,[17] which preferentially metastasize to the skeleton. Given that bone cells have been shown to play a role regulating skeletal metastasis,[34] and that trabectedin modulates bone cells and the bone microenvironment, it will be important to consider if potential trabectedin effects on metastasis are due to altering bone cells in addition to directly inhibiting tumor cells.

In this study, we observed that iPTH was effective at increasing trabecular bone mass in trabectedin-treated mice. This data has several implications. First, it may generally suggest that an anabolic strategy may be an effective therapeutic option to increase bone mass in patients receiving trabectedin. Although iPTH is not available for use in cancer patients, other anabolic bone treatments are in clinical trials.[35] Prior data suggest that iPTH anabolism may be regulated by macrophages and efferocytosis[4,36]; however, the data presented here suggest that partially inhibiting macrophages and efferocytosis with trabectedin does not inhibit the anabolic actions of PTH. It is possible that inhibiting macrophages and efferocytosis by a greater magnitude may further compromise PTH anabolic effects.

Finally, there are several limitations to this study. First, all experiments were carried out in noncancerous models to assess the effect of macrophages and efferocytosis on bone during normal homeostasis. Thus, the results of this study may not directly model a cancer patient receiving trabectedin. An additional limitation is that experiments in this study were performed in male mice, and therefore results may differ in females. Finally, results focused on the appendicular skeleton, and trabectedin effects may differ in axial skeletal sites.

In summary, this study adds new data regarding the role of macrophages and efferocytosis within the bone microenvironment. Importantly, it suggests that in addition to macrophage number, the efferocytic function of macrophages in the bone microenvironment may also regulate bone homeostasis. In addition, because patients are currently receiving trabectedin but the bone phenotype of trabectedin has not been previously described, the data in this study has immediate clinical relevance.

Disclosures

LCH: Consultancy for Alexion, Amgen, Shire, Lilly, Radius, and UCB to institution and personally; payment for development of educational presentations for Alexion, Amgen, and UCB to institution and personally. All other authors (BPS, LZ, AJK, MNM, JIA, HR, LKM) have no disclosures.

Acknowledgments

This study was supported by the National Institutes of Health DK053904 (LKM) and CA093900 (LKM) and P30AR069620 (Univ. Michigan), DOD W81XWH-14-1-0408 (BPS), NIH F30DE025154 (MNM), and Deutsche Forschungsgemeinschaft Forschergruppe-1586 SKELMET (LCH). We acknowledge Michelle Lynch and Justin Do for μCT assistance, and Chris Strayhorn for histology sectioning.

Authors' roles: Study design: BPS and LKM. Study conduct: BPS, LZ, MNM, and AJK. Data collection: BPS, LZ, AJK, MN, and JIA. Data analysis: BPS, LZ, and JIA. Data interpretation: All authors. Drafting manuscript: BPS and LKM. Revising and approving manuscript: All authors. BPS and LKM take responsibility for the integrity of the data analysis.

References

1. Horwood NJ. Macrophage polarization and bone formation: a review. Clin Rev Allergy Immunol. 2016;51(1):79–86.
2. Sinder BP, Pettit AR, McCauley LK. Macrophages: their emerging roles in bone. J Bone Miner Res. 2015;30(12):2140–9.
3. Chang MK, Raggatt L-J., Alexander KA, et al. Osteal tissue macrophages are intercalated throughout human and mouse bone lining tissues and regulate osteoblast function in vitro and in vivo. J Immunol. 2008;181(2):1232–44.
4. Cho SW, Soki FN, Koh AJ, et al. Osteal macrophages support physiologic skeletal remodeling and anabolic actions of parathyroid hormone in bone. Proc Natl Acad Sci U S.A. 2014;111(4): 1545–50.
5. Parfitt AM. Bone-forming cells in clinical conditions. In: Hall B, editor. Bone. Vol 1 Osteoblast Osteocyte. Boca Raton, FL: CRC Press; 1990. p. 351–429.
6. Jilka RL, Weinstein RS, Bellido T, Parfitt AM, Manolagas SC. Osteoblast programmed cell death (apoptosis): modulation by growth factors and cytokines. J Bone Miner Res. 1998;13(5):793–802.
7. Medeiros AI, Serezani CH, Lee SP, Peters-Golden M. Efferocytosis impairs pulmonary macrophage and lung antibacterial function via PGE2/EP2 signaling. J Exp Med. 2009;206(1):61–8.
8. Vandivier RW, Henson PM, Douglas IS. Burying the dead: the impact of failed apoptotic cell removal (efferocytosis) on chronic inflammatory lung disease. Chest. 2006;129(6):1673–82.
9. Thorp E, Cui D, Schrijvers DM, Kuriakose G, Tabas I. Mertk receptor mutation reduces efferocytosis efficiency and promotes apoptotic cell accumulation and plaque necrosis in atherosclerotic lesions of apoe$^{-/-}$ mice. Arterioscler Thromb Vasc Biol. 2008; 28(8):1421–8.
10. Thorp E, Tabas I. Mechanisms and consequences of efferocytosis in advanced atherosclerosis. J Leukoc Biol. 2009;86(5):1089–95.
11. Shao W-., Cohen PL. Disturbances of apoptotic cell clearance in systemic lupus erythematosus. Arthritis Res Ther. 2011; 13(1):202.
12. Soki FN, Koh AJ, Jones JD, et al. Polarization of prostate cancer-associated macrophages is induced by milk fat globule-EGF factor 8 (MFG-E8)-mediated efferocytosis. J Biol Chem. 2014;289(35): 24560–72.
13. Huynh M-LN, Fadok VA, Henson PM. Phosphatidylserine-dependent ingestion of apoptotic cells promotes TGF-beta1 secretion and the resolution of inflammation. J Clin Invest. 2002;109(1): 41–50.
14. Xiao YQ, Freire-de-Lima CG, Schiemann WP, Bratton DL, Vandivier RW, Henson PM. Transcriptional and translational regulation of TGF-β production in response to apoptotic cells. J Immunol. 2008;181(5):3575–85.
15. Michalski MN, Koh AJ, Weidner S, Roca H, McCauley LK. Modulation of osteoblastic cell efferocytosis by bone marrow macrophages. J Cell Biochem. 2016 Dec;117(12): 2697–706.
16. Germano G, Frapolli R, Belgiovine C, et al. Role of macrophage targeting in the antitumor activity of trabectedin. Cancer Cell. 2013;23(2):249–62.
17. ClinicalTrials.gov. Trabectedin studies. Available from: https://clinicaltrials.gov/ct2/results?term=trabectedin.
18. Bouxsein ML, Boyd SK, Christiansen BA, Guldberg RE, Jepsen KJ, Müller R. Guidelines for assessment of bone microstructure in rodents using micro-computed tomography. J Bone Miner Res. 2010;25(7):1468–86.
19. Parfitt AM, Drezner MK, Glorieux FH, et al. Bone histomorphometry: standardization of nomenclature, symbols, and units. Report of the ASBMR Histomorphometry Nomenclature Committee. J Bone Miner Res. 1987;2(6):595–610.
20. Dempster DW, Compston JE, Drezner MK, et al. Standardized nomenclature, symbols, and units for bone histomorphometry: a 2012 update of the report of the ASBMR Histomorphometry Nomenclature Committee. J Bone Miner Res. 2013;28(1):2–17.
21. Alexander KA, Raggatt L-J., Millard S, et al. Resting and injury-induced inflamed periosteum contain multiple macrophage subsets that are located at sites of bone growth and regeneration. Immunol Cell Biol. 2017;95(1):7–16.
22. Livak KJ, Schmittgen TD. Analysis of relative gene expression data using real-time quantitative PCR and the $2^{-\Delta\Delta C}_{T}$ method. Methods. 2001;25(4):402–8.
23. Wang D, Christensen K, Chawla K, Xiao G, Krebsbach PH, Franceschi RT. Isolation and characterization of MC3T3-E1 preosteoblast subclones with distinct in vitro and in vivo differentiation/mineralization potential. J Bone Miner Res. 1999; 14(6):893–903.
24. Datta NS, Chen C, Berry JE, McCauley LK. PTHrP signaling targets Cyclin D1 and induces osteoblastic cell growth arrest. J Bone Miner Res. 2005;20(6):1051–64.
25. Koh AJ, Beecher CA, Rosol TJ, McCauley LK. 3′,5′-Cyclic adenosine monophosphate activation in osteoblastic cells: effects on parathyroid hormone-1 receptors and osteoblastic differentiation in vitro. Endocrinology. 1999;140(7):3154–62.
26. Pettit AR, Chang MK, Hume DA, Raggatt L-J. Osteal macrophages: a new twist on coupling during bone dynamics. Bone. 2008;43(6): 976–82.

27. Mori G, Brunetti G, Colucci S, et al. Alteration of activity and survival of osteoblasts obtained from human periodontitis patients: role of TRAIL. J Biol Regul Homeost Agents. 2007; 21(3–4): 105–14.
28. Tinhofer I, Biedermann R, Krismer M, Crazzolara R, Greil R. A role of TRAIL in killing osteoblasts by myeloma cells. FASEB J. 2006;20(6):759–61.
29. Atkins GJ, Bouralexis S, Evdokiou A, et al. Human osteoblasts are resistant to Apo2L/TRAIL-mediated apoptosis. Bone. 2002;31(4):448–56.
30. Pereira RC, Delany AM, Canalis E. CCAAT/enhancer binding protein homologous protein (DDIT3) induces osteoblastic cell differentiation. Endocrinology. 2004;145(4):1952–60.
31. Shirakawa K, Maeda S, Gotoh T, et al. CCAAT/enhancer-binding protein homologous protein (CHOP) regulates osteoblast differentiation. Mol Cell Biol. 2006;26(16):6105–16.
32. Zauli G, Rimondi E, Nicolin V, Melloni E, Celeghini C, Secchiero P. TNF-related apoptosis-inducing ligand (TRAIL) blocks osteoclastic differentiation induced by RANKL plus M-CSF. Blood. 2004;104(7): 2044–50.
33. Roux S, Lambert-Comeau P, Saint-Pierre C, Lépine M, Sawan B, Parent J-L. Death receptors, Fas and TRAIL receptors, are involved in human osteoclast apoptosis. Biochem Biophys Res Commun. 2005;333(1):42–50.
34. Logothetis CJ, Lin S-H. Osteoblasts in prostate cancer metastasis to bone. Nat Rev Cancer. 2005;5(1):21–8.
35. McClung MR, Grauer A, Boonen S, et al. Romosozumab in postmenopausal women with low bone mineral density. N Engl J Med. 2014;370(5):412–20.
36. McCauley LK, Dalli J, Koh AJ, Chiang N, Serhan CN. Cutting edge: parathyroid hormone facilitates macrophage efferocytosis in bone marrow via proresolving mediators resolvin D1 and resolvin D2. J Immunol. 2014;193(1):26–9.